PFC/RR-81-1 DOE/ET/51013-3
UC 20

HIGH FREQUENCY GYROTRONS AND THEIR APPLICATION TO TOKAMAK PLASMA HEATING

K. E. Kreischer

January 1981

M.I.T.
Plasma Fusion Center
Cambridge, MA 02139

HIGH FREQUENCY GYROTRONS AND THEIR APPLICATION TO TOKAMAK PLASMA HEATING*

K. E. Kreischer

Plasma Fusion Center +
Massachusetts Institute of Technology
Cambridge, Massachusetts 02139

* Work supported by U.S.D.O.E. contract DE-AC-02-78ET-51013

+ Supported by U.S. Department of Energy

ABSTRACT

A comprehensive analysis of high frequency (100-200 GHz) and high power (> 100 kW) gyrotrons has been conducted. It is shown that high frequencies will be required in order for electron cyclotron radiation to propagate to the center of a compact tokamak power reactor. High power levels will be needed in order to ignite the plasma with a reasonable number of gyrotron units.

In the first part of this research, a set of analytic expressions, valid for all TE cavity modes and all harmonics, is derived for the starting current and frequency detuning using the Vlasov-Maxwell equations in the weakly relativistic limit. These results are applicable for any longitudinal distrubution of the RF field. It is shown that the starting current can be expressed in a simple form which contains the Fourier transform of this distribution. This formalism is used to investigate the effect of RF field profiling, and it is found that a weak RF field at the input end of the cavity prebunches the electrons and reduces the starting current. This theory is also used to study mode competition and starting characteristics in the high frequency regime.

In the second part of this report the use of an optical cavity is investigated. It is found that such a resonator has good mode selectivity characteristics, and may be capable of supporting much higher power levels than a closed cavity. A general linear theory is derived that includes both the electric and magnetic interaction mechanisms that is valid for any angle between the wave vector $\bar{k}$ and the beam direction. Two configurations are studied in detail: $\bar{k}$ perpendicular to and parallel to the beam. The former case is of interest only when $\bar{E}$

is perpendicular to the beam, and gives a pure ECM interaction with no magnetic contribution analogous to the mechanism analyzed in the first part of this report. In the latter case, both electric and magnetic terms are present but tend to offset one another yielding rather high, but feasible, starting currents. A 140 GHz gyrotron operating in the TEM_{00-18} mode is designed which exhibits good mode separation properties but requires a perpendicular velocity dispersion of less than 1%.

This report concludes with the design of an ECR heating system for a commercial fusion reactor. This consists of a parametric analysis of a 100 kW, 200 GHz gyrotron and the design of a microwave transmission and port system based on a reasonable extrapolation of presently available technology. In the parametric analysis, a procedure is outlined for selecting a design point that conforms to the technical and physical limitations, including cavity cooling requirements and constraints on the maximum beam current. A transmission system utilizing the TE_{01} mode in an oversized waveguide is described with a total power loss of 20%. At present, the primary unknowns of this system include the deleterious effect of spurious modes as well as the lack of high power, high frequency components.

Submitted by Kenneth E. Kreischer to the M.I.T. Department of Nuclear Engineering on January 28, 1981 in partial fulfillment of the requirements for the degree of Doctor of Philosophy.

Table of Contents

LIST OF FIGURES AND TABLES

Acknowledgements

Credit is due to many people for their assistance during the course of this work. I am particularly indebted to Dr. Richard J. Temkin for the guidance and support he provided during this research. His advice provided much needed direction and stimulus for this work. I also wish to express my gratitude to my reader, Professor Lawrence Lidsky, for his help in defining the overall goals of this work, and for pointing out areas where future study could be done. I am also grateful for the support Dr. Daniel R. Cohn has provided both during my undergraduate and my graduate studies.

A number of associates provided useful input at various stages of this research. Many thanks to Drs. R. C. Davidson and H. S. Uhm for discussions about the properties of relativistic beams, and to Dr. S. Wolfe for his assistance in defining ECRH constraints on fusion reactors. I am also grateful to Joel Schultz and Dr. Leslie Bromberg for their help concerning the material of Chapter 5. I also thank those people involved in the production of this report, including typists Diane Carcia and Regina Montane.

Finally, I must thank my family and friends for their support and encouragement during my graduate studies, and especially my wife, Debbie, for her enduring patience and for the sacrifices she has made on my behalf.

Chapter 1

Introduction

Over the past decade electron cyclotron resonance heating (ECRH) has become a viable method of heating a tokamak plasma. The reason for this is twofold. First, recent experiments [1,2] have shown that electron cyclotron radiation can be coupled effectively to the plasma, producing a localized and controlled deposition of energy. Secondly, electron cyclotron masers (ECM), and in particular the gyrotron, have been produced that can provide high powers in the millimeter and submillimeter regime.

In most present reactor designs, plasma heating is accomplished with neutral beam injection. However, it may be difficult to achieve high efficiency and obtain good plasma penetration when heating power-producing tokamaks with neutral beams. RF or microwave power has been suggested as an alternative. Major RF heating experiments have been carried out on tokamak plasmas primarily at one of the following frequencies: ion cyclotron (ICRH) in the 30-200 MHz range, lower hybrid (LHH) at 1 - 5 GHz, and ECRH at 30 - 85 GHz. Although the technology of RF heating at lower frequencies (ICRH and LHH) is decidedly simpler, and efficient, high power sources and auxiliary components are available, the problem of coupling RF power to the bulk of the plasma tends to become most difficult at these low frequencies. The two primary reasons for this are the plasma opacity, which causes the wave energy to be deposited near the plasma surface unless special precautions are taken, and the need for special antenna structures because the radiation wavelength is comparable to or

larger than the plasma dimensions. On the other hand, electron cyclotron radiation should have little difficulty reaching the plasma center if certain accessibility criteria are met. In addition, the propagation and absorption processes relevant to the use of ECRH in power reactors appear to be linear phenomena, and as a result theoretical understanding of the coupling process is greatly simplified. Linear theory predicts that ECRH absorption, which is already effective in today's experiments, will increase as the electron temperature, machine size, and magnetic field strength increase. Since the region where this energy is deposited is narrow can be controlled by adjusting the wave frequency, ECRH has possible benefits beyond simple bulk heating. It may also be used to modify the pressure profile in tokamaks in such a way as to stabilize MHD disruptions [3]. It has also found uses in other devices, including mirrors [4] and the bumpy torus [2]. The use of ECRH is limited only by the lack of high power sources.

Gyrotrons and related devices presently appear to be the best candidates to fill this gap. The term gyrotron was invented by A. V. Gaponov in 1965 for a special type of ECM characterized by a cavity near cutoff and utilizing a magnetron injection gun to produce the electron beam. Coherent radiation is emitted at approximately the Doppler-shifted frequency $\omega = n\omega_c + k_{||} u$, where ω_c is the cyclotron frequency, n is the harmonic number, $k_{||}$ is the wavenumber parallel to the cavity axis, and u is the parallel electron velocity. The cutoff condition implies that $k_{||} u << n\omega_c$, and as a result the emitted frequency $\omega \simeq n\omega_c$ and the above resonance condition is insensitive to any inherent spread of u.

The emission mechanism of the gyrotron results from the relativistic

dependence of the electron mass, and consequently ω_c , on the energy of the electron. As the beam interacts with the RF field, some of the electrons lose energy while others gain, and as a result a bunching in phase space occurs. By properly selecting the phase of these bunched electrons with respect to the RF field, net emission is possible. This unique mechanism allows the gyrotron not to be hampered by problems facing both microwave and optical devices as they are extrapolated to the millimeter regime. Unlike microwave sources, the gyrotron does not rely on small-scale structure on the order of a wavelength in size that might be susceptible to overheating. In addition, and in contrast to a laser, the electrons are able to give up many energy quanta to the electromagnetic wave, and as a result efficient operation is possible.

The major components of the gyrotron are illustrated in Fig. 1.1, which is a schematic of the λ = 8.9 mm device used by Kisel' et. al. [5]. The system consists of three major parts: a magnetron injection gun that creates the electron beam to the left, the resonant cavity in the center, and the collector to the right. The gyrotron is symmetric about the z axis. The solenoids produce a magnetic field that points in the z direction and has a profile shown in the graph. As a result of the symmetry, the cathode with its emitter strip is able to produce an intense flow of electrons with rather small velocity dispersion. The electrons, guided by the magnetic field and accelerated by the electrostatic field produced by the anodes, enter a region of magnetic compression. Here, the transverse energy of the electrons increases according to the adiabatic invariant w^2/B_o = constant, where w is the electron perpendicular velocity and B_o is the axial magnetic field.

Fig. 1.1 **8.9 MM GYROTRON**

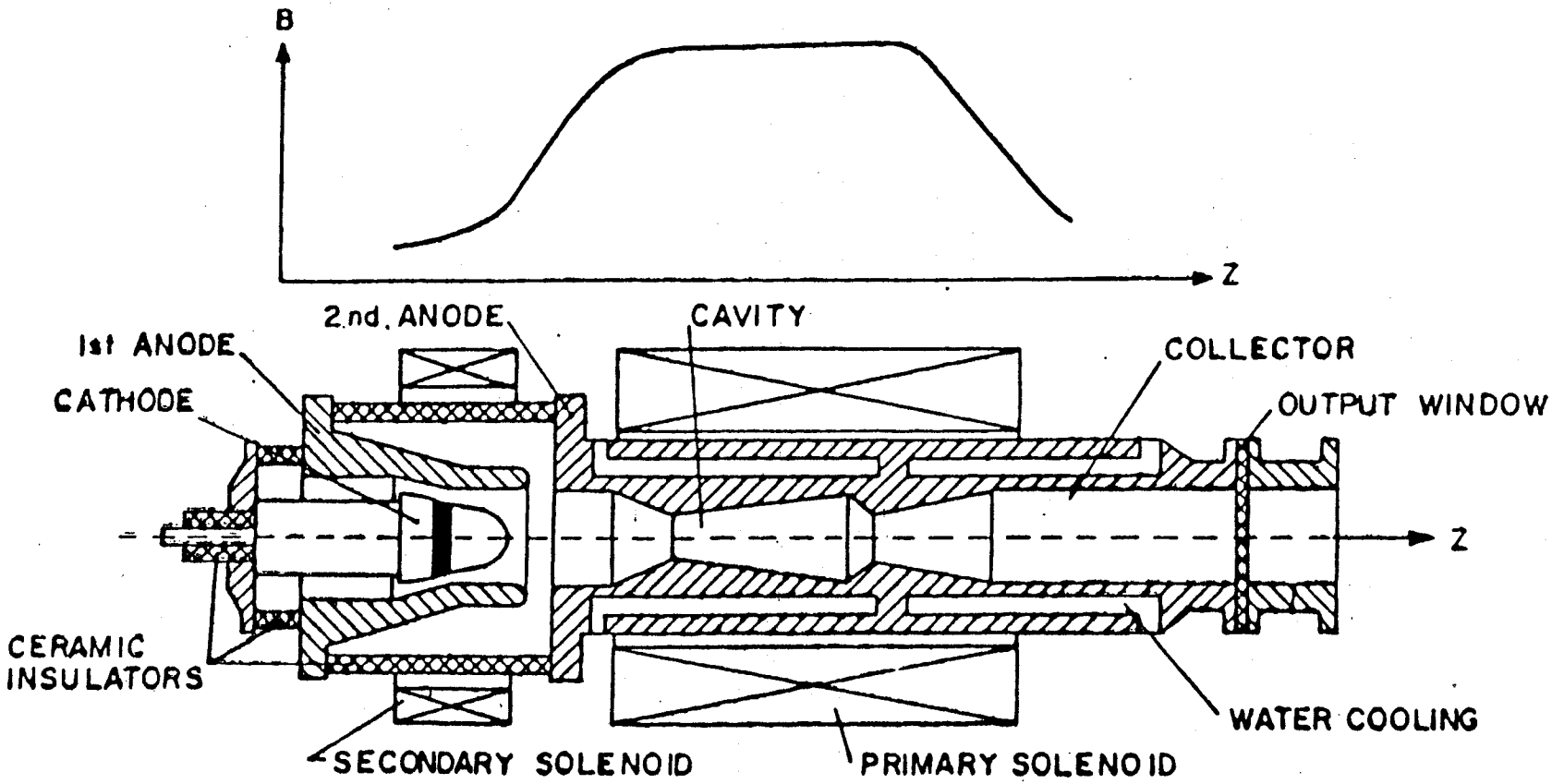

Ref: Kisel' et. al., Radio Eng. Electron. Phys., 19, No.4, 95 (1974)

Once within the cavity, the electrons interact with the resonant RF field, and an energy transfer from the electrons to the field occurs. After leaving the cavity, the electrons enter a region of decreasing field (decompression section) and are deposited on a large surface collector. The RF field is transmitted through the output window and down the transmission line to the plasma.

Early ECR heating experiments were carried out at low density and low initial electron temperature, resulting in heating of the electron tail distribution to high energies [6 , 7]. In 1972, the first successful ECR heating experiments were reported in two separate tokamak experiments in the Soviet Union. At the Kurchatov Institute in Moscow, V. V. Alikaev et al. reported heating results [8] on the TM-3 tokamak. A gyrotron with a wavelength of about 1 cm, a power of about 40 kW and a pulse length of about 0.5 msec was used. The electron temperature rise was 200 - 400 ev, with an initial temperature of about 250 ev. The heating efficiency was 20 - 30%. On the Tuman-2 tokamak at the Ioffe Institute in Leningrad, ECR heating experiments were reported by Golant et al. [9]. The microwave power at 34 GHz was up to 40 kW for 100 μsec. A heating efficiency of several tens of percent was obtained.

More recent experiments have been carried out at both Institutes with higher power levels, longer pulse lengths, larger tokamaks and, at Kurchatov, higher frequencies. In the time period from 1971 - 1976, experiments were performed at wavelengths of 10 and 5 mm on the TM-3 tokamak. Heating was carried out at magnetic fields of up to 2.5 T and plasma density of up to 1×10^{13} cm^{-3}. The experiments at $\lambda \sim 5$ mm had a power of about 60 kW and those at 10 mm had a power of about

100 kW, for a pulse duration of 1 ms. [10,11,12]. At present, experiments are being carried out on the T-10 tokamak at Kurchatov Inst. with two, 200 kW gyrotrons of 3.5 mm wavelength and 20 - 100 msec pulse duration, and initial results indicate successful heating.

A major commitment has been made to ECR heating for the T-15 tokamak which will be built at the Kurchatov Institute. Ordinary wave heating will be carried out at a field of 3.5 T and density of up to 7×10^{13} cm^{-3} using 5 MW of gyrotron power. The gyrotron system will consist of 24 units, each emitting 200 kW for a pulse length of 1.5 sec. The experiment should commence in 1983 - 1984. This ECR heating experiment should certainly be viewed as a major test of both ECR heating theory and gyrotron technology.

In the U.S., the major recent applications of ECR heating of plasmas have been to the EBT and ISX-B experiments at ORNL. The EBT experiment is performed in a CW mode, unlike the pulsed mode of tokamaks. Consequently, gyrotrons developed for this experiment will have to fulfill the more difficult specifications of CW operation. A 28 GHz, 200 kW gyrotron has been developed at Varian Co. for use on the EBT experiment [13]. For the EBT-II experiment, a 2 MW system of ten, 200 kW, CW gyrotrons will be needed. Very recently a pulsed gyrotron developed at the Naval Research Laboratory that could produce 100 kW at 35 GHz for a 10 msec pulse was used successfully to heat ISX-B [44]. The power was injected from the inside of the torus so that both the ordinary and extraordinary modes could propagate to the plasma center. An absorption efficiency of about 60% was obtained with good bulk electron temperature heating. This gyrotron is presently being used on the Versator tokamak at MIT [14]. Fig. 1.2 illustrates the present

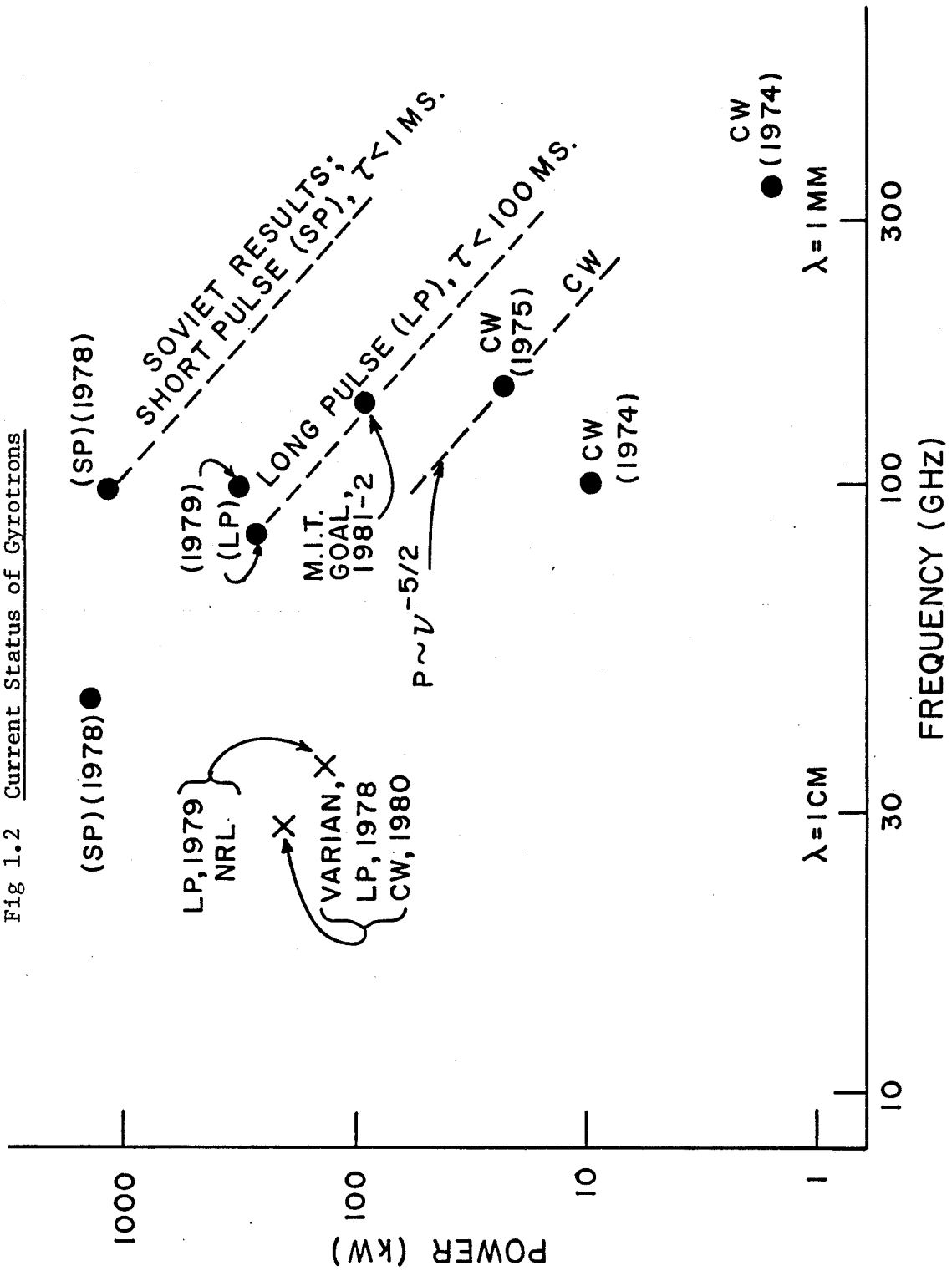

Fig 1.2 Current Status of Gyrotrons

status of gyrotron research. Both the past results achieved by the Soviet Union and the U.S., as well as future goals, are shown. In addition, lines are drawn illustrating the $\nu^{-5/2}$ power law (ν = frequency) for extrapolating power versus frequency. Numerous other gyrotron experiments are presently being planned. The level of effort represented by these experiments adds greatly to the credibility of ECR heating as an eventual option.

The primary goals of this report are twofold. First, an extensive analysis of the linear theory of the gyromonotron and the optical gyrotron has been conducted in order to obtain a basic understanding of the physical processes involved in the electron beam-RF field interaction. This has involved the identification of all electric and magnetic field mechanisms, and the determination of when these mechanisms dominate. Such an understanding of the basic processes is crucial before the problems associated with high frequency operation can be solved. The linear, rather than the nonlinear, theory has been developed for several reasons. The linear theory can be solved analytically, and as a result the physical processes involved are more evident. The nonlinear behavior can only be obtained numerically, and is therefore difficult to interpret. Also, most linear analyses have been restricted to specific device configurations, and are therefore not applicable to many gyrotrons being investigated at the present time. The need for a general theory is thus evident. Finally, the linear theory gives good insight into problems that will become severe as ν increases. Mode competition in particular falls into this category.

The second major goal of this research is to extrapolate present knowledge about gyrotrons to the high power, high frequency regime required for ECR heating of fusion power reactors. In this manner the major constraints can be identified. Such an analysis is helpful in the identification of areas where future research is necessary.

This report is presented in the following manner. In Chapter 2, the constraints imposed on the gyrotron frequency by the propagation of ECR radiation to the plasma center is discussed. It is shown that compact reactors will require frequencies greater than 100 GHz. In Chapter 3 the general theory of the gyromonotron is developed that gives the starting current and frequency detuning of this device. This theory is then applied to a number of topics that are relevant to present gyrotron research. In Chapter 4 the theory of a gyrotron with an optical resonator is presented. In this case both magnetic and electric field mechanisms are present, their relative strengths depending upon the orientation of the wave vector $\bar{k}$ with respect to the beam. Chapter 5 deals with the extrapolation of the gyrotron to a power reactor environment, and identifies its basic features and constraints. Conclusions are presented in Chapter 6.

Chapter 2

Physics Contraints of an ECR Heated Reactor

The design of an ECR heated tokamak reactor must take into account the conditions for the absorption of RF radiation in the plasma. These conditions impose additional contraints on the reactor design, constraints which ultimately place a lower limit on the toroidal magnetic field. This in turn determines the minimum frequency at which the gyrotrons must operate. The analysis outlined in this chapter is kept general so that the conclusions reached are not specifically tied to any single reactor design. It begins with a discussion of the characteristics of electromagnetic wave propagation and absorption in a toroidal plasma at the fundamental and second harmonic frequencies. Conditions resulting from the need to avoid cutoff are then combined with equations giving the plasma density and temperature required for stable, ignited operation to obtain the reactor's regime of operation. How these restrictions affect the choice of gyrotron frequency will then be discussed.

In this chapter four possible heating modes are considered: ordinary (O) wave heating at $\omega = \omega_c \equiv eB_o/\gamma m_e c$, where the wave is launched from outside the torus (low field region); extraordinary (X) wave heating at $\omega = \omega_c$, where the wave is launched from the inside the torus (high field region); extraordinary wave at $\omega = 2\omega_c$ with the wave launched from the outside; and ordinary wave at $\omega = 2\omega_c$. In order to determine the conditions under which these waves can propagate to the plasma center, one must examine the Appleton-Hartree dispersion relation [15], which can be derived from the linearized cold electron fluid

equations. Specializing to the case of an ordinary wave in a cold plasma, this relation can be written as

$$k_\perp^2 c^2 = \omega^2 - \omega_p^2 \tag{2.1}$$

where $\omega_p = (ne^2/\varepsilon_o m)^{1/2}$ is the plasma frequency. Propagation is possible ($k_\perp^2 > 0$) provided $\omega^2 > \omega_p^2$. This inequality can be rewritten in terms of the dimensionless parameter $\alpha \equiv \omega_p^2/\omega_c^2 = m_e n_o/\varepsilon_o B_o^2$, where n_o is the plasma density and it is understood that all parameters are to be evaluated on the plasma axis. The accessibility conditions for the ordinary wave at the first two harmonics can be expressed as

$$\begin{aligned} \omega_c \text{ wave:} \quad & \alpha < 1 \\ 2\omega_c \text{ wave:} \quad & \alpha < 4 \end{aligned} \tag{2.2}$$

In reality, since operation at cutoff is not possible, the maximum values of α will be slightly less.

The dispersion relation for the extraordinary wave is given by

$$k_\perp^2 c^2 (\omega^2 - \omega_p^2 - \omega_c^2) = (\omega_p^2 - \omega^2)^2 - \omega_c^2 \omega^2 \tag{2.3}$$

Propagation is possible provided either $\omega > \omega_+ = (\omega_c^2 + 4\omega_p^2)^{1/2} + \omega_c$ or $\omega_{UH} > \omega > \omega_-$ where $\omega_{UH} = (\omega_c^2 + \omega_p^2)^{1/2}$ and $\omega_- = (\omega^2 + 4\omega_p^2)^{1/2} - \Omega$. Here ω_{UH} is the upper hybrid resonance frequency, while ω_+ and ω_- are the right-hand and left-hand cutoff frequencies respectively. Since these conditions are functions of ω_c, the profile of the toroidal magnetic field must be taken into account. The results are shown in Fig. 2.1, where the accessibility characteristics of both the ordinary and extraordinary waves are illustrated. In the upper graph one can see the cutoff region that prevents $\omega = \omega_c$ extraordinary wave propagation from the outside. The $\omega = 2\omega_c$

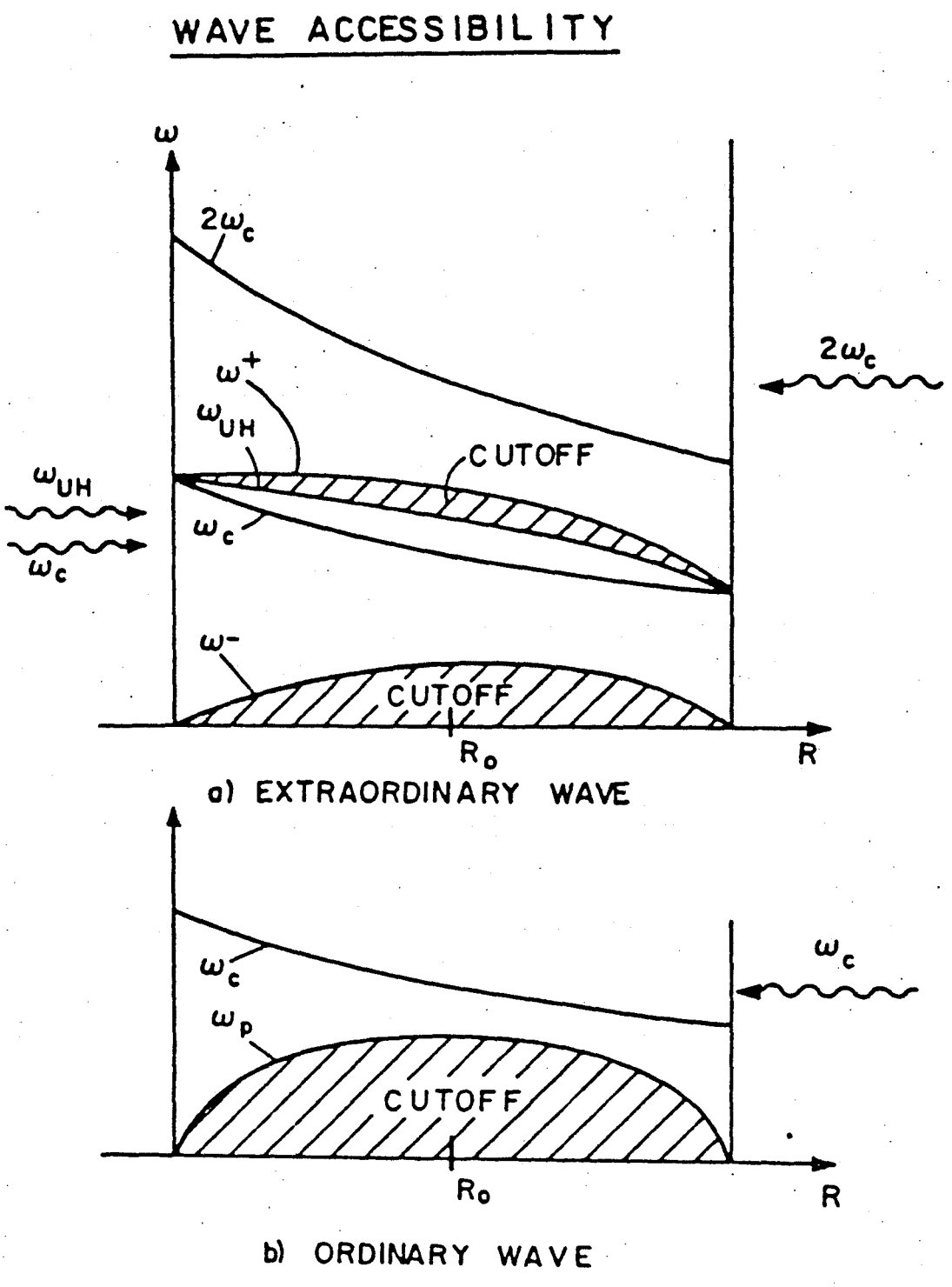

Figure 2.1 Wave Accessibility Diagram

extraordinary wave can reach the center if launched from the inside and if $2\omega_c > \omega_+$, while the $\omega = \omega_c$ wave requires that $\omega_c > \omega_-$. These inequalities can be expressed in terms of α as follows:

$$\begin{aligned} \omega_c \text{ wave:} \quad & \alpha < 2 \\ 2\omega_c \text{ wave:} \quad & \alpha < 2 \end{aligned} \tag{2.4}$$

In addition to accessibility, one must also consider the absorption properties of these waves. An examination of the cold plasma theory for waves propagating in a tokamak shows that these waves will propagate through the cyclotron resonance regions without loss of energy. Linear absorption of energy occurs only when kinetic effects that result from a finite electron temperature are included. Numerical evaluation of the absorption processes [4, 16] indicates that any reasonable reactor grade plasma will be optically thick to all heating modes considered here, with the possible exception of the extraordinary wave at the fundamental cyclotron resonance. In this case the resonant layer may become partially transparent for values of α somewhat less than cutoff. Even here nonlinear absorption or linear mode conversion to the Berstein wave with subsequent damping [17] may take place at the upper hybrid layer (see Fig.2.1).

To be suitable for auxiliary heating, the radiation must also satisfy a startup condition, namely that the plasma be optically thick at a relatively low temperature of 1 or 2 keV. This condition is easily satisfied by all the heating modes except the O-wave at $\omega = 2\omega_c$. For this mode, the optical depth scales as $(T/mc^2)^2$ and as a result the startup capability is marginal, depending sensitively on the time-

varying plasma parameters.

Summarizing, Eqs. (2.2) and (2.4) give the propagation limits based on accessibility of ECR radiation to the plasma center. These conditions can be written in terms of the plasma density and magnetic field on axis:

$$B_0^2 > \frac{m_e n_o}{\varepsilon_0 \alpha_{max}} \tag{2.5}$$

Both the O-wave at the fundamental resonance and the X-wave at $\omega = 2\omega_c$ satisfy constraints imposed by the toroidal geometry and absorption process. The X-wave at $\omega = \omega_c$ may have good absorption properties, but the need to launch the wave from the inside severely complicates the engineering of the reactor. The O-wave at the second harmonic resonance is not absorbed effectively, especially during the startup phase.

These results can now be combined with constraints imposed by ignition and the need for stable operation. The approach followed here differs somewhat from the procedure used by S. M. Wolfe et.al. [18], where the output thermal power was treated as a constant. Here, the plasma radius is fixed, and the minimum plasma density, and subsequently B_o, are determined by the ignition, propagation, and beta limits. The ignition condition is obtained by balancing the energy gain and loss mechanisms of the tokamak. Introducing the empirical scaling law for the global energy confinement time [19]:

$$[n_o \tau_E]_{emp} = 3.8 \times 10^{-21} (n_o a)^2 \ m^{-3} \ s \tag{2.6}$$

where a is the plasma radius, the ignition condition can be written in the following form:

$$an_o \gtrsim \sqrt{MS}\ G(\bar{T}, Z_{eff}) \tag{2.7}$$

where $$MS = \frac{[n_o\ \tau_E]_{emp}}{[n_o\ \tau_E]_{ign}}$$

The function G, which is given in the HFCTR design study [20], depends in a rather complicated manner on the density averaged temperature $\bar{T}$ and on the impurity level of the plasma as measured by Z_{eff}. In general it is a decreasing function of T_o and an increasing function of Z_{eff}. The margin of safety, MS, allows for possible degradation of the empirical τ_E as Eq.(2.6) is scaled from present experimental conditions to reactor plasmas. Such a degradation may result from adverse temperature effects or reduced plasma collisionality.

The beta limit can be expressed as follows

$$\langle\beta\rangle = \frac{\langle\Sigma_j\ n_j\ T_j\rangle}{B_0^2/2\mu_0} \leq \beta_c \tag{2.8}$$

where the summation includes all plasma species present (e.g., ions, electrons, alpha particles, etc.). The critical beta, β_c, is presently thought to be determined by the appearance of ballooning modes which disrupt the plasma [3]. However, the exact value of β_c, or whether even such a limit exists, is not presently known. In this analysis a critical beta $\beta_c = 0.04$ will be assumed for a plasma with an aspect ratio of 5.

Using the ignition condition, Eq.(2.7), to determine the density, the minimum magnetic field satisfying both the propagation and the beta limits can be calculated. An example is shown in Fig. 2.2 where the minimum B_o has been plotted versus $\bar{T}$ for the $\omega = \omega_c$ ordinary wave heating mode ($\alpha < 1$). The plasma is assumed to have parabolic temperature and density profiles, a q of 3, and an aspect ratio of 5 (HFCTR parameters). The margin of safety is 2. Also shown is the operating frequency of the gyrotron corresponding to each value of B_o. The O-wave mode was chosen because it results in lower gyrotron frequencies than the $2\omega_c$ X-wave mode. It can be seen that each curve consists of two parts. In the low temperature region the propagation limit is the most restrictive, and results in the minimum B_o being a decreasing function of $\bar{T}$. In the high $\bar{T}$ region the beta limit becomes the dominating constraint. This graph suggests that the gyrotron frequency regime for a commercial reactor is approximately 100 - 300 GHz. Under the most optimistic conditions (MS = 1), one can show that a compact reactor ($a \leq 1.5$ m) would require gyrotrons with $\nu \gtrsim 140$ GHz, relatively high compared to today's CW experiments. As one might expect, increasing the margin of safety or decreasing the plasma radius causes n_o and subsequently ν to increase. The curves shown can be scaled to other safety margins and radii using Eq.(2.7).

If the beta limit proves to be less restrictive than $\beta_c = 4\%$, or even nonexistent, then the higher $\bar{T}$ segment of each curve in Fig. 2.2 will shift downward. This results in lower values of ν, and causes the optimum temperature to increase. However, even if the beta constraint were neglected altogether, the propagation constraint alone would set a

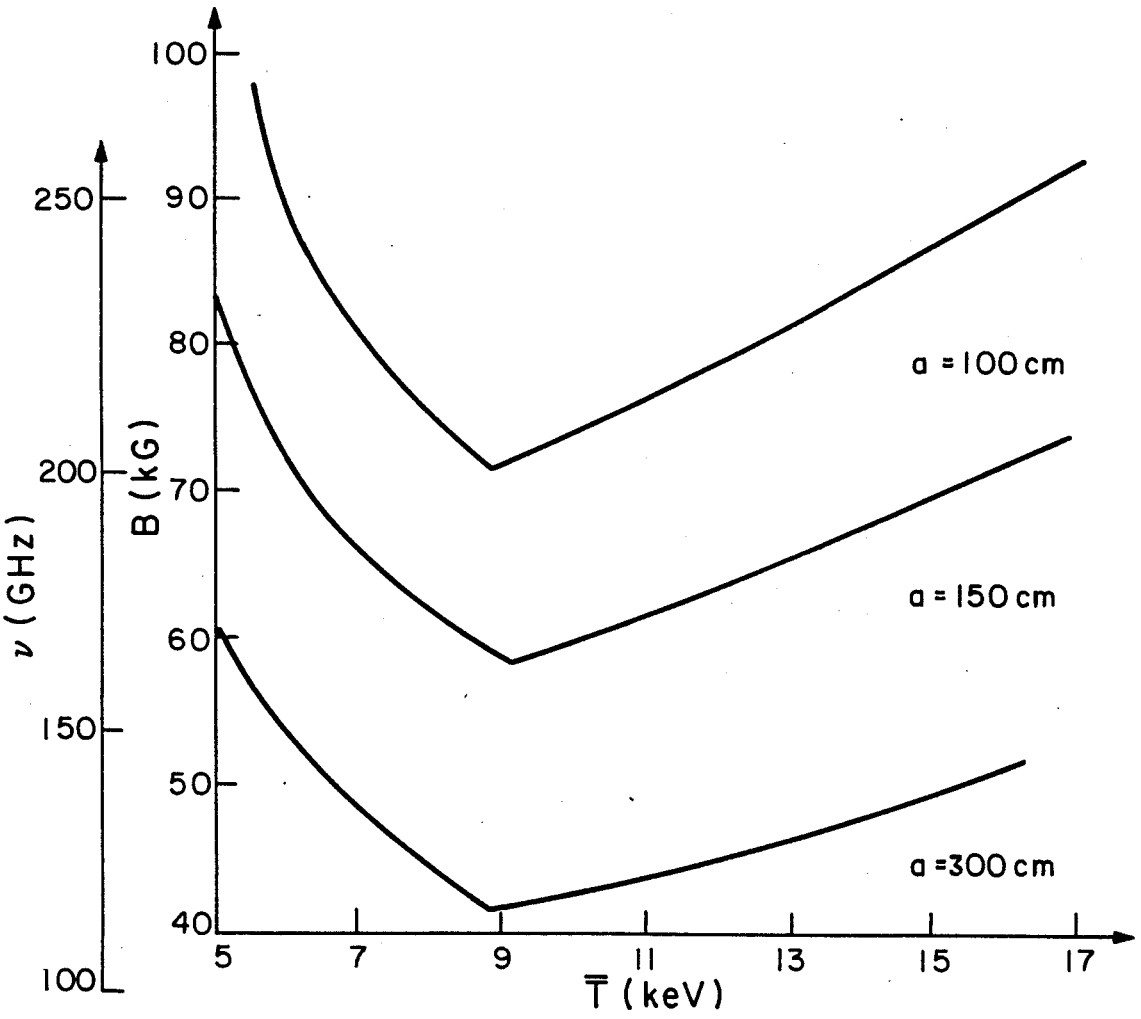

Figure 2.2 Minimum toroidal magnetic field and gyrotron frequency for a plasma with q=3 and an aspect ratio of 5. MS=2 and β_c=4% .

lower limit on ν. For example, for a = 1.0 m, ν could be no less than 175 GHz if one scaled the propagation condition to higher $\bar{T}$.

An operating regime can be determined if the limitations imposed by the neutron power flux through the first wall is included. This places an upper limit on the density at a given temperature and plasma radius, and then B_o can be calculated using the beta and propagation constraints. In a similar manner the total output power corresponding to each value of B_o and $\bar{T}$ can be calculated. For the MS = 2 and a = 1.5 m curve of Fig. 2.2, a wall loading less than 4 MW/m^2 would restrict $B_o \lesssim 78$ kG at $\bar{T}$ = 9 keV. At this same temperature, a thermal output of 1500 MW corresponds to a magnetic field of 65 kG.

Fig. 2.2 suggests that the optimum temperature occurs when the beta and propagation curves intersect. This is equivalent to combining Eqs. (2.5) and (2.8), which leads to the following expression:

$$\bar{T}_{opt}(\text{keV}) = \frac{232\ \beta_c}{\alpha_{max}} \tag{2.9}$$

where the alphas are assumed to contribute 20% to the total plasma pressure. For the parameters of Fig. 2.2 this gives a temperature of 9.3 keV. If this equation is used to select the temperature, then it is possible to graph the minimum B_o as a function of MS and a. This is shown in Fig. 2.3 for the $\omega = \omega_c$ ordinary wave heating mode.

It should be remembered that these results pertain to a power reactor operating at the ignition point. One must also investigate the accessibility and stability requirements during the startup phase in

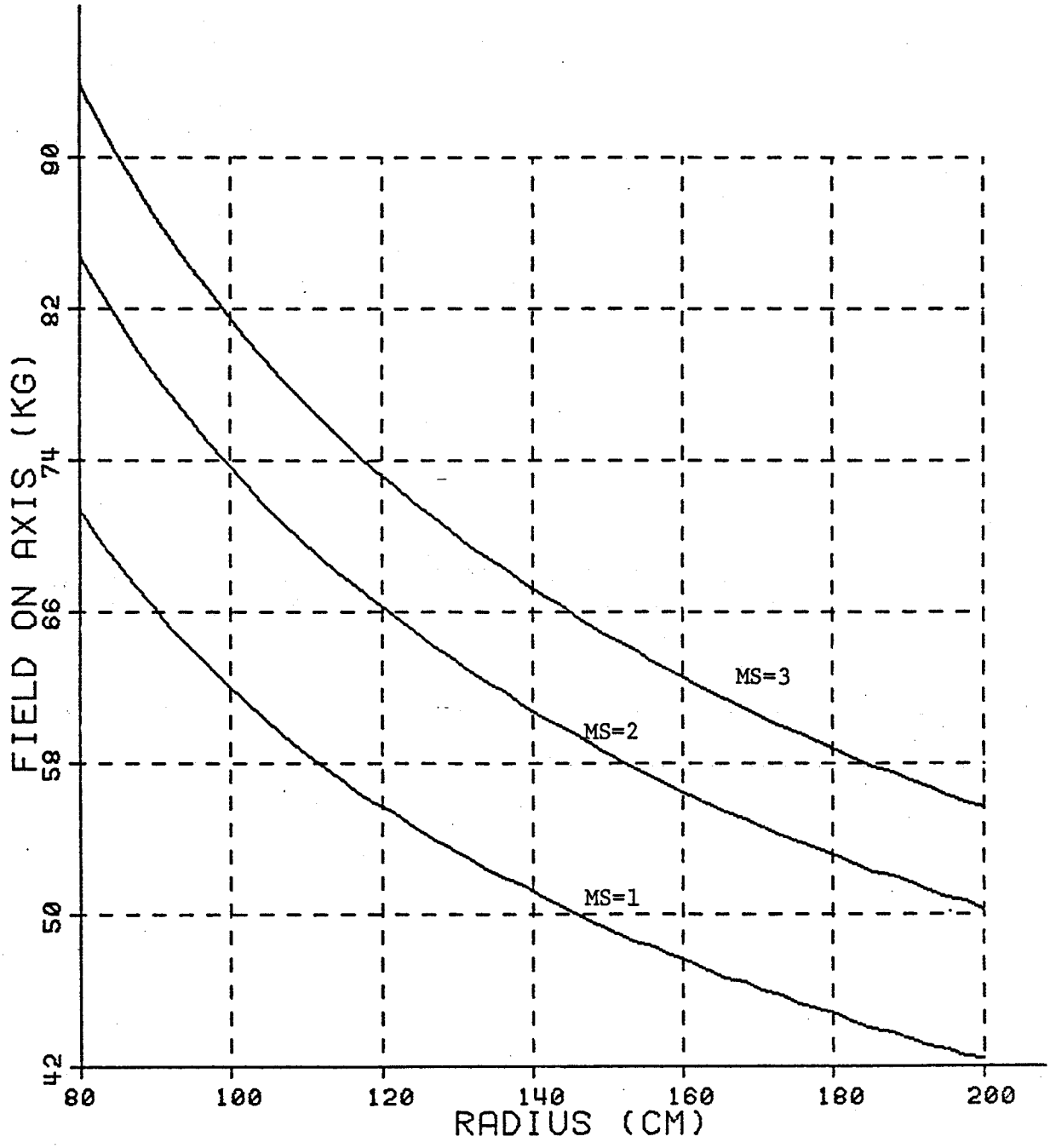

Figure 2.3 Minimum field as a function of the margin of safety. Temperature has been optimized according to Eq.(2.9)

order to determine the minimum ν need for ECR bulk heating. It can be shown that the ignition point corresponds to the most restrictive conditions, and thus determines ν, if the plasma density and temperature during startup are always less than the values of these parameters at ignition as determined by Eq. (2.7). The propagation and beta limits can be expressed as $B_o^2 \geq K_1 n_o$ and $B_o^2 \geq K_2 n_o T_o$ respectively, where K_1 and K_2 are constants. Obviously, depending on which condition is the most restrictive, the highest value of n_o or $n_o T_o$ determines the minimum B_o and consequently the lower limit of ν. Since both n_o and $n_o T_o$ reach their highest values at ignition, the ignition density and temperature must determine the minimum value of ν which satisfies both the beta and propagation limits during the startup sequence.

Summarizing, the analysis outlined here indicates that ordinary wave heating at $\omega = \omega_c$ appears to be the best heating mode of the four modes examined. It exhibits good absorption and can be launched from the outboard side of the torus. In addition, it requires lower ECRH frequencies than the other viable mode, X-wave heating at $\omega = 2\omega_c$. Fig. 2.3 shows that if a conservative beta limit of $\beta_c = 4\%$ is assumed, and the confinement law is expected to degrade somewhat when scaled to reactor conditions (MS = 2), then 60 kG will be required for $a \leq 1.5$ m. The presence of impurities will also result in the need for higher magnetic fields in order to utilize ECRH. Hence, it is likely that the development of high frequency ($\geq$ 170 GHz) gyrotron sources will be necessary in order to use ECRH to heat tokamak power reactors.

Chapter 3

Linear Theory of a Gyrotron

In this chapter the linear theory of a gyrotron, which describes the characteristics of this device at threshold, is derived. Expressions are obtained for the starting current I_{st} and the detuning of the operating frequency from the empty cavity resonance frequency. In general, linear theory results can be expressed in analytic form, as will be the case here. In contrast, the nonlinear theory, which describes the operation of the maser above threshold and yields the output power and efficiency of the device, must ordinarily be solved numerically. A linear analysis provides a means of quickly determining the basic operational characteristics of the gyrotron, thus making it an important tool in the examination of this device.

There have been a number of previous investigations of the linear theory of the ECM [24-29]. However, these studies have been limited or idealized in one respect or another, such as by treating only specific cavity modes or electron beams with no velocity spread. In this chapter, an analytic treatment of ECM linear theory that is applicable to all TE modes of the cavity, as well as to an arbitrary, weakly relativistic, electron velocity distribution, is derived. Furthermore, the results presented are valid for any distribution of the longitudinal RF field. This allows one to compare the linear characteristics of different models of an ECM cavity, including: an idealized right circular cylinder cavity with closed ends and sinusoidal longitudinal RF field; and a more realistic cavity with open ends and a Gaussian distribution. In addition, the present comprehensive results can be used to evaluate

important effects in an ECM, including mode competition and changes caused by a velocity spread in the electron beam. By analyzing these effects, those factors that strongly influence the threshold behavior of an ECM can be determined.

The method employed in this analysis involves solving the combined Vlasov and Maxwell equations for an electron beam interacting with the RF fields of a cavity. The Vlasov equation is solved by a standard perturbation approach in the weakly relativistic limit. The results are then combined with the Slater equations for the cavity modes and solved for the oscillation condition. This yields expressions for both the starting current and the frequency detuning. Calculation of the starting current allows one to determine the minimum beam current needed for self-oscillation. The frequency detuning, which depends on the cavity Q, may provide a means of determining Q experimentally.

This analysis is presented in the following manner. In Section 1, the problem is formulated and general expressions for the starting current and frequency detuning are presented. In Section 2, the results of this linear derivation are described in detail and applied to three different longitudinal RF field profiles: uniform, sinusoidal, and Gaussian. This comparison allows one to determine the sensitivity of the threshold behavior of an ECM to the field structure. The effect of beam quality will also be investigated. In Sections 3 through 6, this linear analysis will be utilized in conjunction with a variety of key problems associated with the operation of a gyrotron. These problems, in the order of their presentation, are: i) Field profiling and its use in lowering the threshold current, ii) The extension of this theory to higher harmonics, iii) Mode competition, iv) Startup behavior of a gyrotron.

3.1 General Theory

The formulation used for describing the ECM consists of a combination of the Vlasov equation for the electron distribution function and Maxwell equations for the RF cavity fields. A number of assumptions are made that aid in simplifying the calculation without severely limiting its usefulness. We are concerned with the small signal (i.e., linear) operation of an ECM. The cavity is assumed to have a cross-sectional shape that is uniform or slowly varying along its axis, here chosen as the z-axis. This allows one to solve the Helmholtz equation, which describes the field structure within the cavity, by a separation of variables. The RF field can then be expressed as a product of two functions, one describing the cross-sectional structure and the other giving the field variation along z. Space charge effects are neglected. The electron beam is assumed to be weakly relativistic, with relativistic effects included in the calculation by retaining the velocity dependence of the electron mass m_e and the cyclotron frequency ω_c. The dependence of ω_c on velocity is crucial in order for emission to occur. Finite Larmor radius effects are neglected, and as a consequence the results presented in this section are applicable only to an ECM operating at the fundamental frequency, i.e., $\omega \simeq \omega_c$.

This calculation will include only the interaction between the beam and the RF electric field, and will neglect the RF magnetic field. Results from a previous paper [29] indicate that the terms associated with the magnetic field are small if $\omega_c / k_{||} c >> 1$, where $k_{||}$ is the wavenumber parallel to the z-axis. Since a gyrotron

operates near cutoff and satisfies the above inequality, this analysis is especially applicable to this device. This same condition also results in TE modes having substantially higher gain than TM modes, and for this reason the latter will not be treated here.

In order for the initial electron distribution function to be in equilibrium, it must satisfy the zero-order Vlasov equation with $\partial f_o/\partial t = 0$ (See Eq. (B.2)). It can be shown that such an equilibrium exists if this distribution can be expressed as a function of only the constants of the motion [28,38,85-6]. For a gyrotron these constants are the electron velocities parallel and perpendicular to the z-axis, u and w respectively, and the canonical angular momentum. In general this results in a distribution function in which the spatial and velocity dependences are not separable. An analysis of the equilibrium Vlasov equation shows that such a separation is possible if the Larmor radius r_L is much smaller than the characteristic spatial dimension of the distribution function.

For a gyrotron operating at the fundamental, it is possible to model f_o as a separable function of the spatial and velocity coordinates if r_L is much smaller than the characteristic wavelength of the perturbation, which in this case is the TE mode. Since the characteristic dimension of this perturbation is R_o/p for a TE_{op1} mode, where R_o is the cavity wall radius, this condition can be expressed mathematically as $\nu_{mp}/p >> w/c$, where ν_{mp} is the transverse mode index (for a cylindrical cavity ν_{mp} is the p^{th} zero of $J_m'(y) = 0$). For higher harmonic interactions (see Section 3.4), this assumption can be generalized by saying that $\partial^n \bar{E}/\partial \bar{r} << r_L$, where n is the harmonic number. This condition

is easily satisfied by the gyrotron and as a result the function f_o is written in this analysis as:

$$f_o(\bar{r},\bar{v},t = 0) = N(R_e,\theta_e)\ f_o(u,w) \tag{3.1}$$

where

$$2\int_{-\infty}^{\infty} du \int_{0}^{\infty} w\ dw\ f_o(u,w) = 1$$

and $N(R_e,\theta_e)$ is the spatial density of the beam, and is expressed in terms of the coordinates of the electron gyrocenter. This model of f_o as a superposition of particles with arbitrary guiding centers and velocities is found to be consistent with computer models of electron trajectories in a gyrotron, and greatly simplifies the final analytic results. One should note, however, that this model is applicable only because space charge effects, and consequently the self-fields of the beam, have been neglected.

This analysis begins with a Slater expansion [30] of the RF vacuum field within the cavity in terms of orthonormal modes:

$$\bar{E}(\bar{r},t) = \sum_{\ell} p_\ell(t)\bar{E}_\ell(\bar{r})$$

$$\bar{H}(\bar{r},t) = \sum_{\ell} q_\ell(t)\bar{H}_\ell(\bar{r}) \tag{3.2}$$

where the field components have been written as sums of orthonormal modes that satisfy:

$$\int_V d^3r\ \bar{E}_\ell \cdot \bar{E}_d = \int_V d^3r\ \bar{H}_\ell \cdot \bar{H}_d = \delta_{\ell d}$$

Here, V is the cavity volume, $\omega_\ell = ck_\ell$ is the vacuum frequency of the mode, and $p_\ell(t)$ and $q_\ell(t)$ describe the amplitudes and time dependences of the field components. Writing Maxwell's equations $\nabla \times \bar{E} = -\mu_o \partial\bar{H}/\partial t$ and $\nabla \times \bar{H} = \bar{J} + \varepsilon_o \partial\bar{E}/\partial t$ in terms of the above expansions, combining these two equations, and utilizing the orthogonal characteristics of $\bar{E}_\ell$ and $\bar{H}_\ell$ leads to an expression describing the time-dependent behavior of the ℓ^{th} mode [30]:

$$\frac{1}{c^2}\ \frac{d^2p_\ell}{dt^2} + k_\ell^2\ p_\ell = -\mu_o \frac{d}{dt}\left(\int_V d^3r\ \bar{J}\cdot\bar{E}_\ell - \int_{S'} dA(\hat{n} \times \bar{H})\cdot\bar{E}_\ell \right) - k_\ell \int_S dA\ (\hat{n} \times \bar{E})\cdot\bar{H}_\ell \qquad (3.3)$$

where $\hat{n}$ is a vector normal to the cavity surface and pointing outward. The multimode nature of this problem is embodied in the fact that $\bar{J}, \bar{E}$, and $\bar{H}$ must be expanded in terms of all possible cavity modes.

The surfaces S and S' represent two types of boundary conditions that are present. The S surface corresponds to the conducting walls of the cavity at which the tangential component of $\bar{E}$ is virtually zero. The S' surface corresponds to an insulated area and is associated with power coupled out of the cavity. The S integral can be rewritten in terms of the ohmic quality factor of the cavity, Q_o, by noting that $\hat{n} \times \bar{E} = \bar{H}(1 + i)\sqrt{\omega\mu_o/2\sigma}$ at a wall with conductivity σ. Using the following definition for $Q_o^{\ell d}$:

$$Q_o^{\ell d} = \sqrt{2\omega\sigma\mu_o}\left(\int_S dA\ \bar{H}_\ell \cdot \bar{H}_d \right)^{-1}$$

the S integral in Eq.(3.3) can be written as:

$$\int_S dA(\hat{n} \times \bar{E})\cdot\bar{H}_\ell = (i - 1) \sum_d \left(\frac{k_d}{Q_o^{\ell d}}\right) p_d \tag{3.4}$$

Here $Q_o^{\ell d} >> 1$ has been assumed and terms of order $(Q_o^{\ell d})^{-2}$ have been dropped. The terms associated with $Q_o^{\ell d}$, $d \neq \ell$, which represent a coupling between cavity modes, are typically small in a gyrotron and can be neglected.

The S' integral can be expressed in terms of the diffractive Q, Q_D, that results from the output coupling of the cavity mode:

$$\int_{S'} dA(\hat{n} \times \bar{H})\cdot\bar{E}_\ell = - \varepsilon_o \left(\frac{\omega_\ell}{Q_D^\ell}\right) p_\ell \tag{3.5}$$

The superscript on Q_D indicates that this parameter is defined in terms of the stored energy in the ℓ^{th} mode and the power coupling between the ℓ^{th} mode of the cavity and the output mode of the waveguide connected to the cavity. No mode coupling terms are obtained from this integral. Combining Eqs. (3.3), (3.4), and (3.5) leads to the following result:

$$\frac{1}{c^2}\frac{d^2 p_\ell}{dt^2} + k_\ell^2 p_\ell = - \mu_o \frac{d}{dt}\left[\int_v d^3 r \bar{J}\cdot\bar{E}_\ell + \varepsilon_o\left(\frac{\omega_\ell}{Q_D^\ell}\right) p_\ell\right]$$

$$- (i - 1)\left(\frac{k_\ell^2}{Q_o^{\ell\ell}}\right) p_\ell \tag{3.6}$$

If an equilibrium exists within the cavity, it is possible to express this equation as two separate relations, one describing the energy balance within the cavity while the other determines the frequency detuning. Writing $p_\ell = p_{o\ell}\exp[i\omega(\ell)t]$, where $p_{o\ell}$ is independent of time, the decoupled expressions are:

$$\left(\frac{\omega_\ell}{Q_T^\ell}\right) = -\frac{1}{\varepsilon_o}\,\mathrm{Re}\left[\frac{1}{P_{o\ell}}\int_v d^3r\ \bar{J}\cdot\bar{E}_\ell\right] \tag{3.7a}$$

$$\left(\omega'_\ell\right)^2 - \left(\omega(\ell)\right)^2 = \frac{\omega(\ell)}{\varepsilon_o}\,\mathrm{Im}\left[\frac{1}{P_{o\ell}}\int_v d^3r\ \bar{J}\cdot\bar{E}_\ell\right] \tag{3.7b}$$

where

$$Q_T^\ell = \frac{Q_D^\ell\, Q_o^{\ell\ell}}{Q_D^\ell + Q_o^{\ell\ell}}$$

$$\omega'_\ell = \omega_\ell\sqrt{1 - (Q_o^{\ell\ell})^{-1}}$$

Here Q_T^ℓ is the overall quality factor, and $\omega(\ell)$ is the operating frequency of the ℓ^{th} mode, which generally differs from ω_ℓ.

For a cylindrical cavity with no taper and an arbitrary cross section, the electric field of a single TE mode in equilibrium can be written as [40]:

$$\bar{E}(\bar{r},t) = \bar{T}(r,\theta)g(z)\exp(i\omega t) \tag{3.8}$$

where $\bar{T}(r,\theta)$ and $g(z)$ satisfy:

$$\bar{T}(r,\theta) = \hat{z} \times \nabla_\perp \Psi$$

$$d^2g(z)/dz^2 + k_{||}^2\, g(z) = 0 \qquad (3.9)$$

$$k_\perp^2 + k_{||}^2 = \omega^2/c^2$$

$$\nabla_\perp^2 \Psi + k_\perp^2 \Psi = 0$$

Here $\hat{z}$ is a unit vector, Ψ is determined by the boundary conditions, and $k_\perp$ and $k_{||}$ are constants. $\bar{T}(r,\theta)$ gives the field amplitude and cross-sectional structure, and can be complex, while $g(z)$ is real and describes the longitudinal field profile. In addition $g(z)$ is normalized to a maximum value of one. It can be shown that Eqs. (3.8) and (3.9) also apply to cavities with weakly irregular features at the ends for output coupling, or with slowly tapered cross sections, if we allow $k_\perp$, $k_{||}$, and Ψ to become functions of z [31,41]. The dependence of $\bar{T}$ on z will be relatively weak for these cavities, and can be neglected.

An expression can be obtained for $P_{o\ell}$ by equating Eqs. (3.2) and (3.8) squaring and integrating over the cavity volume. This gives:

$$|P_{o\ell}|^2 = \int_V d^3r\, |g_\ell(z)\, \bar{T}_\ell(r,\theta)|^2 \qquad (3.10)$$

The parameter $p_{o\ell}$ serves as a normalization factor in Eqs.(7) so that, in a single mode analysis, the starting current and detuning are independent of field amplitudes. Also noteworthy is the fact that $(\varepsilon_o p_{o\ell}^2/2)$ is equal to the total stored energy (electric plus magnetic RF fields) within the cavity in the ℓ^{th} mode.

3.1.1 Equations for Single Mode Operation

The integrals in Eqs. (3.7) must now be solved. In general, $\bar{J}$ is written in terms of all modes existing within the cavity. However, we will initially limit our attention to a single oscillating TE mode and leave the discussion of multimoding to a later section. Starting with the linearized Vlasov and Maxwell equations, the perturbation $f_1(\bar{r},\bar{v},t)$ of the distribution function of the electron beam due to the RF electric field in the cavity can be calculated using the method of characteristics [33]. This method is appropriate as long as the perturbation is small, that is, the field amplitude is small. An expression for $\bar{J}$ can be derived based on this perturbed distribution. The approach followed is described in detail in Appendix B, and only the final results are presented here. The integrals of Eqs. (3.7) can be expressed in the following form:

$$\frac{1}{P_{o\ell}}\int_v d^3r\ \bar{J}\cdot\bar{E}_\ell = \frac{-e}{P_{o\ell}}\int_v d^3r\ N(r,\theta)\int d^3v\ \bar{E}_\ell\cdot\bar{v}\ f_1(\bar{r},\bar{v},t)$$

$$= |P_{o\ell}|^{-2}\frac{e^2}{\gamma m_e}\frac{\pi}{k_{||}^2}\int_{-\infty}^{\infty} du\int_o^{\infty} dw\ f_o(u,w)\left(\frac{w}{u}\right)\left[1-\frac{1}{2}\left|\frac{sw^2}{c^2}\right|\frac{d}{dx}\right]$$

$$\cdot\left[(F_c^{\ell\ell}+i\,F_s^{\ell\ell})(G_D^{\ell\ell}-iG_c^{\ell\ell})\right] \qquad (3.11)$$

where

$$G_D^{\ell d} = \int_o^{2\pi} d\theta_e\int_o^{R_o} R_e\ dR_e\ N(R_e,\theta_e)(\bar{T}_\ell\cdot\bar{T}_d^*)$$

$$G_C^{\ell d} = \int_o^{2\pi} d\theta_e \int_o^{R_e} R_e \, dR_e \, N(R_e, \theta_e)(\bar{T}_\ell \times \bar{T}_d \cdot \hat{z})$$

$$x_\ell = \frac{\left[\omega_c - \omega(\ell)\right]}{k_{||} u}$$

$$s = \frac{\omega_c}{k_{||} u}$$

$$\omega_c = \frac{eB_o}{m_e \gamma}$$

Here, γm_e is the relativistic electron mass, R_o is the cavity radius, and e is the electron charge. The strength of the interaction between the beam and the RF field is measured by the geometric factors G_D and G_C. The expression $\left[1 - (1/2)(sw^2/c^2)d/dx\right]$ operates on the functions $F_c^{\ell\ell}$ and $F_s^{\ell\ell}$. These functions are determined by the longitudinal field dependence g(z), and can be calculated from the following equations:

$$F_c^{\ell d}(x_d) = \int_{-\infty}^{\infty} d\tilde{z} g_\ell(\tilde{z}) \int_o^{\infty} d\lambda g_d(\tilde{z} - \lambda) \cos(\lambda x_d) \qquad (3.12a)$$

$$F_s^{\ell d}(x_d) = \int_{-\infty}^{\infty} d\tilde{z} g_\ell(\tilde{z}) \int_o^{\infty} d\lambda g_d(\tilde{z} - \lambda) \sin(\lambda x_d) \qquad (3.12b)$$

where $\tilde{z} = k_{||} z$. In the next section, detailed results will be presented for specific g(z) distributions. The derivative in Eq. (3.11) results

from the dependence of γ, and consequently ω_c, on velocity, and is a measure of the electron bunching process.

We will now specialize to an annular electron beam that is symmetric in θ, has no radial thickness, and is located at $r = R_e$. We will limit our attention to an RF field with a standing wave structure in the θ direction, so that $\bar{T}_\ell$ is real and $G_c^{\ell\ell}$ is zero. Relating N to the beam current I, the geometric factor $G_D^{\ell\ell}$ can be written as:

$$G_D^{\ell\ell} = (I/e\bar{u})G(R_e)$$

where (3.13)

$$G(R_e) = \frac{1}{2\pi}\int_0^{2\pi} d\theta \; |\bar{T}_\ell(R_e,\theta)|^2$$

and $\bar{u}$ is the average longitudinal velocity. An explicit expression can now be written for the starting current I_{ST} by combining Eqs. (3.7a) (3.11), and (3.12). For clarity, the ℓ script has been dropped from all parameters except frequencies:

$$I_{ST} = -\varepsilon_o \frac{\omega_\ell}{Q_T} |p_o|^2 \frac{m_e}{e} \frac{\gamma k_{||}^2 \bar{u}}{\pi G(R_e)} \left\{ \int_{-\infty}^{\infty} du \int_o^{\infty} dw \; f_o(u,w)\left(\frac{w}{u}\right)\left[F_c - \frac{1}{2}\left(\frac{sw^2}{c^2}\right)\frac{dF_c}{dx}\right]\right\}^{-1} \tag{3.14}$$

The starting current is positive and emission is possible only when $(sw^2/c^2)(F_c)^{-1}(dF_c/dx) > 2$.

A simple expression can also be obtained for the frequency detuning by dividing (3.7b) by (3.7a). Defining $y \equiv (\omega_c - \omega_\ell)(k_{||}\, u)^{-1}$ and assuming $|\omega_c - \omega_\ell| << \omega_\ell$, one can write:

$$\left(\frac{2Q_T}{s}\right)\left(y - x + \frac{s}{2Q_o} - \frac{y}{2Q_o}\right) = \frac{\int_{-\infty}^{\infty} du \int_0^{\infty} dw f_o(u,w)\left(\frac{w}{u}\right)\left[F_S - \frac{1}{2}\left(\frac{sw^2}{c^2}\right)\frac{dF_s}{dx}\right]}{\int_{-\infty}^{\infty} du \int_0^{\infty} dw f_o(u,w)\left(\frac{w}{u}\right)\left[F_c - \frac{1}{2}\left(\frac{sw^2}{c^2}\right)\frac{dF_c}{dx}\right]} \tag{3.15}$$

Eqs. (3.14) and (3.15) can be further simplified by assuming that the electron beam has no velocity spread and f_o can be represented by delta functions: $f_o(u,w) = (2\pi w_o)^{-1}\,\delta(u - u_o)\,\delta(w - w_o)$. This leads to the following set of equations:

$$I_{ST} = -2\varepsilon_o \frac{\omega_\ell}{Q_T} |p_o|^2 \frac{\gamma m_e}{e} \frac{(k_{||} u_o)^2}{G(R_e)} \left[F_c - \frac{1}{2}\left(\frac{sw_o^2}{c^2}\right)\frac{dF_c}{dx}\right]^{-1} \tag{3.16a}$$

$$\left(\frac{2Q_T}{s}\right)\left(y - x + \frac{s}{2Q_o}\right) = \frac{F_s - \frac{1}{2}\left(\frac{sw_o^2}{c^2}\right)\frac{dF_s}{dx}}{F_c - \frac{1}{2}\left(\frac{sw_o^2}{c^2}\right)\frac{dF_c}{dx}} \tag{3.16b}$$

Note that I_{ST} is independent of the field amplitude, as is expected in linear theory. The term $y/2Q_o$ has been dropped in Eq. (3.16b) since it is very small in comparison to the other terms.

It can be seen that F_c and F_s, which are defined by Eq. (3.12), are crucial in determining the characteristics of the starting current and detuning. A simple expression can be obtained for F_c by writing it in terms of the Fourier transform of $g(\tilde{z})$. Using the transform:

$$\mathfrak{L}(k) = (2\pi)^{-\frac{1}{2}} \int_{-\infty}^{\infty} g(a)\, e^{ika}\, da$$

in conjunction with Eq.(12a) gives (see Appendix B)

$$F_c = \pi \mathcal{L}_\ell(x)\, \mathcal{L}^*_\ell(x) \tag{3.17}$$

Using Eq. (3.11), one can show that F_s can be expressed in terms of F_c using the Kramers-Kronig relations [38]:

$$F_s = \pi^{-1} P \int_{-\infty}^{\infty} \frac{F_c(a)}{x-a}\, da \tag{3.18}$$

where P indicates the principal value of the integral. These two equations, in conjunction with (3.16), provide a convenient means of quickly determining the linear characteristics of an ECM. Moreover, because of the simple nature of these expressions, the possibility exists of defining the desired linear characteristics of an ECM, and then calculating the appropriate longitudinal field structure via these relations.

The functions $F_c(x)$ and $F_s(x)$ are very similar to the absorption and dispersion functions of a forced harmonic oscillator. Thus, it is possible to model the ECM interaction as a harmonic oscillator with natural frequency ω_c and a driving force due to the RF field with frequency ω. The damping time τ_d, which is inversely related to the resonance width, can be shown to be approximately equal to the time of interaction between the beam and RF field, $\tau_i \sim L/u$. If $\omega \neq \omega_c$, then the electron will precess with respect to the field, experiencing alternating periods of acceleration and deceleration. If the interaction continues indefinitely, $(\tau_i \to \infty)$, then the net

electron energy change will be zero. In this case, an energy transfer to the electrons will occur only at $\omega = \omega_c$, and the resonance curve becomes a delta function located at $\omega = \omega_c$. However, if τ_i is finite, the periods of acceleration and deceleration will not exactly cancel for $\omega \neq \omega_c$, and the resonance curve will be broadened. The relationship between τ_d and τ_i can also be shown by noting that $F_c(x)$ typically has a width $\Delta x \sim 2$. Thus one can write:

$$\tau_d^{-1} = \frac{\Delta\omega}{2\pi} \simeq \frac{2k_{\parallel} u}{2\pi} = \frac{u}{L} = \tau_i^{-1}$$

This broadening mechanism is often called transit time broadening.

3.2 Results for Specific Cavity Field Structures

The general theory just derived will now be applied to specific longitudinal field structures in order to determine the sensitivity of a gyrotron to g(z). A cavity of length L and circular cross section will be assumed. For a thin annular electron beam of radius R_e and a standing RF wave in the θ direction, the starting current and frequency detuning are given by Eqs.(3.16) in the case of no electron velocity spread.

Three specific longitudinal profiles will be considered: sinusoidal, Gaussian, and uniform. A sinusoidal distribution is associated with a nontapered cavity with conducting walls at each end. In reality, such a description is inadequate since an ECM normally consists of an open resonator in which the field, rather than ending abruptly, extends beyond the ends of the cavity in order to achieve output coupling. If one wishes to calculate g(z) exactly, the Helmholtz equation must be

solved with the appropriate boundary conditions. However, a Gaussian distribution is a reasonably good approximation for the profile, and compares well with both exact numerical solutions for a variety of open cavities [31], and experimental measurements [32]. A Gaussian profile can be expressed as $g(z) = \exp\left[-(k_{\|} z)^2\right]$, where $k_{\|} = 2/L_{eff}$ and L_{eff} is determined by the shape and length of the cavity. $\bar{T}(r,\theta)$ as calculated for a nontapered cavity will be used to describe the transverse field structure under the assumption that, for a cavity operating near cutoff, any taper will be small and the dependence of $\bar{T}$ on z can be neglected.

A uniform field, $g(z) = 1$, that extends from $z = -L/2$ to $L/2$ will also be considered. Such a distribution might be used to describe a long cavity in which the resonant interaction only occurs in the central part of that cavity. As in the case of the Gaussian, the $\bar{T}(r,\theta)$ of a nontapered cavity will be utilized.

In order to calculate the starting current and detuning, one must determine the functions F_c, F_s, $|p_o|^2$, and $G(R_e)$. For the three longitudinal field distributions discussed here, the expressions for F_c, F_s, and $|p_o|^2$, derived using Eqs. (3.17), (3.18), and (3.10) respectively, are given in Table 3.1. The first column gives $g(z)$, as well as the definition of $k_{||}$ and the range of interaction between the electron beam and RF field. The sinusoidal and uniform distributions involve interactions over a finite distance L, whereas the Gaussian interaction extends from $z = -\infty$ to ∞. In the case of the uniform field, where $g(z)$ is independent of $k_{||}$, the definition of $k_{||}$ is arbitrary and does not affect the final results.

The geometric factor $G(R_e)$ and $|p_o|^2$ are calculated using Eqs.

TABLE 3.1

Results for Various Longitudinal Field Distributions g(z)

g(z)	$F_c(x)$	$F_s(x)$	$\lvert P_0\rvert^2$
(1) $\sin k_{\parallel} z$ $k_{\parallel} = q\pi/L$ $0 \le z \le L$	$\frac{2}{(1-x^2)^2} \sin^2\left(\frac{(x+1)\pi q}{2}\right)$	$\frac{-1}{(1-x^2)^2}\left[\sin q\pi(x-1) + \frac{x(1-x^2)q\pi}{2}\right]$	$\frac{\pi L}{4} k_{\perp}^{-2}\left[\nu_{mp}^2 - m^2\right] J_m^2(\nu_{mp})$
(2) $e^{-k_{\parallel}^2 z^2}$ $k_{\parallel} = 2/L_{eff}$ $-\infty \le z \le \infty$	$\frac{\pi}{2} e^{-\frac{x^2}{2}}$	$\sqrt{\pi}\ D\left(\frac{x}{\sqrt{2}}\right)$	$(\frac{\pi}{2})^{\frac{3}{2}} \frac{L_{eff}}{2} k_{\perp}^{-2}\left[\nu_{mp}^2 - m^2\right]$ $\times\ J_m^2(\nu_{mp})$
(3) 1 $k_{\parallel} = \pi/L$ $-\frac{L}{2} \le z \le \frac{L}{2}$	$2\left[\frac{\sin^2 \frac{x\pi}{2}}{x^2}\right]$	$\frac{\pi}{x} - \frac{\sin(\pi x)}{x^2}$	$(\frac{\pi}{2}) L k_{\perp}^{-2}\left[\nu_{mp}^2 - m^2\right] J_m^2(\nu_{mp})$

$D(x) = e^{-x^2}\int_0^x e^{\alpha^2} d\alpha$ Dawson's Integral

$|P_0|^2$ corresponds to a standing wave in the θ direction

(3.13) and (3.10) respectively, where $\bar{T}(r,\theta)$ is given by Eq. (3.9) for a TE_{mpq} mode with a standing wave in the θ direction:

$$\bar{T}(r,\theta) = \hat{r}\left(\frac{m}{k_\perp r}\right) J_m(k_\perp r)\begin{Bmatrix}\sin m\theta\\ -\cos m\theta\end{Bmatrix} + \hat{\theta}\ \frac{1}{k_\perp}\frac{dJ_m(k_\perp r)}{dr}\begin{Bmatrix}\cos m\theta\\ \sin m\theta\end{Bmatrix} \tag{3.19}$$

Here J_m is a Bessel function of order m, and $\hat{r}$ and $\hat{\theta}$ are unit vectors. Boundary conditions yield $k_\perp = \nu_{mp}/R_o$ and $k_\parallel = q\pi/L$, where ν_{mp} is the p^{th} zero of $J_m'(x) = 0$. The brackets contain the θ dependence for the two normal modes. The geometric factor can be written as:

$$G(R_e) = \tfrac{1}{4}\left[J^2_{m-1}(k_\perp R_e) + J^2_{m+1}(k_\perp R_e)\right]$$

Standing Wave (3.20)

A standing wave structure is obtained if the cylindrical (i.e., θ) symmetry is destroyed. This can be done, for example, by cutting slots in the wall. However, for a cavity with cylindrical symmetry, the RF field structure is found to rotate in the θ direction. This has been observed in experiments [32]. For this situation, the proper description of the cross-sectional structure of the $\bar{E}$ field is:

$$\bar{T}(r,\theta) = \left[\hat{\theta}\,\frac{1}{k_\perp}\,\frac{dJ_m(k_\perp r)}{dr} \mp \hat{r}i\left(\frac{m}{k_\perp r}\right) J_m(k_\perp r)\right] \exp(\pm im\theta) \tag{3.21}$$

Note that $\bar{T}$ is complex and thus $\bar{T} \times \bar{T}^*$ is nonzero. The derivation of the linear theory for this case shows that Eqs. (3.14)-(3.18) correctly give the linear characteristics of an ECM if the following expressions for $G(R_e)$ and $|p_o|^2$ are used:

$$G(R_e) = J^2_{m \pm 1}(k_\perp R_e)$$
$$|p_o|^2 = 2|p_o|^2_{\text{standing}}$$

Rotating Wave (3.22)

Note that the two rotating modes, designated by ±, interact differently with the beam and have different $G(R_e)$ when $m \neq 0$, while $G(R_e)$ is the same for both normal modes of a standing wave structure. In this section Eq. (3.20) will be used to define $G(R_e)$.

The sinusoidal distribution is characterized by several self-excitation regions which are dependant on q. Modes with q = 1 have the lowest starting currents, with the resonance band-width centered at approximately $x \simeq -1$. This observation is in agreement with the fact that the ECM interaction is a Doppler-shifted resonance that satisfies $\omega - k_{||} u \simeq \omega_c$. Modes with $q > 1$ generally have higher starting currents because I_{ST} scales as q/Q, and Q^{-1} increases with q. One can determine the minimum value of sw^2/c^2 needed in order for emission to occur from the condition $(sw^2/c^2) > 2F_c \cdot (dF_c/dx)^{-1}$. For a sinusoidal distribution this inequality becomes:

$$\left(\frac{sw^2}{c^2}\right) > \left[\frac{2x}{(1-x^2)} + \frac{\pi}{2} q \cot\left(\frac{(x+1)\pi q}{2}\right)\right]^{-1} \qquad (3.23)$$

For an ECM with a q = 1 mode operating at the minimum I_{ST} at $x \simeq -1$, sw^2/c^2 must be greater than approximately two in order for the ECM to self-oscillate. Excitation can be achieved at lower values of sw^2/c^2 by decreasing x, but this results in higher values of I_{ST}. This implies that, for a given beam current, the transverse energy of the electron beam must exceed a certain minimum value in order for emission to occur.

The use of a Gaussian, rather than a sinusoidal, function for g(z) can substantially alter the linear characteristics of an ECM. This can be seen in Fig. 3.1, where I_{ST} and the frequency detuning have been plotted for these two profiles for the TE_{031} mode with L = 10.5λ, and $\omega_{031}/2\pi$ = 200 GHz. The cavity has a Q_T = 3150 and, for copper walls, $Q_o >> Q_D$ so that the term $S/2Q_o$ is neglected in the detuning equation. The beam, which is assumed to have no velocity spread, interacts with the RF field at the 2nd radial maximum and has a voltage of 30kV and w/u = 1.5. Calculations are based on Eq. (3.16). The upper curves represent the values for I_{ST}, while the lower curves give the frequency detuning. The detuning $(\omega_\ell - \omega(\ell))$ is expressed relative to the resonance width ω_c/Q_T. For the Gaussian curves, L_{eff} = L has been assumed, which is typical for an open resonator of length L with straight cylindrical walls [31]. One can see that the Gaussian resonance region is substantially narrower than that for the sine distribution, and less shifted from zero. In addition, the minimum I_{ST} for the Gaussian, which occurs at:

$$x \doteq -\left(\frac{c^2}{w^2 S}\right) - \sqrt{1 + \left(\frac{c^2}{w^2 S}\right)^2} \qquad (3.24)$$

or $(\omega_c - \omega_{031})\, L/\pi u \cong -0.7$ for the parameters given above, is lower by a factor of 3 than the minimum I_{ST} for a sinusiodal g(z). The degree of detuning experienced in these two cases is similar. The narrower (and less shifted) I_{ST} curve for the Gaussian can be explained primarily in terms of differences in $k_{||}$, that is, differences in the breadth of the g(z) profile. For the above example, $k_{||} = 2/L = 1.21$ cm.$^{-1}$ for the Gaussian and $k_{||} = \pi/L = 1.99$ cm.$^{-1}$

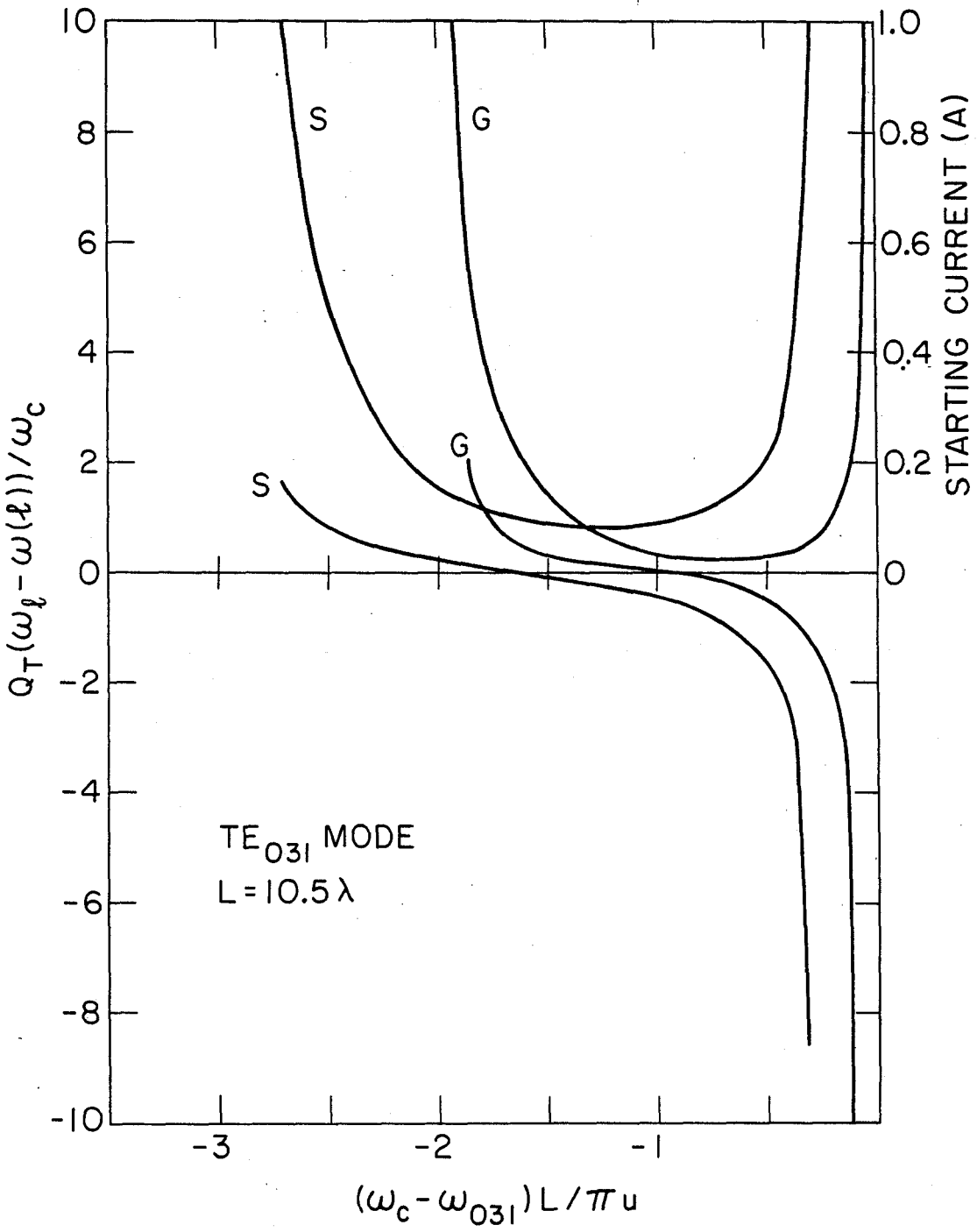

Figure 3.1 Comparison of the linear characteristics of an ECM with a sinusoidal (S) longitudinal RF field distribution with one having a Gaussian (G) profile. Upper curves represent the starting currents, while lower curves give the frequency detuning.

for the sine. Since the wavenumber for the Gaussian is smaller, which results in a broader profile, one would expect the Doppler shift and resonance width, both of which are inversely related to the breadth of g(z), to be reduced. The lower minimum starting current for the Gaussian is also primarily a result of the lower $k_{||}$.

The general expressions derived in Section 1 have been compared with the results of previous studies of ECM linear theory. Chu [28] has derived the starting current for TE_{opq} modes (i.e., m = 0) with a sinusoidal longitudinal field profile and no velocity spread in the beam using a fully relativistic approach. It was found that my weakly relativistic approach agrees with his results to within 10% for a beam energy of 60 keV or less. Thus, use of a fully relativistic model introduces rather small corrections in comparison to changes resulting from varying the RF field shape or allowing for a velocity spread in the electron beam. The results of this chapter should be sufficiently accurate as long as the beam voltage is low and the device operates at the fundamental. Antakov et. al. [26] have derived the starting current for a TE_{mpq} mode with $g(z) = \sin k_{||} z$ and a velocity spread in the beam. Their results were found to be in agreement with mine except for an additional factor of $(\beta_{||}/\beta_{\perp})^4$ in their equation, a factor that appears to be erroneous. Finally, the expression for I_{ST} for the Gaussian profile and no beam velocity spread was found to agree with similar results given by Nusinovich and Erm [39], as well as with an expression presented by Gaponov et. al. [32] for the minimum starting current.

The effect on I_{ST} of having a velocity spread in the electron beam will now be investigated. In order to avoid a detailed analysis

of particle trajectories from the gun cathode, it will be assumed that all electrons are emitted with the same energy, and that the perpendicular velocity dispersion can be described by a Maxwellian with a characteristic width Δw (full width at half maximum). For simplicity no spatial dispersion will be included. If we define $\bar{u}$ and $\bar{w}$ as the average velocities, then the electron distribution function is written as:

$$f_0(u,w) = \left(\frac{0.94}{\Delta w}\right) \exp\left(-\frac{(w-\bar{w})^2}{0.36(\Delta w)^2}\right) \delta(\bar{u}^2 + \bar{w}^2 - u^2 - w^2)(2\pi w)^{-1} \tag{3.25}$$

This expression for f_o is then used in conjunction with Eq.(3.14) to calculate the starting current.

This calculation was done numerically for the TE_{031} mode with a sinusoidal longitudinal field distribution using the same design parameters as those given for Fig. 3.1. The results are shown in Fig. 3.2, where I_{ST} has been plotted versus $\bar{x} = (\omega_c - \omega(\ell))/k_{||}\bar{u}$ for various velocity spreads $\Delta w/w$. It can be seen that large spreads in velocity have a relatively minor effect on the minimum starting current. Increasing the velocity dispersion causes the minimum value of I_{ST} to decrease and shift towards $\bar{x} = 0$ provided the dispersion does not become excessively large. This behavior can be explained in the following manner. Let x_{opt} be that value of x at which the electrons lose the greatest fraction of their energy and I_{ST} is minimized. If an ECM with a beam velocity spread is operating at $|\bar{x}|$ slightly less than $|x_{opt}|$, then a number of electrons will have a sufficiently small velocity u such that they have an effective $x \simeq x_{opt}$. In addition,

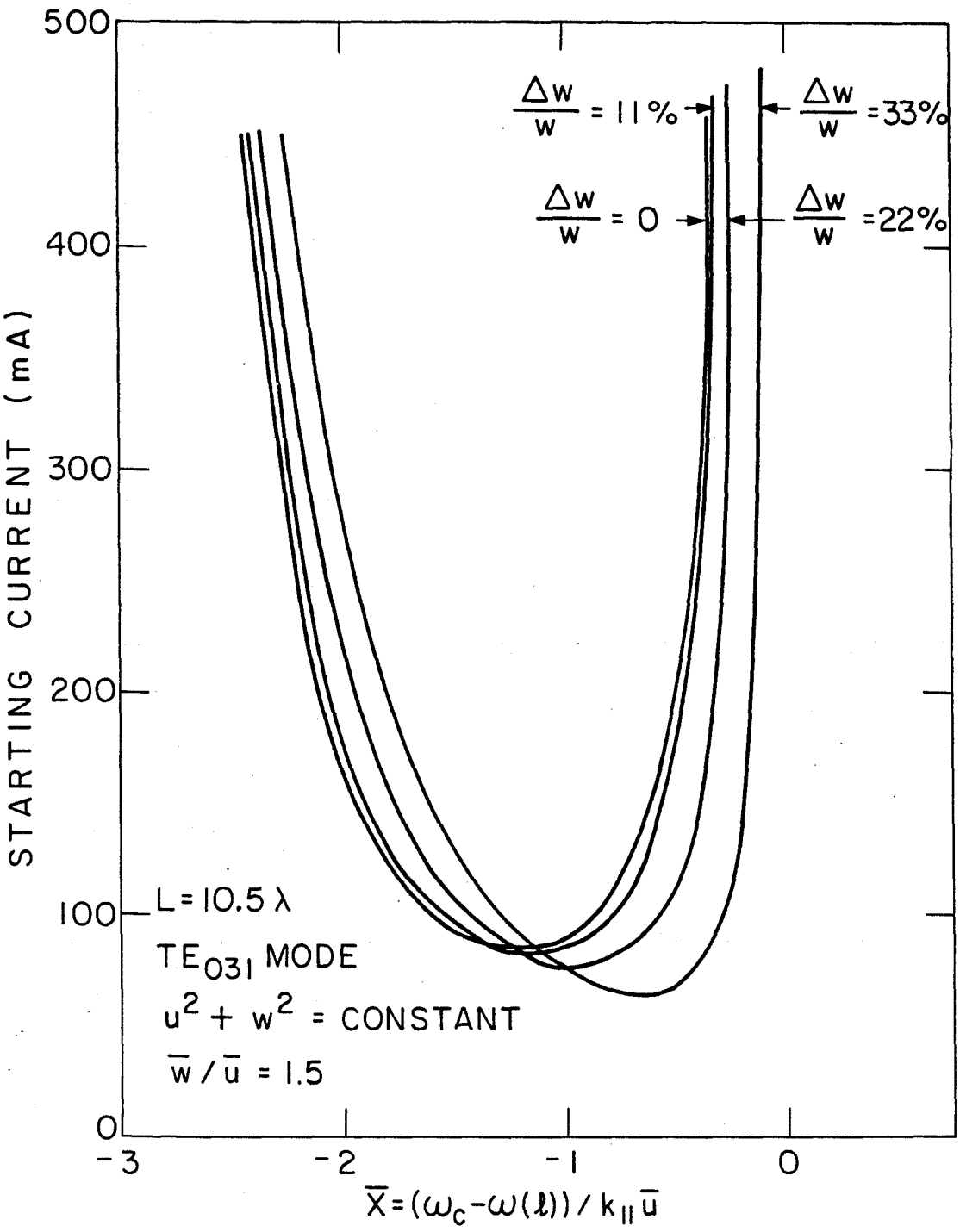

Figure 3.2 Dependence of the starting current on the velocity spread of the electron beam, $\Delta w/w$, for the TE_{031} mode. ECM has RF field with sinusoidal longitudinal profile, and same operating parameters as those given for Fig. 3.1

these particles will have a relatively high ratio w/u. These two factors cause these electrons to lose a larger than average fraction of their energy. It can be shown that this effect dominates, resulting in a reduction of the starting current for $|\bar{x}|$ slightly less than $|x_{opt}|$ for a beam with a velocity spread.

Although a velocity dispersion has a small and even somewhat beneficial effect in the linear regime of operation, this is not expected to be the case in the nonlinear operation of an ECM. For example, V. P. Taranenko et al. [35] conclude that a velocity spread in the electron beam has a detrimental effect on the efficiency of the device.

3.3 Field Profiling

Recent investigations [42,43] have shown that field profiling can be used to increase the efficiency of a gyrotron oscillator. Both the RF field and the axial magnetic field B_o can be shaped to achieve this improvement. In this section, the effect of profiling on the linear characteristics of the gyrotron will be explored.

The starting current can be calculated for any longitudinal profile of the RF electric field using Eq.(3.16a). Looking only at those terms that are affected by the field shape, one can write

$$I_{ST} \propto k_{\|}^2 \left(\int_{-\infty}^{\infty} d\tilde{z}\, g^2(\tilde{z})\right)\left(\frac{dF_c}{dx}\right)^{-1} \tag{3.26}$$

where it has been assumed that the derivative dominates within the brackets of Eq.(3.16a). This equation indicates that both the profile width and shape influence I_{ST}. For example, the major reason that the Gaussian gives a lower I_{ST} in Figure 3.1 is the fact that, for an open

resonator, the field can extend beyond the cavity, resulting in a broader profile. In order to eliminate the effect of the profile width and thus isolate the influence of the field shape, $k_{||}$ must be adjusted so that the profile halfwidth remains constant. This was done for the three profiles of Table 3.1, giving $k_{||}$ (sin) = 1.26$k_{||}$ (Gaussian) = 0.66 $k_{||}$ (flat). Using this in conjunction with Eq.(3.26), one can show that the Gaussian shape gives the lowest minimum starting current, while the flat shape gives the highest. The starting current of the Gaussian is 33% lower than that of the sinusoidal profile. These findings are consistent with those of Bykov and Goldenberg [43] who found that a region of low amplitude RF field at the input end of the cavity, such as the tail of a Gaussian, can help to prebunch the electrons, resulting in an improvement in the operational characteristics of the gyrotron.

The benefits of a low field, prebunching region at the front end of the cavity suggests that an asymmetric profile may result in lower starting currents. This can be investigated by modeling the electric field in the following manner:

$$g(z) = \begin{cases} \exp[-(k_{||}z)^2] & \text{for } z \leq 0 \\ \exp[-(rk_{||}z)^2] & \text{for } z \geq 0 \end{cases}$$

where r = 1 corresponds to a symmetric Gaussian, and r > 1 gives a longer tail at the cavity input end. Using this profile the gain function F_c and stored energy $|p_o|^2$, and subsequently the starting current, can be calculated. This was done in Figure 3.3, where the normalized current has been plotted for three different cases for a

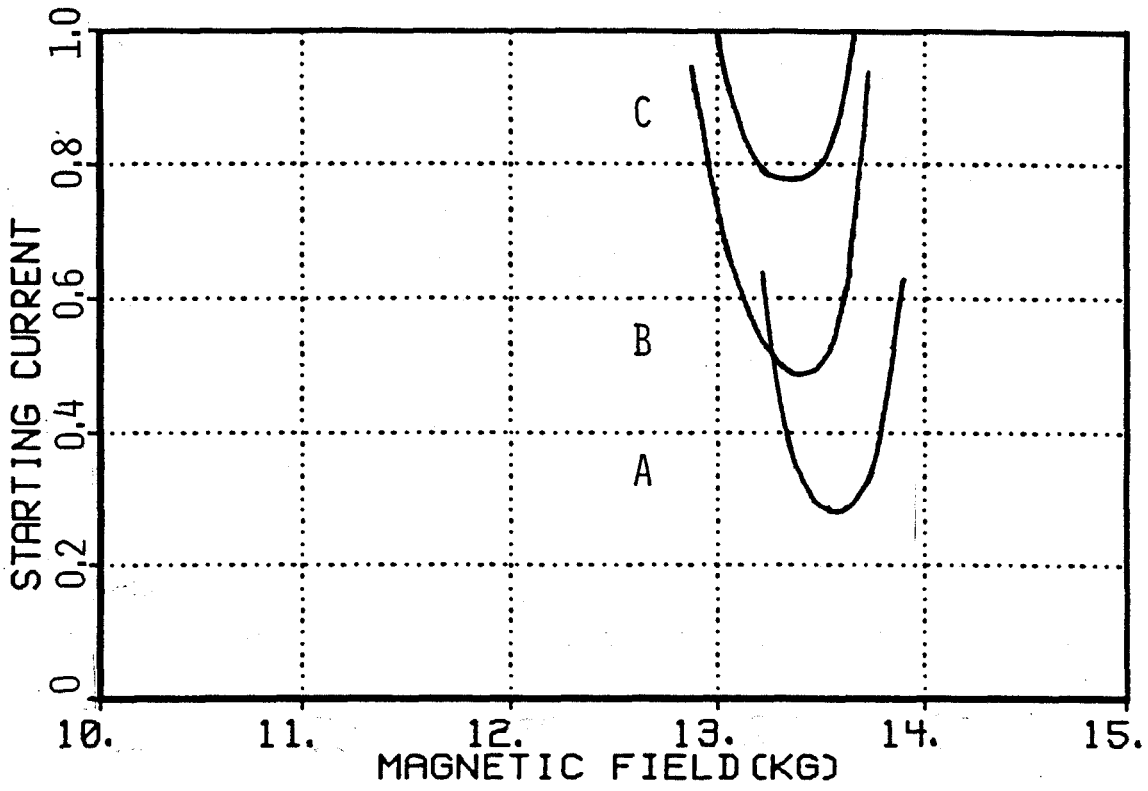

Figure 3.3: Effect of profile asymmetries on starting current of 35 GHz gyromonotron

A - symmetric Gaussian with wavenumber $k_{||}^{o}$

B - asymmetric Gaussian (r=2) with wavenumber $k_{||}^{o}$

C - symmetric Gaussian with same effective halfwidth as profile B ($k_{||} = 1.38\ k_{||}^{o}$)

35 GHz gyromonotron [44]. The first curve (A) is the gain curve for a symmetric Gaussian with wavenumber $k^o_{||}$. The second curve (B) shows the effect of using an asymmetric profile with the same wavenumber. The greater Doppler shift and higher starting currents are due to the fact that the asymmetric Gaussian has a narrower halfwidth. In order to eliminate variations due to the profile width, it is necessary to compare curve B with the gain curve of a symmetric Gaussian with the same effective halfwidth, which in this case is curve C with $k_{||} = 1.38\ k^o_{||}$. These plots indicate that profile asymmetries can drastically lower I_{ST}. In this particular example a reduction of 40% was obtained comparing curves B and C.

Magnetic field shaping has proven to be an important technique that has led to major improvements in gyrotron efficiency. As with $\bar{E}$ field profiling, this improvement results from a prebunching of electrons in velocity space in order to achieve maximum energy extraction.

The methodology outlined in Appendix B can be modified in order to include B_o profiling as well as RF field profiling. Looking at Eqs.(B.7), one can see that for small variations of B_o only the parameter $\phi'(\tau)$ will be affected. In actuality, u and w also change somewhat according to adiabatic theory, but these changes are minor and can be neglected. If a linear taper of B_o is assumed with slope $\partial B_o/\partial Z$, then $B_o = B_o(Z=0) + Z(\partial B_o/\partial Z)$. Using this in the equation for ϕ' leads to

$$\phi'(\tau) = \frac{u}{2}\frac{\omega_{co}}{B_o}\frac{\partial B_o}{\partial z}(\tau-t)^2 + \omega_{co}\left(1 + \frac{z}{B_o}\frac{\partial \dot{B}o}{\partial z}\right)(\tau-t) + \phi \qquad (3.27)$$

where the cyclotron frequency ω_{co} and B_o are evaluated at $z = 0$. The remainder of the derivation of I_{ST} is unaltered and leads to Eq.(3.16a) with the following gain function:

$$F_c = \int_{-\infty}^{\infty} d\tilde{z}\; g(\tilde{z}) \int_0^{\infty} d\lambda\; g(\tilde{z}-\lambda)\; \cos\left[\lambda x + \left(\frac{\omega_c}{k_{||}^2 u}\right)\lambda \frac{1}{B_0}\frac{\partial B_0}{\partial z}\left(\tilde{z} - \frac{1}{2}\lambda\right)\right] \tag{3.28}$$

Unfortunately, the Fourier techniques described in Appendix B cannot be used here, leaving a rather complicated integral to evaluate for all except the simplest profiles. It should be noted that the $\partial B_o/\partial z$ term introduced by the magnetic taper is a large factor that can drastically alter the gain function F_c.

3.4 Extension of Linear Theory to Higher Harmonics

The linear theory outlined in the first section can be modified to include the higher harmonic interactions. Operation at higher harmonics increases the beam currents needed for self-oscillation but lowers the magnetic field requirements and its associated costs. As noted in Appendix B, the fundamental interaction can be analyzed by using the RF field at the gyrocenter. In order to obtain the higher harmonic terms, the field seen by the electron along its orbit must be used.

In this analysis a methodology outlined by Yulpatov and Petelin [34] will be followed. The function $\mathfrak{F}$ used in Eqs.(3.9) is written as an expansion in terms of the gyrocenter coordinates (R_e, θ_e) and the Larmor radius and phase of the electron with respect to the gyrocenter (r_L, ϕ). This differs from the approach used by Chu [28], who expanded the RF field components directly, and only treated m=0 modes. The expansion of $\mathfrak{F}$ can be written in the following general form:

$$\mathfrak{F}(r,\theta) = \sum_{n=-\infty}^{\infty} \mathfrak{F}_n (R_e, \theta_e, r_L) e^{-in\phi} \tag{3.29}$$

where the series represents the various harmonic terms. The coefficient $\mathfrak{F}_n$ can be written as

$$\mathfrak{F}_n(R_e, \theta_e, r_L) = (2\pi)^{-1} \int_{-\pi}^{\pi} \mathfrak{F}(r,\theta) e^{in\phi} d\phi \tag{3.30}$$

The immediate goal is to express $\mathfrak{F}_n$ in terms of two functions, one defined in terms of the gyrocenter coordinates, the other in terms of r_L. This can be achieved if the following integral representation of $\mathfrak{F}$ is used [45].

$$\mathfrak{F}(r,\theta) = \int_{-\pi}^{\pi} \eta(\xi) e^{ik_\perp r \cos(\xi-\theta)} \, d\xi \tag{3.31}$$

This integral is equivalent to expressing $\mathfrak{F}$ as a sum of plane waves with a weighting factor $\eta(\xi)$. Substituting this equation into Eq.(3.30) and expressing r and θ in terms of R_e, θ_e, r_L, and $\alpha \equiv \phi - \xi$ gives

$$\mathfrak{F}_n = (2\pi)^{-1} \int_{-\pi}^{\pi} \eta(\xi) e^{ik_\perp R_e \cos(\theta_e - \xi) + in\xi} \int_{-\pi-\xi}^{\pi-\xi} e^{ik_\perp r_L \cos\alpha + in\alpha} \, d\alpha \, d\xi \tag{3.32}$$

It can be shown that the second intergral can be written as $2\pi i^n J_n(k_\perp r_L)$. The first integral is obtained by using the following operator on $\mathfrak{F}(R_e, \theta_e)$ as defined by Eq.(3.31):

$$L_n = \left(\frac{n}{|n|}\right)^n \left[\exp\left(i\frac{n}{|n|}\theta_e\right) k_\perp^{-1} \left(\frac{\partial}{\partial R_e} + iR_e^{-1}\frac{n}{|n|}\frac{\partial}{\partial \theta_e}\right)\right]^{|n|} \tag{3.33}$$

Combining these results gives

$$\mathfrak{F}(r,\theta) = \sum_{n=-\infty}^{\infty} J_n(k_\perp r_L) \, L_n \left[\mathfrak{F}(R_e, \theta_e)\right] e^{-in\phi} \tag{3.34}$$

and from this $\bar{T}(r,\theta)$ can be determined. The remainder of the derivation of I_{ST} as described in Appendix B and Section 3.1 continues unaltered, yielding the following equation for the starting current for the n^{th} harmonic interaction and an annular beam:

$$I_{ST} = \frac{\varepsilon_0 \omega \ell}{2} \frac{}{Q_T} |p_0|^2 \frac{\gamma m_e}{e} \frac{k_\parallel^2 \bar{u}}{\pi G_D} \left(\frac{dJ_n(k_\perp r_L)}{dk_\perp r_L} \right)^{-2} \left[\int_{-\infty}^{\infty} du \int_0^{\infty} dw \, \frac{nsw^3}{uc^2} f_o \frac{dF_c}{dx} \right]^{-1}$$

$$G_D = \frac{1}{2\pi} \int_0^{\pi} d\theta \, |L_n[\bar{f}(R_e,\theta_e)]|^2 \qquad x = \frac{n\omega_c - \omega}{k_\parallel u} \qquad (3.35)$$

and only the cyclotron instability term has been retained, the other terms being negligible for $n > 1$. Comparing this equation with Eq.(3.14), one can observe that the changes resulting from the inclusion of the higher harmonic terms are the introduction of a Larmor radius factor, the replacement of ω_c with $n\omega_c$, and a new definition for G_D. For standing and traveling waves in the θ direction, the following functions are used to obtain G_D:

$$\text{Standing:} \quad \bar{f} = J_m(k_\perp R_e) \cos m\theta_e$$

$$|L_n|^2 = \frac{1}{4} J_m^2 + n(k_\perp R_e) + J_{m-n}^2(k_\perp R_e)$$

$$\text{Rotating:} \quad \bar{f} = J_m(k_\perp R_e) \, e^{\pm im\theta_e}$$

$$|L_n|^2 = J_{m\pm n}^2(k_\perp R_e) \qquad (3.36)$$

These results are in good agreement with Chu's theory for $m = 0$ modes, and also agree with Gaponov's expression [32] if the small argument expansion of $J_n(k_\perp r_L)$ is used.

This theory has been utilized to calculate the mode spectrum of a proposed 245 GHz second harmonic experiment [46], and the results are shown in Fig. 3.4. This device would operate in the TE_{051} mode and have a cavity length of 15 wavelengths, a beam voltage of 65kV, and a velocity ratio $w/u = 1.27$ at $B_o = 49$ kG. The second graph indicates that the spectrum of competing first harmonic modes is relatively thin and that thse modes should not pose any difficulties. The first graph shows that the neighboring second harmonic oscillations are the spurious modes most likely to be excited, especially the TE_{1021} mode whose gain region virtually coincides with that of the TE_{051} mode.

3.5 Theory of Mode Excitation

Two topics will be dealt with in this section. The first will be a description of the spectrum of modes excited in a gyrotron. The simple approximation that these modes are excited at Doppler-shifted frequencies (i.e., $\omega = \omega_c \pm k_{||} u$) can be shown to be inadequate for low q modes, and a more realistic formalism based on the exact linear theory will be developed. The second topic will be a discussion of multimode excitation in a gyrotron resonator.

In order to obtain a mode spectrum, the threshold current must be calculated as a function of magnetic field, or equivalently ω_c, for the desired mode and neighboring modes. For a gyrotron, it is convenient to first determine the starting current and frequency of each $q > 1$ mode relative to the $q = 1$ mode. Then the various TE_{mp1} modes can be related to one another based on their transverse indices ν_{mp}. To use this methodology, one must identify the dependence of I_{ST} on the parameters q and x, the latter determining the magnetic field dependence.

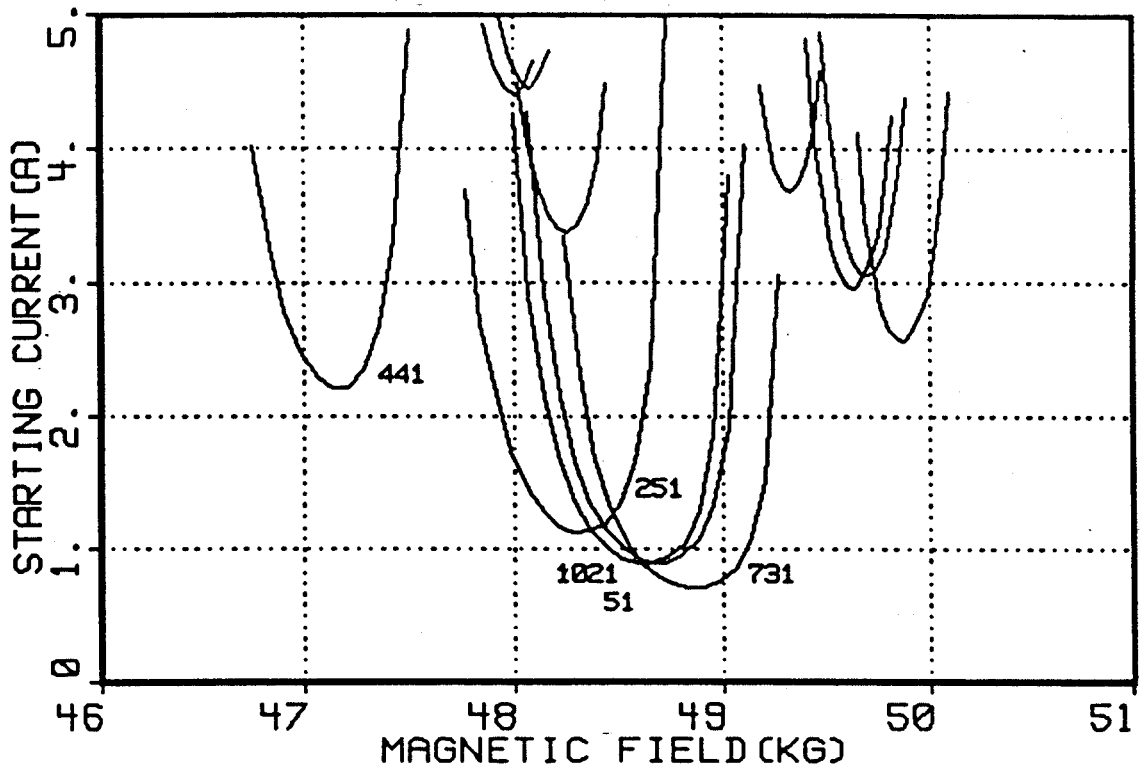

Figure 3.4(a): Second harmonic mode spectrum for a TE_{051} 245 GHz experiment.

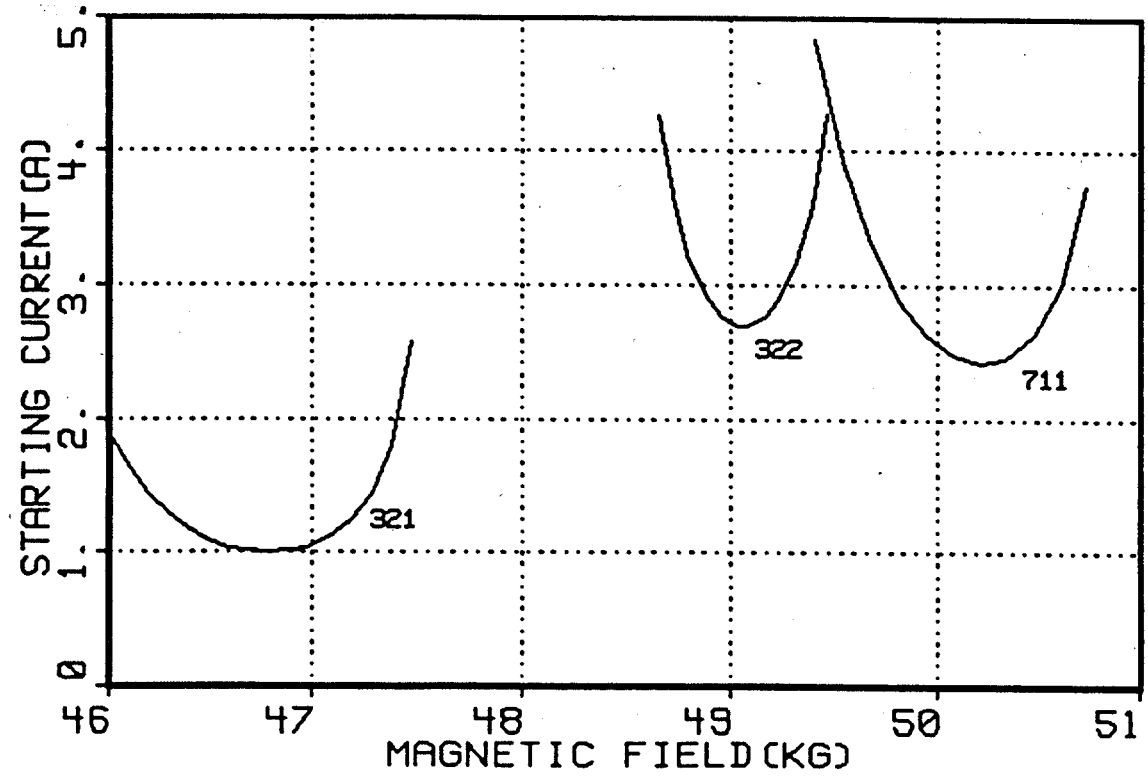

Figure 3.4(b): Competing first harmonic modes for the above 245 GHz experiment.

If Q_T is approximated as the diffractive Q as given by Vlasov [31]:

$$Q_T \simeq Q_D \propto \frac{4\pi L^2}{q^2\lambda^2}$$

then the following scaling relation can be obtained from Eq.(3.16a):

$$I_{ST} \propto \left(\frac{u^3}{w^2}\right) q^5 \left(\frac{dF_c(x,q)}{dx}\right)^{-1} \qquad (3.37)$$

where only the cyclotron instability term has been retained since it dominates. Using this equation, the relative positions of the $q > 1$ modes can be determined. A typical example of the hierarchy of modes that exists in a gyrotron resonator is shown in Fig.3.5. Each TE_{mpq} mode is characterized by q strong excitation branches, of which two predominate for $q \geq 2$. If $q = 1$, only a single branch at the Doppler down-shifted frequency (i.e., $x = -1$) is strong. Because of the dependence of the cavity resonance frequency on q, these branches are shifted to higher magnetic field as q increases. This results in a significant overlap of modes on the lower magnetic field side of TE_{mp1}, and a spreading out of modes on the higher side. Another observation that can be made from Fig.3.5 is that modes in the higher magnetic field region have relatively lower starting currents. This is a result of adiabatic compression, which causes the ratio u/w to decrease as B_o increases, thus reducing I_{ST}. Finally, an analysis of Eq.(3.37) indicates that if Q did not depend on q, then the minimum starting currents of gyrotron modes would be roughly independent of q.

Figures 3.6 are examples of mode spectra of gyrotrons. For both graphs the device parameters are: beam voltage = 65 kV, cavity length = 15 mm, frequency = 140 GHz, $Q_T = 8\pi \cdot (L/\lambda q)^2$, and w/u = 1.5 at

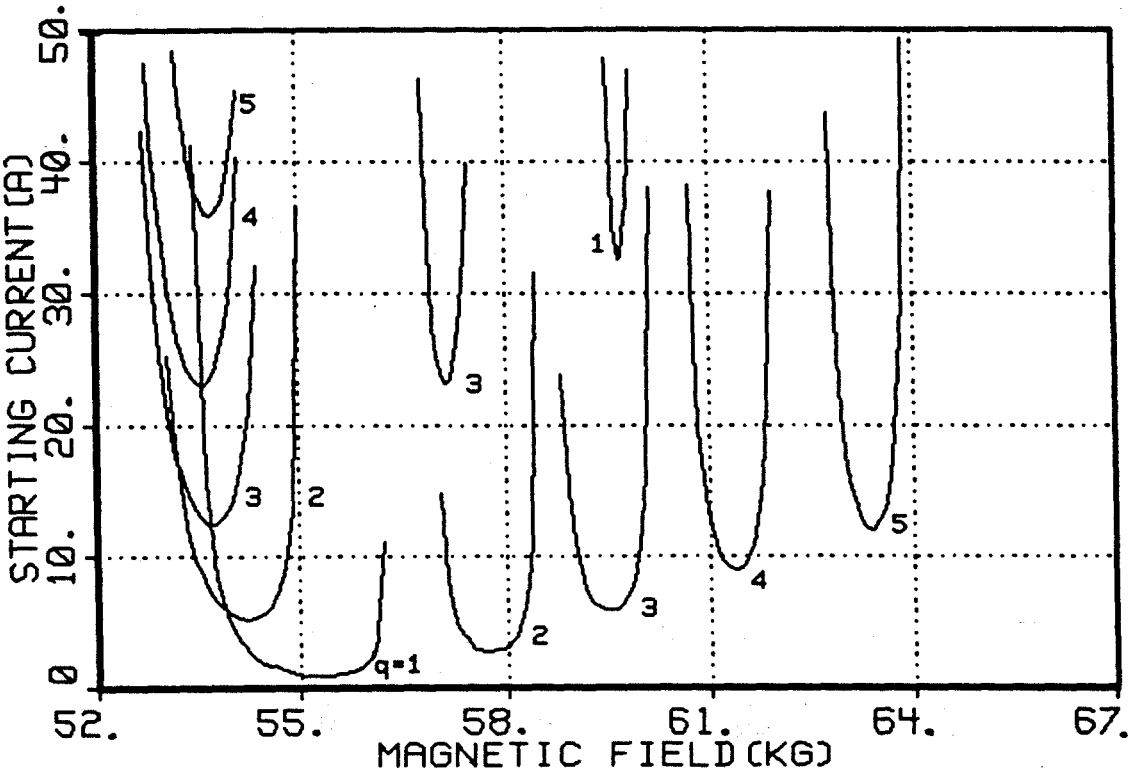

Figure 3.5 Example of hierarchy of modes excited in a gyrotron resonator (m and p fixed, $q \leq 5$)

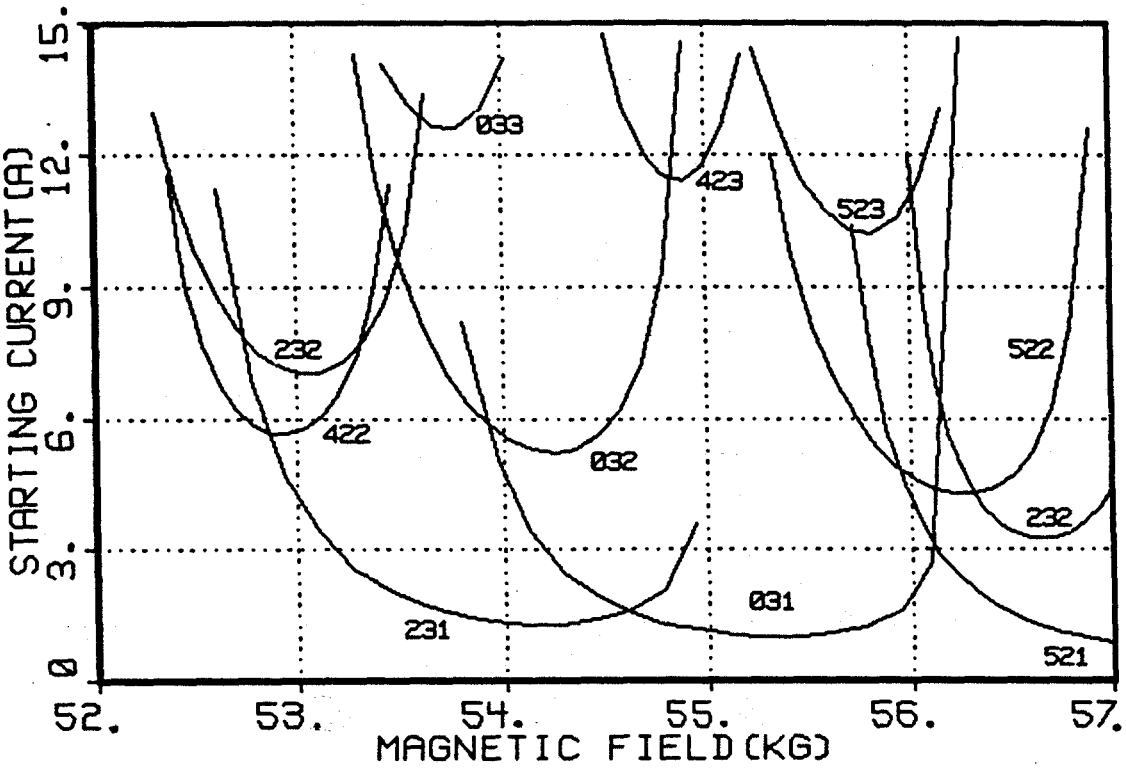

Figure 3.6(a) Mode spectrum of 140 GHz gyrotron operating in TE_{031} mode. See text for device parameters.

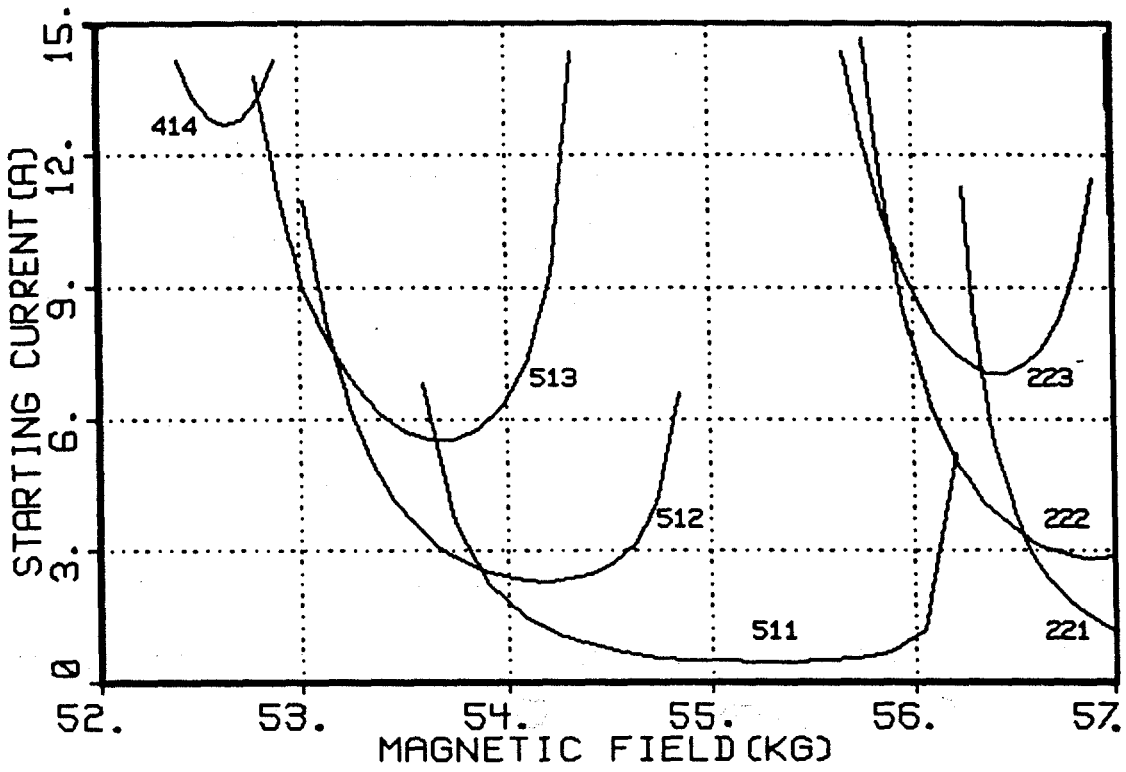

Figure 3.6(b) Mode spectrum of 140 GHz gyrotron operating in "whispering gallery" mode TE_{511}.

B_o = 55.7 kG. The only parameter that is different in each graph is the cavity radius, which is adjusted so that the oscillation frequency remains fixed at 140 GHz for the desired modes TE_{031} and TE_{511}. Fig. 3.6(a) clearly demonstrates the severe mode competition that will be encountered when operating in higher order modes. Careful inspection reveals the hierarchy of modes seen in Fig.3.5. Stable, single mode operation may be difficult due to the significant overlap of the modes TE_{231} and TE_{032}. Fig.3.6(b) suggests that operation in a whispering gallery mode, characterized by large m and p = 1, might help to alleviate this problem. The only modes severly overlapping with TE_{511} are its higher q modes. The primary reason for the absence of competing modes here is that the RF fields of whispering gallery modes are localized near the cavity walls, and an electron beam interacting with this mode will not couple effectively with other modes whose RF field maxima are closer to the resonator axis. However, ohmic losses in the cavity walls may cause difficulties in using this class of modes.

We next consider multimode excitation, which is one of the major problems confronting the high power, high frequency gyrotron. This involves the excitation of a number of competing modes in addition to the working mode, thus adversely affecting the efficiency of the maser. This problem is exasperated as the cavity size is increased to accommodate higher powers, since one must move to higher order modes, and mode separation decreases. In order to analyze multimode excitation, the oscillation equations (3.6) for all possible excited modes must be solved simultaneously. In general, a mode can be excited if its frequency falls within the gain bandwidth $\Delta\omega_g \sim k_{\|} u$. These equations

are coupled since the perturbed current $\bar{J}$ is a function of all the modes oscillating within the cavity. Coupling between modes also occurs as a result of the ohmic losses in the cavity walls (i.e., the $Q_o^{\ell d}$ terms, where $\ell \neq d$), but these terms are typically small and can be neglected. The crossterms associated with the $\bar{J} \cdot \bar{E}$ integral result from the fact that the RF field serves two purposes. It is responsible for the bunching of the electrons as well as the energy extraction from the electron stream. In the case of a single mode, both duties are accomplished by the same field. In the case of multimode operation, crossterms occur because bunching and energy extraction can be accomplished by different modes, and this leads to geometric factors which are functions of $\bar{T}_\ell$ and $\bar{T}_d$, where ℓ and d represent different modes.

A number of complications arise when two or more modes are allowed to oscillate within a cavity. For a single-mode analysis, the final equations for the starting current and detuning are independent of both time and RF field amplitude, which is consistent with linear theory. However, in a multimode analysis, the cross-terms associated with the interaction of two separate modes will be functions of both time and the relative amplitudes of the two modes. These terms will be proportional to $\exp(i\Delta\omega_s t)$, where $\Delta\omega_s = \omega(\ell) - \omega(d)$. The correct treatment of these terms will thus depend upon the relative frequencies of the competing modes. If $(\Delta\omega_s)^{-1}$ is small compared to the transit time of the electron in the cavity ($\tau_i \sim (k_{||} u)^{-1}$), then $\exp(i\Delta\omega_s t)$ is expected to be highly oscillatory along the electron path, mode coupling will be weak, and the cross-terms can be ignored. In this case each oscillation equation can be solved independently in the linear regime. However, if $\Delta\omega_s \simeq k_{||} u$, then the cross-terms cannot

be neglected, and the system of oscillation equations must be solved simultaneously. A multimode anaysis would utilize Eqs.(3.7a) and (3.7b), and Eq.(3.11) in its generalized form. Such an analysis has been done, and some of the major qualitative features of the solution will now be described.

Consider a cavity resonator with a circular cross section and a thin annular beam symmetric in θ. For this cavity, one can show that two cavity modes, TE_{mpq} and $TE_{m'p'q'}$ will turn on simultaneously only if $m = m'$ and $p = p'$. This can be explained as follows. For those competing modes with different m, the orthogonality of the θ dependence of the two modes will cause $G_D^{\ell d}$ and $G_c^{\ell d}$, $\ell \neq d$, in Eq. 3.11 to be zero. This will eliminate mode coupling in this case. For modes with $m = m'$ but $p \neq p$, it is easy to show that the frequency difference of the modes

$$\Delta\omega_s/\omega \simeq |\nu_{mp} - \nu_{mp'}|/\nu_{mp}$$

will always be quite large for gyrotron modes with m or p less than about 20. Thus, in practice, mode competition in the linear theory only occurs between modes of the form TE_{mpq} and $TE_{mpq'}$. These modes can be closely spaced, particularly if $q = 1$ and $q' = 2$ and the cavity is near cutoff ($k_\perp >> k_\parallel$).

Fig.3.7 shows results for the TE_{03q} and TE_{23q} modes with $q = 1$ and 2. The starting current and detuning ($\omega_\ell - \omega(\ell)$) are plotted versus $x_{031} = (\omega_c - \omega_{031})/k_\parallel^{031}u$, and have been calculated using the single mode equations. The parameter x_{031} is effectively a measure of the magnetic field. The device parameters are the same as those presented in conjunction with Fig. 3.1. Here one can see extensive

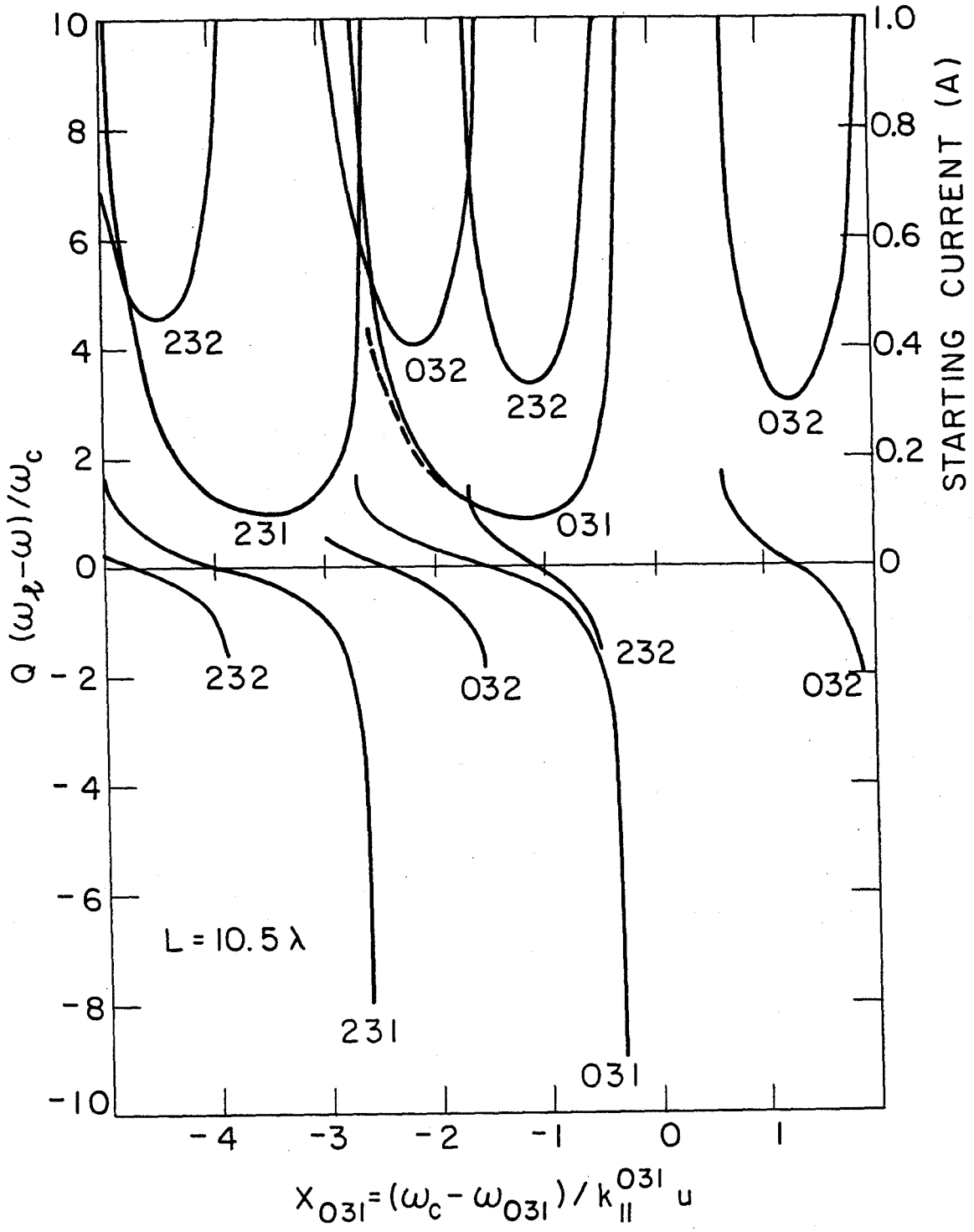

Figure 3.7 Starting current (upper curves) and detuning (lower curves) for the TE_{03q} and TE_{23q} modes. Dotted line is starting current if TE_{031} and TE_{032} oscillate simultaneously.

mode overlap of the 031 and 032 modes. In addition, the TE_{opq} and TE_{2pq} modes tend to be closely situated, especially for $p \geq 3$. The frequency detuning observed in Fig. 3.7 is quite small, although measurable, with $|Q_T(\omega_\ell - \omega(\ell))/\omega_c| \lesssim 2$ over a major portion of the I_{ST} curves. Also plotted is the starting current if both TE_{031} and TE_{032} exist in the cavity simultaneously. Here one observes that the gyrotron can self-oscillate at a lower beam current than the starting currents of the individual modes.

Based on the observation that the starting current curves have an approximate width $\Delta x \simeq 2/q$, one can derive a simple scaling law that determines if mode competition will be a major problem. Modes TE_{mpq} and $TE_{m'p'q'}$ will not overlap when $\omega_{mpq} - \omega_{m'p'q'} \geq (2 + q - q') \cdot (\pi/L)u$ if $\omega_c > \omega_c'$. Writing $\omega_{mpq} = c\nu_{mp}/R_o$ gives

$$\frac{1}{8}(q + q')\Delta q\left(\frac{\lambda}{L}\right)^2 + \frac{\Delta\nu_{mp}}{\nu_{mp}} \geq \frac{1}{2}(2 + \Delta q)\left(\frac{u}{c}\right)\left(\frac{\lambda}{L}\right) \tag{3.38}$$

as the mode separation condition, where $\Delta q = q - q'$ and $\Delta\nu_{mp} = \nu_{mp} - \nu_{m'p'}$. This is satisfied in the case of the competing TE_{031} and TE_{231} modes with $L/\lambda = 10.5$ and $\Delta\nu_{mp} = 0.2$, and thus only a slight overlap of these modes is observed in Fig. 3.7. However, Eq. (3.38) indicates competition between TE_{031} and TE_{032} ($\Delta q = 1$, $\Delta\nu_{mp} = 0$), and this is verified by the graph.

3.6 Startup of a Gyrotron

In this section the startup phase of a pulsed gyrotron will be investigated [47]. As a result of the time varying gun parameters, the

magnetic field and starting current needed for self-excitation drastically change during this period. Therefore it is important that the gun parameters be carefully controlled in order that the desired mode is excited first. Due to the brevity of the startup period (typically lasting a few microseconds or less), only the cathode and control anode voltages can be altered appreciably in practice. The magnetic field cannot be changed on such a fast time scale. The beam current, which is set by the thermal emission limit of the gun, reaches its full value at gun voltages which are well below their final operating levels. Therefore, the magnetic field and beam current can be treated as fixed parameters during the startup phase.

Ideally, the startup scenario chosen should result in the excitation of the desired mode first, and should maintain stable, single-mode operation thereafter. The analysis of mode stability requires a nonlinear treatment of the beam-field interaction and is beyond the scope of this analysis. However, a number of studies have been done [48,49], and these indicate that once a mode is excited, it tends to suppress the initiation of subsequent modes. Therefore, the excitation of the desired mode first will help to ensure that stability is achieved. It is also desirable that the working mode be chosen in a region relatively free of competing modes. A good example of this is the whispering gallery mode discussed earlier.

Various gyrotron startup scenarios have been analyzed by solving the linear theory exactly on a computer. This code can generate mode charts quickly for a variety of gun voltages. Two methods of turn-on were investigated in detail. In one sequence, both the cathode and control anode voltages were varied to their final

operating values in such a manner that their ratio remained constant. This can be accomplished in practice through the use of a resistance divider. This is shown for the case of the TE_{031} mode discussed earlier in Figures 3.8(a) through 3.8(d) where the final operating parameters are those associated with Figure 3.6(a). It should be noted that the cathode voltage U has been defined as the potential difference between ground and the cathode, and the anode voltage V_a is the difference between the control anode and the cathode. V_a and U are therefore treated as positive quantities, although in reality both voltages must be driven negative in order to generate an electron beam. Also, the value of V_a associated with Fig. 3.6(a) is 20kV, which results in an electric field of 5×10^6 V/m between the control anode and cathode.

In the second sequence, the cathode voltage U is held constant while V_a is ramped up from below cathode voltage to its final operating value. This might be accomplished through the use of two independently controlled voltage supplies, one CW and the other modulated. This scenario is shown in Figures 3.9(a) and 3.9(b), where again TE_{031} operation depicted in Fig. 3.6(a) has been chosen as the final operating point.

Examining these two sets of graphs, one can see how dramatically the excitation regions shift during the startup phase. This is particularly true for the V_a/U = constant sequence. Here one can see the TE_{521} curve minimum shift from 53.5 kG to 57 kG as U increases from 35 to 65 kV. In addition the minimum starting current decreases from about 9.3A to 1A, primarily due to the fact that w/u increases as the gun voltages are raised to their final values.

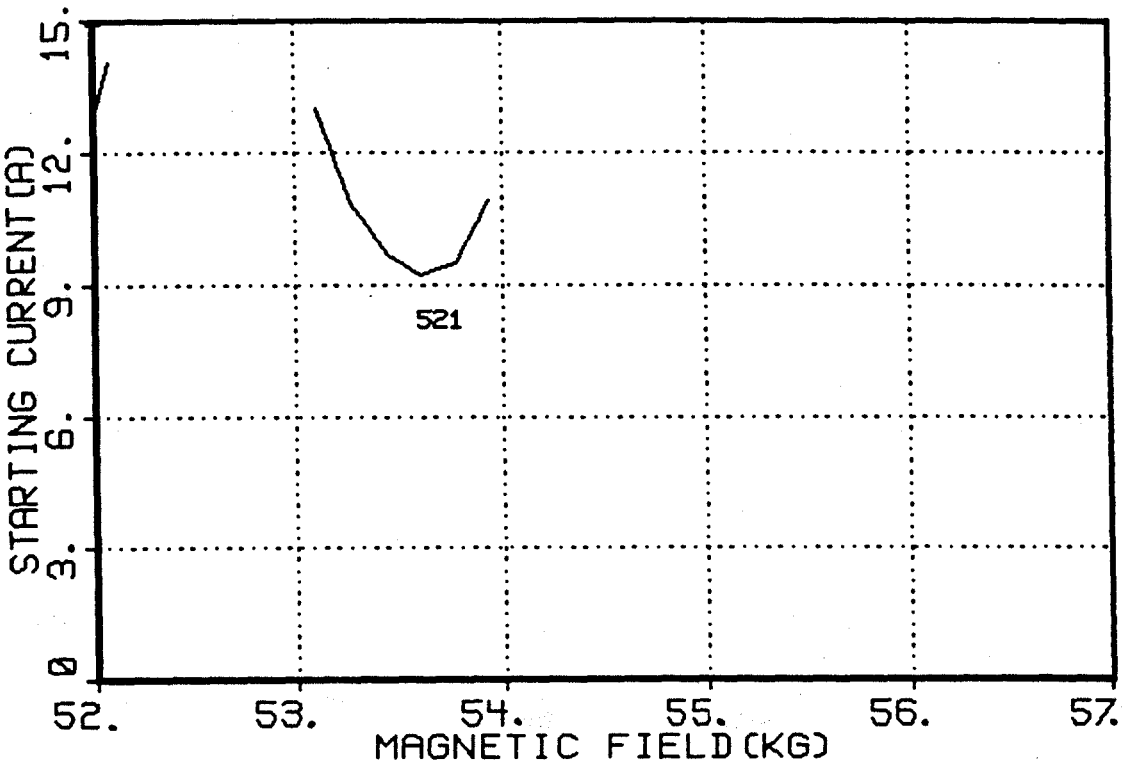

Figure 3.8(a) First of sequence of graphs showing startup for V_a/U = constant. Same final operating parameters as those associated with Fig. 3.6(a). Here U = 35 kV and V_a = 10.77 kV.

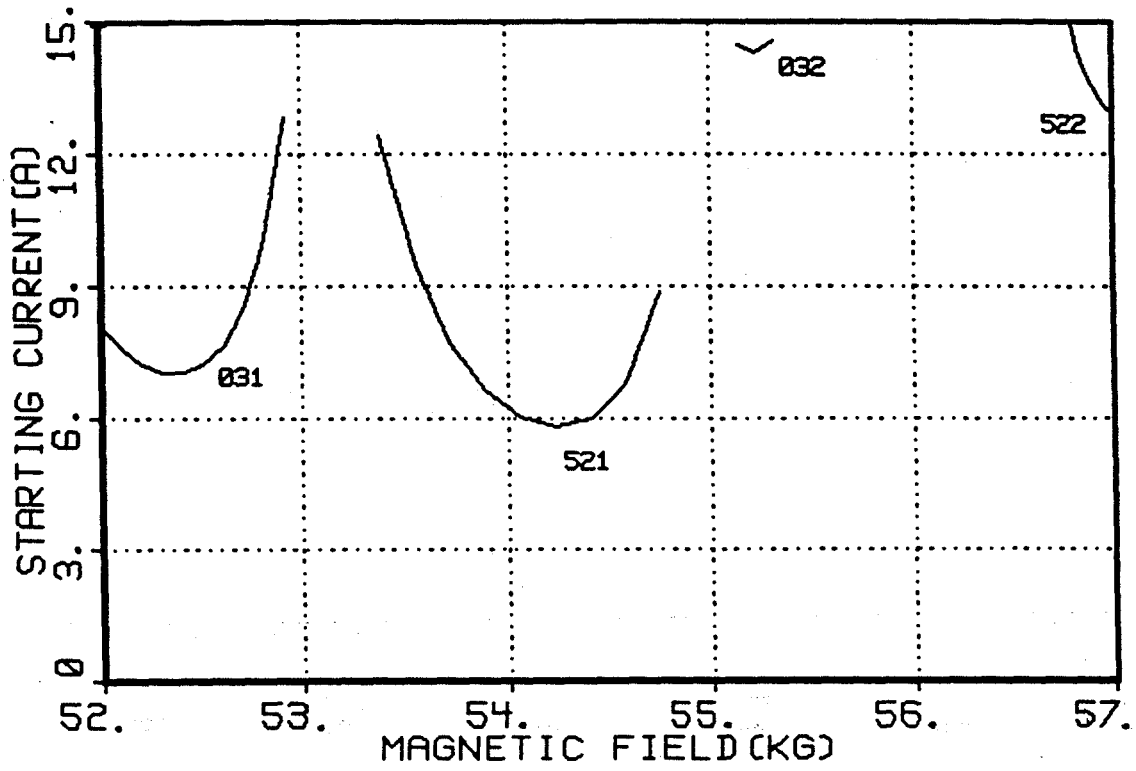

Figure 3.8(b) U = 40 kV and V_a = 12.31 kV.

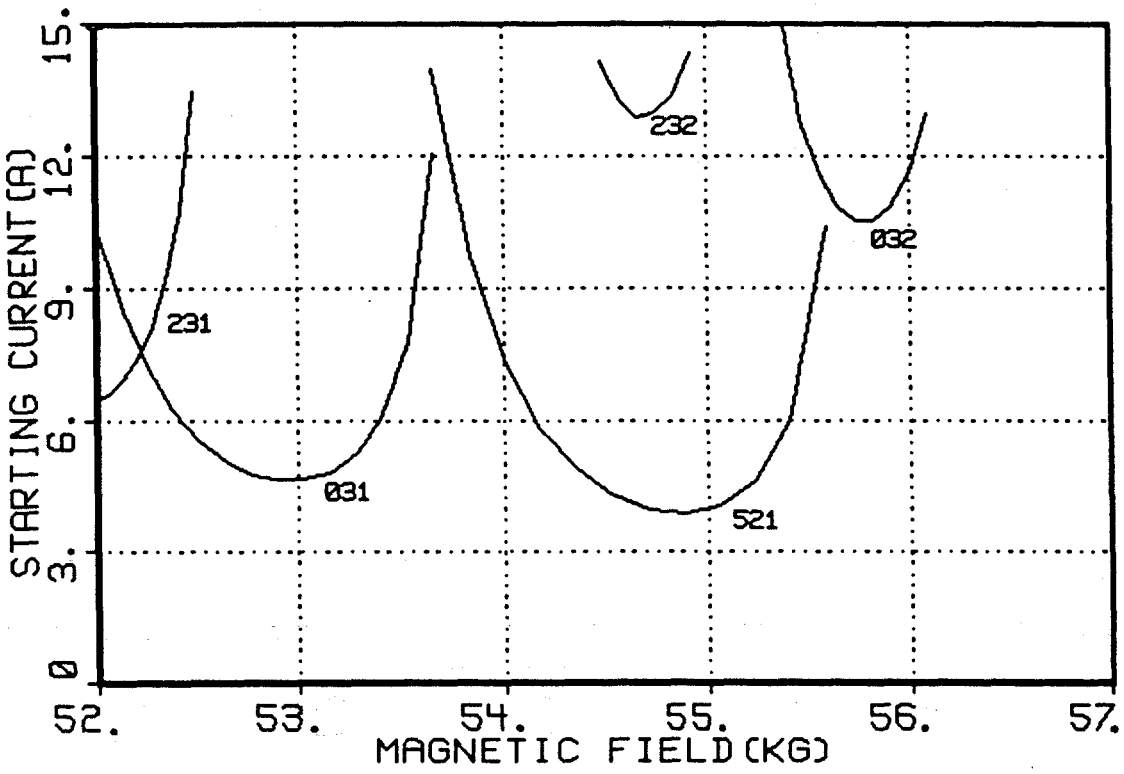

Figure 3.8(c) U = 45 kV, V_a = 13.85 kV.

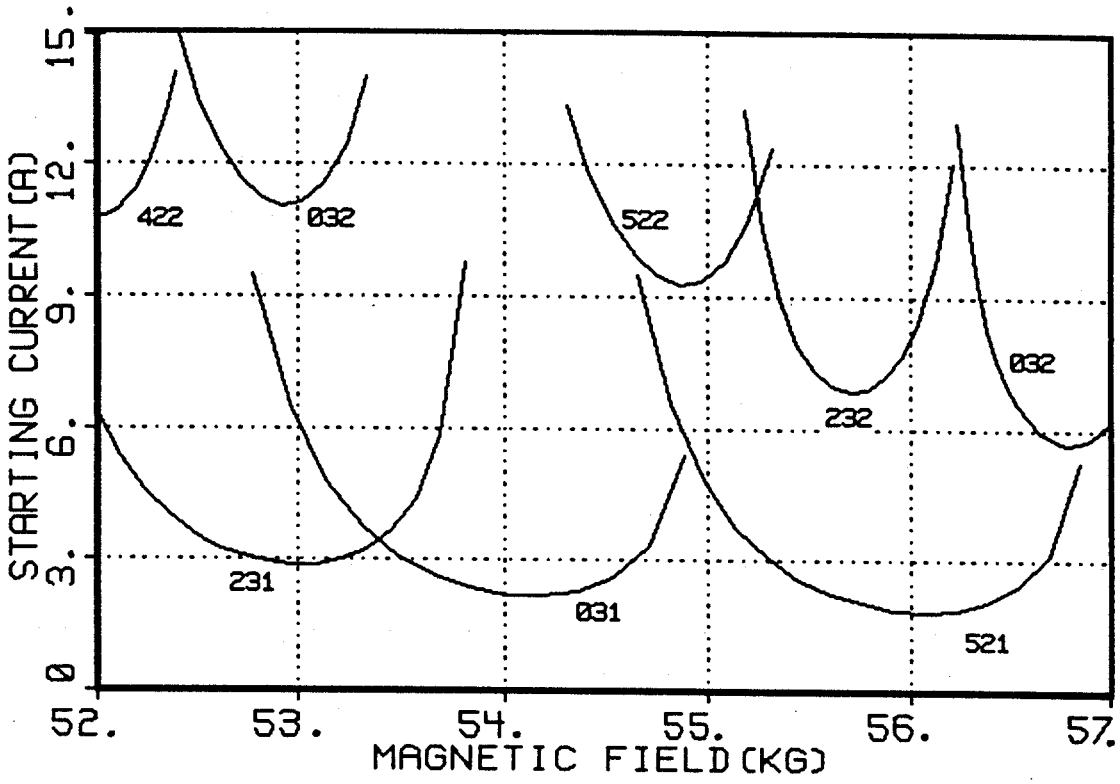

Figure 3.8(d) U = 55 kV, V_a = 16.92 kV.

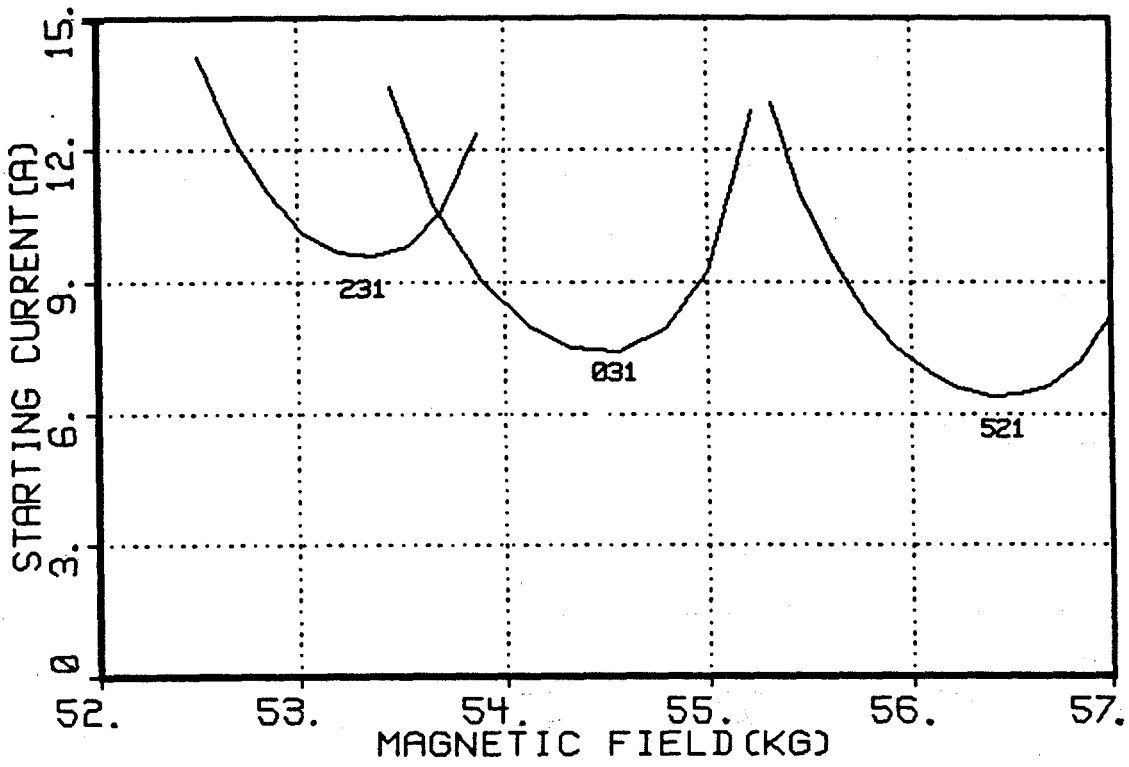

Figure 3.9(a) Startup sequence for U = constant. Here U = 65 kV and V_a = 15 kV.

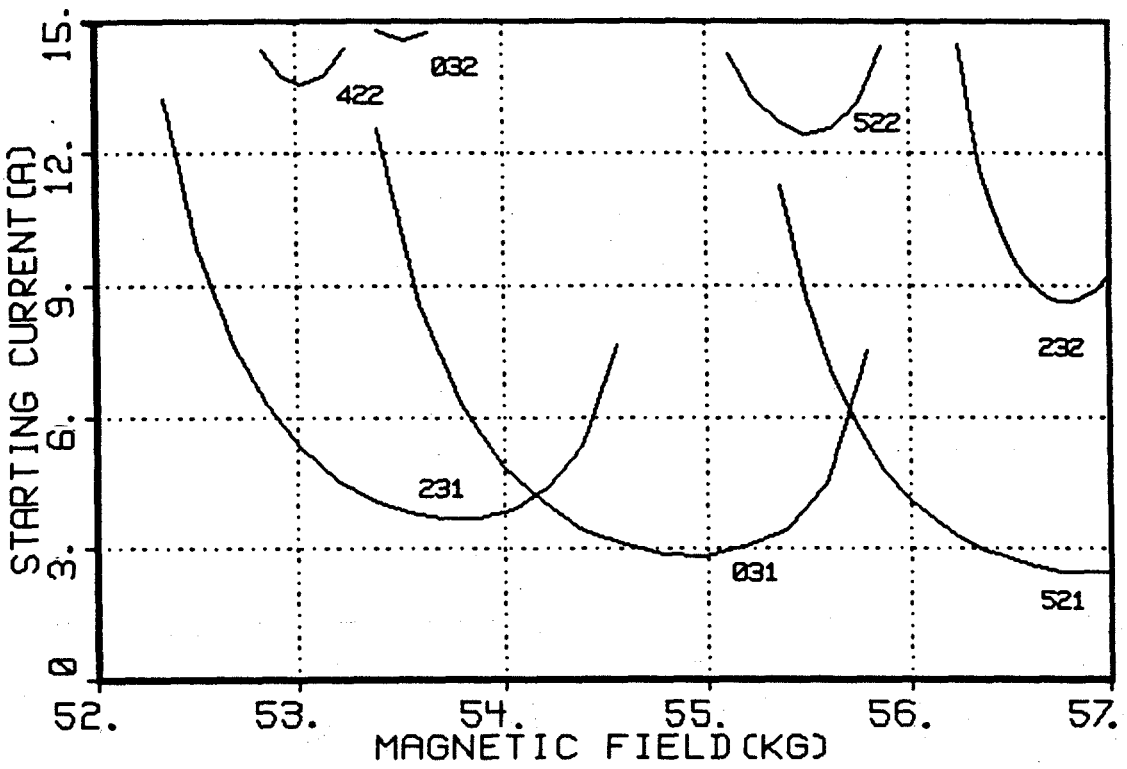

Figure 3.9(b) U = 65 kV and V_a = 17.5 kV.

In order to evaluate whether the desired mode will be excited first, the beam current and magnetic field must be chosen. A current of 6A was selected in order to achieve 100 kW output power, and a field of 54 kG was determined based on efficiency calculations of Chu et al. [42]. Looking at the V_a/U = constant sequence of figures, one can observe that there is a real danger of exciting the TE_{521} mode first at U = 40 kV, well before the TE_{031} mode is excited at about U = 50 kV. There are a number of possible ways of circumventing this problem. First, the diffractive Q for TE_{521} could be selectively lowered by modifying the resonator shape or output coupling, thus raising the starting current sufficiently to avoid oscillation. Here, one must avoid altering the Q_T of the TE_{031} mode as much as possible. A second approach would involve varying the radius of the electron beam in order to reduce coupling between the beam and RF field of the TE_{521} mode. As before, this would only be effective if strong beam coupling with the TE_{031} mode could be maintained. A final method is suggested by the second startup scenario. Rather than select a startup in which the excitation regions undergo large shifts in magnetic field, it would be desirable to choose a method in which the field associated with each curve remains relatively fixed, and only the minimum starting current is changing. As a result the neighboring parasitic modes would have less of an opportunity to be excited before the desired mode, as is illustrated in Figs. 3.9(a) and 3.9(b). For this case, as V_a goes from 15 to 20 kV, the magnetic field associated with TE_{031} only shifts from 54.5 kG to 55.3 kG. The TE_{031} mode is excited just before the TE_{231} mode at V_a = 17 kV. The primary reason for the smaller shifts associated with this startup is the fact that

the parameter x , which determines the magnetic field required to excite a mode with the minimum beam current, is less sensitive to V_a than it is to U.

Once the beam current and magnetic field are fixed, it is possible to depict all possible startup methods on a single graph. This is shown in Fig. 3.10, where the regions of self-oscillation for a number of competing modes have been plotted as a function of U and V_a. The two scenarios, V_a/U = constant and U = constant, are indicated on the graph by lines I and II respectively. Notice how line I just intersects with the TE_{521} curve at U = 40 kV, indicating that TE_{521} would be excited before the TE_{031} oscillation region is reached. In the case of startup II, TE_{031} is reached first, but the proximity of the TE_{231} curve might lead to mode competition difficulties. Fig. 3.10 indicates that the most favorable startup method would be represented by a curve that passes through the region between I and II. In practice, this would be accomplished by having the anode voltage rise lag somewhat behind the cathode voltage rise. If plotted in a manner similar to Figs. 3.9 and 3.10 this scenario would show the TE_{031} mode being excited on the higher magnetic field side of the excitation curve, away from the TE_{231} and TE_{521} curves, and then the operating point would shift to the lower field side of the TE_{031} curve in order that high efficiency operation might be achieved.

In this discussion of the effect of voltage variation on mode excitation, it was assumed that the electron beam parameters varied smoothly with voltage in a manner defined by adiabatic theory. In practice, this smooth variation may not be achieved. This would result

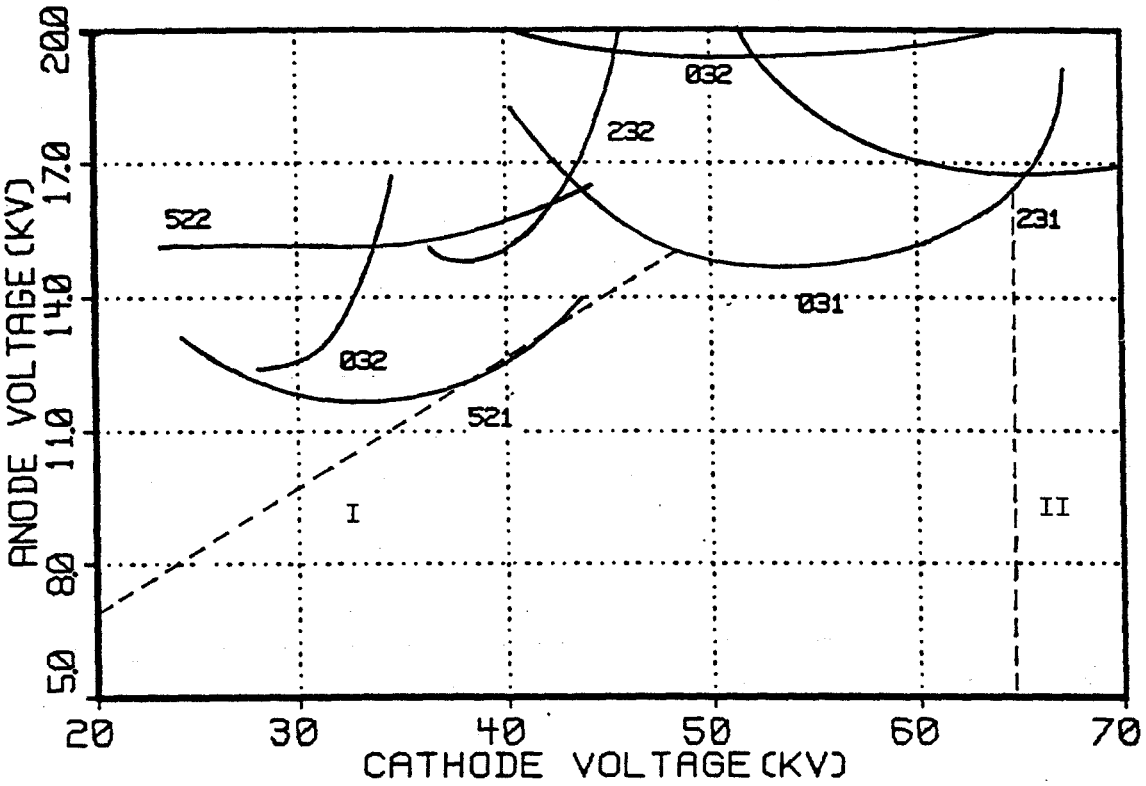

Figure 3.10 Regions of self-oscillation plotted as a function of the cathode and anode voltage. Curves based on a beam current of 6A and a resonator magnetic field of 54 kG. Line I represents the startup of Fig. 4 (V_a/U = constant), while line II is associated with the startup of Fig. 5 (U fixed, V_a increasing).

in a somewhat different sequence of mode excitation. The present results should therefore be considered as illustrative examples rather than exact, quantitative results.

Chapter 4

Design of an ECM with an Optical Resonator

In the previous chapters, it has been noted that one of the major difficulties associated with the operation of high frequency, high power gyrotrons is the suppression of extraneous modes. As the volume of the resonant cavity is enlarged to accommodate higher output powers, the spectral density increases rapidly on the gain regions of neighboring modes overlap severely. For a closed resonator, the number of TE_{mpl} and TM_{mpl} modes falling within the gain region scales approximately according to the Rayleigh-Jeans formula

$$N \propto \left(\frac{R_o}{C}\right)^2 \omega\Delta\omega \simeq \nu_{mp}^2 \left(\frac{\lambda}{L}\right)\left(\frac{u}{c}\right) \qquad (4.1)$$

where the last expression applies specifically to a cylindrical gyrotron of radius R_o operating in the TE_{mpl} mode with mode index ν_{mp} and an electron beam with a parallel velocity u. This expression was derived by assuming $\omega/c \simeq k_\perp = \nu_{mp}/R_o$ and $\Delta\omega \simeq k_\parallel u\ \Delta\nu \simeq 2\pi u/L$. If u and λ/L are held fixed, Eq. (4.1) predicts that the number of competing transverse modes N will increase by a factor of 5 when comparing gyrotrons designed specifically for fusion power reactors utilizing presently available technology (TE_{051} with $\nu_{05} = 16.47$; see Chapter 5) with present experiments (typically TE_{021} with $\nu_{02} = 7.01$). Such a large number of modes in the gain region represents a significant obstacle to the achievement of efficient, single mode operation.

A number of novel devices based on the ECM interaction have been designed in an attempt to alleviate this problem. Several utilize surface

oscillations, such as the whispering gallery modes. These modes reflect off the resonator walls at a small angle, and are consequently confined to a narrow region near the wall. The spectral density of these oscillations scales as the perimeter rather than the cross section of the resonator, which results in reduced mode overlap as the cavity volume increases. Devices that fall into this category include coaxial resonators [50] characterized by the use of a central rod that tends to suppress non-surface modes, and a scheme proposed by Zarnitsyna and Nusinovich [51]. in which the radiation is extracted from the side of the resonator rather than from the open ends.

Other designs have been proposed that rely on quasi-optical rather than microwave techniques. These are typically characterized by open resonators that are much larger than the wavelength of the output radiation. Open resonators generally exhibit better mode selection properties than closed cavities due to the increased diffractive losses of undesirable modes. Ohmic losses are also substantially reduced due to the reduction of wall surface area. It is this class of devices that will be investigated in detail in this chapter.

If an optical resonator is used, it may be possible to utilize mode suppression techniques that have been developed for the laser [52,53]. In describing the mode selectivity characteristics of laser cavities, it is necessary to distinguish between transverse and longitudinal mode selection. The former is based, as a rule, on differences in the transverse field structures of modes. Since higher order transverse modes extend farther in the radial direction than the fundamental mode, it is possible to discriminate against these higher order oscillations through the use of absorbing apertures. It is also possible to increase their diffractive losses by choosing mirror radii that are sufficiently small

so that only the fundamental mode is effectively confined. In the case of longitudinal mode selection, spatial discrimination is ineffective and it is necessary to devise loss mechanisms that are sensitive to frequency variations. It is then possible to selectively lower the Q's of all modes except the desired one. Two important types of loss mechanisms are diffraction and interferometry. Diffractive techniques, which involve the use of elements such as prisms or echelette gratings, cause radiation to be deflected out of the cavity if not at the correct frequency. Interferometric techniques achieve their purpose by varying the reflection coefficients of the confining mirrors. One of the more popular methods that falls in this category is a device first proposed by Fox and Smith [54,55] that combines versatility with low losses for the operating mode. It may also be possible to use a diffraction plate situated at one of the nulls of the desired mode that will discriminate against modes that do not have the correct standing wave pattern.

4.1 Linear Theory of a Fabry-Perot Oscillator

In this section the starting conditions of an ECM with a Fabry-Perot resonator will be derived utilizing the techniques that have been developed in earlier chapters. A number of previous studies have been done concerning both the linear [56,59] and nonlinear [57,59] characteristics of this device, and experimental investigations of its performance have been conducted [58]. However, the theoretical studies have typically been restricted to specific field profiles, such as a sinusoidal variation, thus making it difficult to evaluate the effect of tapered profiles. In addition, when performing a linear analysis of cavities with high q standing wave patterns, many authors have decomposed the standing wave

into two traveling waves and assumed that only one of these interacts effectively with the beam. It will be shown here that although the other interaction is weak, it plays an important role in determining the minimum w/u needed for emission. Finally, the beam-wave interaction will be treated here in a vigorous manner, unlike the phenomenological approach used by Kurin [56] in which he assumes the gain curve is a Lorentzian with a half-width determined by the electron transit time.

For this linear analysis, the methodology described extensively in Chapter 3 and in Appendix B has been followed with three important modifications. First, the RF field is modelled as a plane wave interacting at an arbitrary angle with the electron beam, rather than as a waveguide mode. Although the treatment of the interaction angle as a variable adds complexity to the final result, it allows this analysis to be applicable to a wide variety of device configurations. In addition, this general approach ensures that all emission mechanisms that are possible with this model will be evaluated. Secondly, since the RF $\bar{B}$ field is comparable in amplitude to the RF $\bar{E}$ field, the interaction of the electron beam with the magnetic field will not be neglected as was done in Chapter 3. Finally, the fully relativistic Vlasov equation will be utilized. Although this analysis will be performed in the weakly relativistic limit, it can be shown that factors on the order of γ can drastically affect the calculated starting currents for this device.

Figure 4.1 shows the coordinate system that will be used in this derivation. The electron beam is assumed to be a pencil beam traveling along the z axis parallel to the static magnetic field B_o. The primed system is associated with the plane wave, while the unprimed system is affiliated with the beam. Since the beam is azmuthally

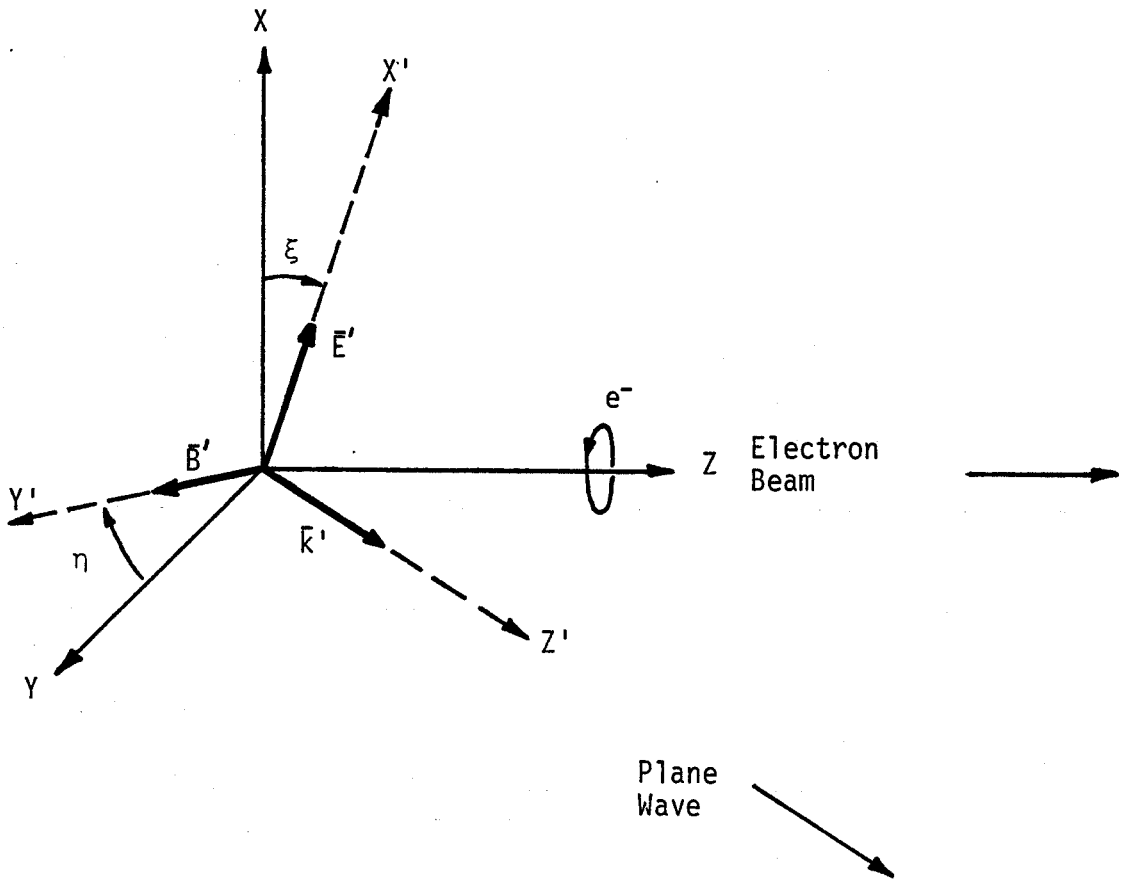

Transformation Matrix:

$$\begin{pmatrix} X \\ Y \\ Z \end{pmatrix} = \begin{pmatrix} \cos\xi & \sin\xi\sin\eta & -\sin\xi\cos\eta \\ 0 & \cos\eta & \sin\eta \\ \sin\xi & -\cos\xi\sin\eta & \cos\xi\cos\eta \end{pmatrix} \begin{pmatrix} X' \\ Y' \\ Z' \end{pmatrix}$$

Figure 4.1 The Coordinate System

symmetric, the orientation of the X and Y axes is irrelevant. However, in this model the X-axis will always be directed in the X' - Z plane. As a result, the primed and unprimed systems can be related by two angles, η and ξ. It should be noted that the RF field is assumed to be linearly polarized in this analysis. This derivation can be extended to circularly polarized radiation if the RF field is modelled as two linearly polarized waves that are 90° out of phase.

Also given in Figure 4.1 is the transformation matrix that can be used to convert a vector in one coordinate system to the other. Using this matrix, the following relations can be established:

$$\begin{aligned} k_{||} &= k_z = k'\cos\xi\cos\eta \\ \bar{E}_{||} &= \hat{z}\,E'\sin\xi \\ \bar{E}_{\perp} &= \hat{x}\,E'\cos\xi \\ \bar{B}_{||} &= \hat{z}\,B'\cos\xi\sin\eta \\ \bar{B}_{\perp} &= \hat{x}\,B'\sin\xi\sin\eta + \hat{y}B'\cos\eta \end{aligned} \tag{4.2}$$

where E' and B', the field amplitudes in the primed system, will be given explicitly shortly. These equations are used in the relativistic Vlasov equation

$$\frac{\partial f}{\partial t} + \bar{v}\cdot\frac{\partial f}{\partial \bar{r}} - e(\bar{E} + \bar{v}\times\bar{B})\,\frac{\partial f}{\partial \bar{p}} = 0 \tag{4.3}$$

which, when linearized and integrated via the method of characteristics can be written as follows:

$$f_1(\bar{p},\bar{r},t) = \int_{t-L/u}^{t} d\tau\; e\,[\bar{E}(\bar{r}(\tau),\tau) + \bar{v}(\tau)\times\bar{B}(\bar{r}(\tau),\tau)] \cdot \frac{\partial}{\partial \bar{p}} f_o(\bar{r}(\tau),\bar{p}(\tau)) \tag{4.4}$$

where f_1 is the perturbed electron distribution, $\bar{p} = \gamma m_e \bar{v}$, $\gamma = [1 + |\bar{p}|^2/m_e^2c^2]^{1/2}$, and the integration is carried out over an interaction distance L along the unperturbed electron orbit, represented here by the parameter τ. At this juncture, derivations for two models of the RF field (standing wave and traveling wave) will be continued separately.

4.1.1 Derivation for a Standing Wave

For a Fabry-Perot cavity with a TEM standing wave, the RF electric field can be written in the following form:

$$\bar{E}' = \hat{x}' \sin(k'z' + \alpha(\bar{r}')) \; g'(\bar{r}) \; e^{-i\omega t} \tag{4.5}$$

where $k' = \omega/c$. Since the radiation is assumed to be a nearly planar wave propagating predominantly along the z' axis, the longitudinal components of $\bar{E}'$ and $\bar{B}'$ can be neglected. This assumption also allows the phase shift α to be treated as a constant. The function g', which varies slowly with $\bar{r}'$, describes the variation of the field intensity (other than the sinusoidal pattern associated with the standing wave) within the resonator. This function will be kept in a general form in order to permit the study of field profiling effects.

The RF magnetic field can be obtained from $\nabla \times \bar{B} = (1/c^2)(\partial\bar{E}/\partial t)$,

$$\bar{B}' = - \hat{y}' \frac{i}{c} \cos(k'z' + \alpha) \; g'(\bar{r}') \; e^{-i\omega t} \tag{4.6}$$

Using Eqs. (4.2), the field components as seen by the electrons are

$$\begin{aligned} \bar{E} &= (E_{\parallel} \hat{Z} + \bar{E}_{\perp}) \sin(k_{\parallel} z + \alpha) \; g(\bar{r}) \; e^{-i\omega t} \\ \bar{B} &= \frac{i}{c} (B_{\parallel} \hat{Z} + \bar{B}_{\perp}) \cos(k_{\parallel} z + \alpha) \; g(\bar{r}) \; e^{-i\omega t} \end{aligned} \tag{4.7}$$

where

$$E_{\|} = \sin \xi$$

$$\bar{E}_{\perp} = \hat{x} \cos \xi$$

$$B_{\|} = \cos \xi \sin \eta$$

$$\bar{B}_{\perp} = \hat{x} \sin \xi \sin \eta - \hat{y} \cos \eta$$

and $g(\bar{r})$ is the transformation of $g'(\bar{r}')$. These equations are now substituted into Eq.(4.4). Since this analysis is concerned only with the fundamental interaction, and the variation of the RF field across the Larmor orbit is assumed to be small, the field at the gyrocenter (i.e., along the z axis) is used. Writing $\partial f_o/\partial \bar{p} = \hat{p}_{\perp} \partial f/\partial p_{\perp} + \hat{z} \partial f/\partial p_{\|}$, the integrand of Eq. (4.4) becomes

$$(\bar{E} + \bar{v} \times \bar{B}) \cdot \frac{\partial f_o}{\partial \bar{p}} = \left(\bar{E}_{\perp} \cdot \hat{p}_{\perp} \frac{\partial f_o}{\partial p_{\perp}} + E_{\|} \frac{\partial f_o}{\partial p_{\|}} \right) \sin(k_{\|} z + \alpha)\ g(z)\ e^{-i\omega t}$$

$$+ \frac{i}{\gamma m_e c} (\bar{B}_{\perp} \times \hat{p}_{\perp} \cdot \hat{z}) \left(p_{\|} \frac{\partial f_o}{p_{\perp}} - p_{\perp} \frac{\partial f_o}{\partial p_{\|}} \right) \cos(k_{\|} z + \alpha) g(z) e^{-i\omega t} \tag{4.8}$$

where $g(z) \equiv g(\bar{r})\big|_{x = y = 0}$

and $\hat{p}_{\perp}$, z, and t vary with τ. Carrying out the integration over the unperturbed helical electron orbit, along which z and ϕ, where ϕ is the angle of $\hat{p}_{\perp}$ with respect to $\hat{x}$, vary in the following manner,

$$z(\tau) = z(t) + (p_{\|}/\gamma m_e)(\tau - t)$$

$$\phi(\tau) = \phi(t) + \omega_c(\tau - t)$$

where

$$\omega_c \equiv eB_o/\gamma m_e$$

allows the perturbed electron distribution to be determined:

$$f_1(\bar{p},\bar{r},t) = e\int_0^{L/u} d\delta \left\{ \left[(\bar{E}_\perp \cdot \hat{p}_\perp)\cos\omega_c\delta + (\bar{E}_\perp \times \hat{p}_\perp \cdot \hat{z})\sin\omega_c\delta \right] \frac{\partial f_0}{\partial p_\perp} + E_\parallel \frac{\partial f_0}{\partial p_\parallel} \right\}$$

$$\cdot \sin\left[k_\parallel(z-u\delta)+\alpha\right] g(z-u\delta) e^{-i\omega(t-\delta)} + \frac{i}{\gamma m_e c}\left[(\bar{B}_\perp \times \hat{p}_\perp \cdot \hat{z})\cos\omega_c\delta \right.$$

$$\left. -(\bar{B}_\perp \cdot \hat{p}_\perp)\sin\omega_c\delta \right] \left(p_\parallel \frac{\partial f_0}{\partial p_\perp} - p_\perp \frac{\partial f_0}{\partial p_\parallel} \right) \cos\left[k_\parallel(z-u\delta)+\alpha\right] g(z-u\delta) e^{-i\omega(t-\delta)} \qquad (4.9)$$

where $\delta = t - \tau$. The perturbed current can now be calculated by integrating over velocity space,

$$\bar{J} = -eN\int d^3\bar{p}\; f_1(\bar{p},\bar{r},t)\left(\frac{\bar{p}}{\gamma m_e}\right) \qquad (4.10)$$

where N = electron density (particles/meter)

and from this the work done by the RF field on the electrons, P_{RF}, is determined by integrating $\bar{J} \cdot \bar{E}_1^*$ over the interaction path,

$$P_{RF} = \mathrm{Re}\int_{-\infty}^{\infty} dz\; \bar{J}\cdot\bar{E}_1^* = -Ne^2\pi(2k_\parallel^2)^{-1}\int_0^\infty p_\perp^2\, dp_\perp \int_{-\infty}^{\infty} p_\parallel^{-1}\, dp_\parallel \left\{ |\bar{E}_\perp|^2 F_1 \frac{\partial f_0}{\partial p_\perp} + 2\left(\frac{p_\parallel}{p_\perp}\right) E_\parallel^2 F_3 \frac{\partial f_0}{\partial p_\parallel} \right.$$

$$\left. -\frac{1}{\gamma m_e c}\left[(\bar{E}_\perp \times \bar{B}_\perp \cdot \hat{z}) F_2 + (\bar{E}_\perp \cdot \bar{B}_\perp) F_4 \right] \left(p_\parallel \frac{\partial f_0}{\partial p_\perp} - p_\perp \frac{\partial f_0}{\partial p_\parallel} \right) \right\} \qquad (4.11)$$

where the integration over ϕ has already been performed. Note that, in contrast to the derivation in Chapter 3 in which one gain function F_c was obtained for the starting current, four gain functions (F_1 through F_4) are obtained here. These will now be examined in detail.

The first function, F_1, can be written as follows,

$$F_1 = \mathrm{Re}\ 2k_{\|}^2 u \int_{-\infty}^{\infty} dz \int_0^{\infty} d\delta \cos \omega_c \delta \sin(k_{\|} z + \alpha)\ g(z) \sin\left[k_{\|}(z-u\delta)+\alpha\right] g(z-u\delta) e^{i\omega\delta} \tag{4.12}$$

In this equation L/u has been replaced by infinity since g contains the necessary information about the interaction distance. Defining $\lambda \equiv k_{\|} \delta u$ and $\tilde{z} \equiv k_{\|} u$, and keeping only the resonant term,

$$\mathrm{Re}\ 2 \cos \omega_c \delta e^{i\omega\delta} = \cos(\omega_c - \omega)\delta + \cos(\omega_c + \omega)\delta \simeq \cos x\lambda$$

F_1 can be rewritten as

$$F_1 = \int_{-\infty}^{\infty} d\tilde{z} \int_0^{\infty} d\lambda \sin(\tilde{z} + \alpha)\ g(\tilde{z}) \sin(\tilde{z} + \alpha - \lambda)\ g(\tilde{z} - \lambda) \cos(x\lambda) \tag{4.13}$$

F_1 has the same form and symmetry as F_c in Chapter 3, and therefore quickly reduces to

$$F_1 = \pi\ G_1(x)\ G_1^*(x)$$

where
$$G_1(x) = (2\pi)^{-1/2} \int_{-\infty}^{\infty} \sin(a + \alpha)\ g(a)\ e^{ixa}\ da \tag{4.14}$$

The function F_2, associated with the magnetic interaction, is given by

$$F_2 = \int_{-\infty}^{\infty} d\tilde{z} \int_0^{\infty} d\lambda \sin(\tilde{z} + \alpha)\ g(\tilde{z}) \cos(\tilde{z} + \alpha - \lambda)\ g(\tilde{z} - \lambda) \sin(x\lambda) \tag{4.15}$$

where again only the resonant term is retained. This equation can be further simplified if $\sin(\tilde{z} + \alpha)\ g(\tilde{z})$ and $\cos(\tilde{z} + \alpha)\ g(\tilde{z})$ have opposite symmetries about some $\tilde{z}$. In this case, the lower limit of the λ integral can be extended to $-\infty$,

$$F_2 = \frac{1}{2} \int_{-\infty}^{\infty} d\tilde{z} \int_{-\infty}^{\infty} d\lambda \sin(\tilde{z} + \alpha)\ g(\tilde{z})\ \cos(\tilde{z} + \alpha - \lambda)\ g(\tilde{z} - \lambda)\ \sin(x\lambda) \tag{4.16}$$

In this form, Fourier techniques utilized in conjunction with F_1 are applicable, yielding the final result:

$$F_2 = \pi\ \mathrm{Im}[G_1(x)\ G_2^*(x)] \tag{4.17}$$

where $$G_2(x) = (2\pi)^{-1/2} \int_{-\infty}^{\infty} \cos(a + \alpha)\ g(a)\ e^{ixa}\ da$$

and $G_1(x)$ is defined in Eq. (4.14).

The function F_3 is very similar in form to F_1 except cos $\omega_c \delta$ is missing. This is understandable since F_3 is associated with the $\bar{E}_{\|}$ interaction which is unaffected by the gyrating electron motion in the transverse plane. This term is closely related to the gain mechanism of a klystron, which results from an anisotropic distribution of the parallel electron velocity. Following the derivation of F_1 gives

$$\begin{aligned} F_3 &= R\ \ 2\int_{-\infty}^{\infty} dz \int_{0}^{\infty} d\lambda \sin(\tilde{z} + \alpha)\ g(\tilde{z})\ \sin(\tilde{z}+\alpha-\lambda)\ g(\tilde{z}-\lambda) e^{i\left(\frac{\omega}{k_{\|}u}\right)\lambda} \\ &= 2\pi G_1(\omega/k_{\|}u)\ G_1^*(\omega/k_{\|}u) \end{aligned} \tag{4.18}$$

Note that for a fast wave device such as a gyrotron $\omega/k_{\|}\, u >> 1$. At these values of $\omega/k_{\|}\, u$, G_1 is typically very small, and as a result F_3 can often be neglected.

Finally, the other magnetic gain function, F_4, can be related to F_2 via the Kramers-Kronig relations [38],

$$F_4 = -\int_{-\infty}^{\infty} d\tilde{z} \int_{0}^{\infty} d\lambda \sin(\tilde{z} + \alpha)\ g(\tilde{z})\ \cos(\tilde{z} + \alpha - \lambda)\ g(\tilde{z}-\lambda)\ \cos\ (x\lambda) \tag{4.19}$$

or

$$F_4 = \frac{1}{\pi} \text{P.V.} \int_{-\infty}^{\infty} \frac{F_2(a)}{(x-a)}\, da$$

Returning to Eq. (4.11), the derivatives of f_o can be eliminated by performing an integration by parts on each term. In order to obtain the ECM mechanism, the dependence of ω_c on γ must be retained. Although the cyclotron frequency does not appear explicitly, the parameter $x \equiv (\omega_c - \omega)/k_{||} u$ is a function of ω_c. Eq. (4.11) becomes

$$P_{RF} = \text{Re} \int_{-\infty}^{\infty} dz\, \bar{J} \cdot \bar{E}_1^* = N e^2 \pi (k_{||})^{-2} \int_0^{\infty} dp_\perp \int_{-\infty}^{\infty} dp_{||} f_o(\bar{p}) \left\{ |\bar{E}_\perp|^2 \left(\frac{p_\perp}{p_{||}}\right) F_1 \right.$$

$$- \frac{1}{2} |\bar{E}_\perp|^2 \left(\frac{\omega}{k_{||} c}\right) \left(\frac{p_\perp^3}{p_{||}^2}\right) \frac{1}{\gamma m_e c} \frac{dF_1}{dx} - \frac{1}{\gamma m_e c} \left(p_\perp + \frac{1}{2} \frac{p_\perp^3}{p_{||}^2} + \frac{x}{2} \frac{p_\perp^3}{p_{||}^2} \frac{d}{dx}\right)$$

$$\left. \left[(\bar{E}_\perp \times \bar{B}_\perp \cdot \hat{z}) F_2 + (\bar{E}_\perp \cdot \bar{B}_\perp) F_4 \right] - E_{||}^2 \left(\frac{\omega}{k_{||} c}\right) \gamma m_e c \left(\frac{p_\perp}{p_{||}^2}\right) \frac{dF_2}{dx} \right|_{x = \frac{\omega}{k_{||} u}} \Bigg\} \qquad (4.20)$$

The final step is to relate P_{RF} to the starting current, I_{ST}. This is accomplished by noting that, at equilibrium, the power loss in the resonator must just equal $- P_{RF}$ (the minus sign signifies power flow to the RF field). Defining the power loss in terms of the cavity Q, the stored energy in the cavity E_s, and the time-averaged power loss $\langle P \rangle$,

$$Q = \frac{E_s \omega}{\langle P \rangle}$$

where

$$E_s = \frac{1}{2} \varepsilon_o \int d^3 \bar{r}'\, \bar{E}' \cdot \bar{E}'^*$$

$$\langle P \rangle = - \frac{1}{2} P_{RF} = - \frac{1}{2} \int_{-\infty}^{\infty} dz\, \bar{J} \cdot \bar{E}^*$$

and relating N to the electron current, $I = Ne\,(\langle p_{||}\rangle/\gamma m_e)$, where $\langle p_{||}\rangle$ is the average parallel momentum, the following equation for I_{ST} can be written:

$$I_{ST} = -\frac{2\omega}{Q} E_s k_{||}^2 \left(\frac{\langle p_i\rangle}{\gamma m_e}\right)\Big[e\pi \int_0^\infty dp_\perp \int_{-\infty}^\infty dp_{||}\, f_o(\bar{p})\Big\{|E_\perp|^2\left(\frac{p_\perp}{p_{||}}\right)F_1$$

$$-\frac{1}{2}|\bar{E}_\perp|^2\left(\frac{\omega}{k_{||}c}\right)\left(\frac{p_\perp^3}{p_{||}^2}\right)\frac{1}{\gamma m_e c}\frac{dF_1}{dx} - \frac{1}{\gamma m_e c}\left(p_\perp + \frac{1}{2}\frac{p_\perp^3}{p_{||}^2} + \frac{x}{2}\frac{p_\perp^3}{p_{||}^2}\frac{d}{dx}\right)$$

$$\left[(\bar{E}_\perp \times \bar{B}_\perp \cdot \hat{z})F_2 + (\bar{E}_\perp \cdot \bar{B}_\perp)F_4\right] - E_{||}^2\left(\frac{\omega}{k_{||}c}\right)\gamma m_e c\left(\frac{p_\perp}{p_{||}^2}\right)\frac{dF_3}{dx}\Big|_{x=\frac{\omega}{k_{||}u}}\Big\}\Big]^{-1} \qquad (4.21)$$

A quick comparison with the results of Chapter 3 indicated that this expression is consistent with Eq. (3.14) if $\bar{B}_\perp$ and $E_{||}$ are set to zero, and the geometric factor $G(R_e)$ is replaced by one.

4.1.2 Derivation for a Traveling Wave

In this section, the RF field will be modelled as a TEM traveling wave with the following field components:

$$\bar{E}' = \pm\ \hat{x}'\ e^{\pm i(k'z' + \alpha)}\ g'(\bar{r}')e^{-i\omega t}$$
$$\bar{B}' = \hat{y}'\ e^{\pm i(k'z' + \alpha)}\ g'(\bar{r}')\ e^{-i\omega t} \qquad (4.22)$$

where the plus sign signifies a forward wave, while the minus sign corresponds to a backward wave. In the beam frame, these can be written as

$$\bar{E} = (E_{||}\,\hat{z} + \bar{E}_\perp)\ e^{\pm i(k_{||}\,z + \alpha)}\ g(\bar{r})\ e^{-i\omega t}$$

$$\bar{B} = (B_{||}\,\hat{z} + \bar{B}_\perp)\ e^{\pm i(k_{||}\,z + \alpha)}\ g(\bar{r})\ e^{-i\omega t}$$

where

$$E_{\|} = \pm \sin \xi$$

$$\bar{E}_{\perp} = \pm \hat{x} \cos \xi$$

$$B_{\|} = - \cos \xi \sin \eta$$

$$\bar{B}_{\perp} = \hat{x} \sin \xi \sin \eta + \hat{y} \cos \eta \qquad (4.23)$$

Comparing this set of equations with Eqs. (4.7), one can see that the major modification is the z-dependence of the RF field. Much of the methodology used in the standing wave problem is applicable here and will not be repeated. The power transfer to the electrons, P_{RF}, has the same form as Eq. (4.20) with the following new gain functions:

$$F_1 = R_e \, 2k_{\|}^2 u \int_{-\infty}^{\infty} dz \int_0^{\infty} d\delta \cos \omega_c \delta e^{\mp i k_{\|} u \delta + i\omega\delta} g(z) \, g(z-u\delta) \qquad (4.24)$$

$$= \frac{1}{2} \int_{-\infty}^{\infty} d\tilde{z} \int_{-\infty}^{\infty} d\lambda \cos \left[(x \pm 1)\lambda \right] g(\tilde{z}) \, g(\tilde{z}-\lambda)$$

$$= \pi L(x \pm 1) \, L^*(x \pm 1) \text{ where } L(x) = (2\pi)^{-\frac{1}{2}} \int_{-\infty}^{\infty} g(a) e^{ixa} \, da$$

$$F_2 = F_1$$

$$F_3 = R_e \, 2k_{\|}^2 u \int_{-\infty}^{\infty} dz \int_0^{\infty} d\delta e^{\mp i k_{\|} u \delta + i\omega\delta} g(z) \, g(z-u\delta)$$

$$= 2\pi \, L \left[\left(\frac{\omega}{k_{\|} u} \right) \mp 1 \right] \, L^* \left[\left(\frac{\omega}{k_{\|} u} \right) \mp 1 \right]$$

$$F_4 = R_e \, 2k_{\|}^2 u \int_{-\infty}^{\infty} dz \int_0^{\infty} d\delta \sin \omega_c \delta e^{\mp i k_{\|} u \delta + i\omega\delta} g(z) \, g(z-u\delta)$$

$$= \pi^{-1} \, P.V. \int_{-\infty}^{\infty} \frac{F_1(a)}{(x-a)} \, da$$

Using these results, the starting current can be calculated in the same manner as Eq. (4.21) was derived.

It is now possible to compare the gain functions derived from the standing and traveling wave models to see if they yield different results. This will allow us to determine if an oscillator operating in a high q mode can be treated as a traveling wave problem, an approach used by some previous authors. This comparison will be done in the next section.

4.2 Characteristics of Results

In this section, the results of the linear analysis just completed will be investigated in greater detail. This will include an examination of the various terms in Eq. (4.20) and their origins, a study of the gain functions and their dependence upon x, and a comparison of the standing and traveling wave theories. In addition, the starting characteristics of a confocal resonator operating at 140 GHz will be calculated in order to determine the beam currents that will be required and better understand the mode competition problems that might be encountered.

Table 4.1 gives a listing of the terms of Eq. (4.20) and their characteristics, including the field component responsible for the bunching process in each case and conditions under which the electrons lose energy ($P_{RF} < 0$). Also given are the types of devices that could be built based on the various emission mechanisms. Each term will now be described briefly.

Term 1: This term always results in net energy absorption by the electrons. Those electrons that gain perpendicular energy from the RF field increase their gyro-radius (ω_c is a constant), and as a result their interaction with the field occur over a longer path than those electrons that lose

Table 4.1: Classification of Beam-Field Interactions

	Term	Bunching Field	Bunching	$P_{RF} < 0$ When	Type of Device
1.	$\lvert E_\perp \rvert^2 \left(\frac{p_\perp}{p_\parallel}\right) F_1$	Transverse Electric	Radial: $r_L(p_\perp)$	Never	----------
2.	$\frac{1}{2} \lvert E_\perp \rvert^2 \left(\frac{\omega}{k_\parallel c}\right) \cdot \left(\frac{p_\perp^3}{p_\parallel^2}\right) \frac{1}{\gamma m_o c} \frac{dF_1}{dx}$	Transverse Electric	Azimuthal: $\omega_c(\gamma)$	$\frac{dF_1}{dx} > 0$	Relativistic; $\bar{E}_{1\perp} \hat{z}_\perp \bar{k}$
3.	$\frac{p_\perp}{\gamma m_o c} T_B$	Transverse Magnetic	Radial: $r_L(p_\perp)$	$T_B > 0$	Nonrelativistic; $\bar{k} \parallel \hat{z}$
4.	$\frac{1}{2} \frac{p_\perp^3}{p_\parallel^2} T_B$	Transverse Magnetic	Axial: $\tau_{in}(p_\parallel)$	$T_B > 0$	Same As 3.
5.	$\frac{x}{2} \frac{p_\perp^3}{p_\parallel^2} \frac{dT_B}{dx}$	Transverse Magnetic	Axial: $x(p_\parallel)$	$x \frac{dT_B}{dx} > 0$	Same As 3.
6.	$E_\parallel^2 \left(\frac{\omega}{k_\parallel c}\right) \gamma m_o c \left(\frac{p_\perp}{p_\parallel^2}\right) \cdot \frac{dF_3}{dx}\Big\rvert_{x = \frac{\omega}{k_\parallel u}}$	Longitudinal Electric	Axial: $p_\parallel(t_{in})$	$\frac{dF_3}{dx}\Big\rvert_{x = \frac{\omega}{k_\parallel u}} > 0$	Slow Wave; not a cyclotron resonance interaction

$$T_B \equiv (\bar{E}_\perp \times \bar{B}_\perp \cdot \hat{z}) F_2 + (\bar{E}_\perp \cdot \bar{B}_\perp) F_4$$

t_{in} = Time Electron Enters Cavity

τ_{in} = Interaction Time

energy and consequently have smaller Larmor radii. No maser is possible with this interaction. This mechanism can lead to ECR heating in plasmas.

Term 2: This corresponds to the relativistic interaction studied extensively in Chapter 3. The dependence of ω_c on $p_\perp$ via the γ factor causes a phase bunching, and emission can occur when $dF_1/dx > 0$. This term dominates when the beam and field propagate at right angles to one another, that is, when $(\omega/k_{||}\, c) >> 1$ and $\bar{E}_1$ is perpendicular to $\hat{z}$.

Term 3: This, as well as terms 4 and 5, result from the transverse magnetic component. In this case, the mechanism is the same as that of term 1, except the bunching force that causes r_L to vary is $\bar{p}_{||} \times \bar{B}_\perp$ rather than $\bar{E}_\perp$. All the magnetic interactions involve $\bar{E}_\perp$ and $\bar{B}_\perp$, and these vectors are largest when the beam and wave are propagating in the same direction. This particular mechanism has not been derived explicitly in previous works.

Term 4: The force involved here is $\bar{p}_\perp \times \bar{B}_\perp$, which alters the parallel momentum and causes axial bunching. This results in variations in the electron-field interaction time τ_{in}, and by proper selection of operating parameters it is possible for electrons losing energy to interact longer than those gaining energy, thus leaving the RF wave with a net energy gain. As with term 3, the emission requirement is $T_B > 0$, where T_B is defined in the table.

Term 5: The variations of $p_{||}$ due to $\bar{p}_\perp \times \bar{B}_1$ also causes x (i.e. the phase difference between the wave frequency, ω, and ω_c) to be different for each electron. Therefore the gain function, which is a measure of how effectively the electron and wave interact, is slightly different for each particle. Emission occurs when those electrons losing energy move into resonance with the field as their x's change, while those gaining

energy move out of resonance. This term, as well as term 4, involve axial bunching of the electrons, and are sometimes classified as Weibel-type interactions [60].

Term 6: The $E_{||}$ interaction, which is independent of the gyro-motion, is best suited for a slow wave device since the phase velocity $\omega/k_{||}$ must be comparable to u in order for the gain function not to be negligible. The mechanism involved here is very similar to that of term 5 except it is $E_{||}$ that causes $p_{||}$ to vary, and also extracts energy from (or gives energy to) the electrons.

It is interesting to note that the only relativistic bunching process that occurs involves the transverse electric field component. The fact that the magnetic field yields only nonrelativistic terms is understandable if one remembers that $\bar{v} \times \bar{B}$ forces cannot change the total energy of a particle (although the ratio of energy in the parallel and perpendicular directions can be altered). Since the total electron energy is unchanged by the magnetic interaction, phase bunching due to variations of γ is not possible.

In order to better understand the functional dependence of the gain functions on x, $F_1 (= F_3)$, F_2, F_4 and their derivatives have been plotted in Fig. 4.2. for an oscillator with a uniform field profile ($g(\tilde{z}) = 1$ for $0 \leq \tilde{z} \leq q\pi$) and $\alpha = 0$. These functions can be expressed as follows:

$$
\begin{aligned}
F_1(x) &= 2(1 - x^2)^{-2} \sin^2\left[\frac{q\pi}{2}(1 + x)\right] \\
F_2(x) &= xF_1(x) \\
F_4(x) &= \frac{x}{(x^2 - 1)^2}\left[\frac{q\pi(x^2 - 1)}{2x} - \sin q\pi(x + 1)\right]
\end{aligned}
\tag{4.25}
$$

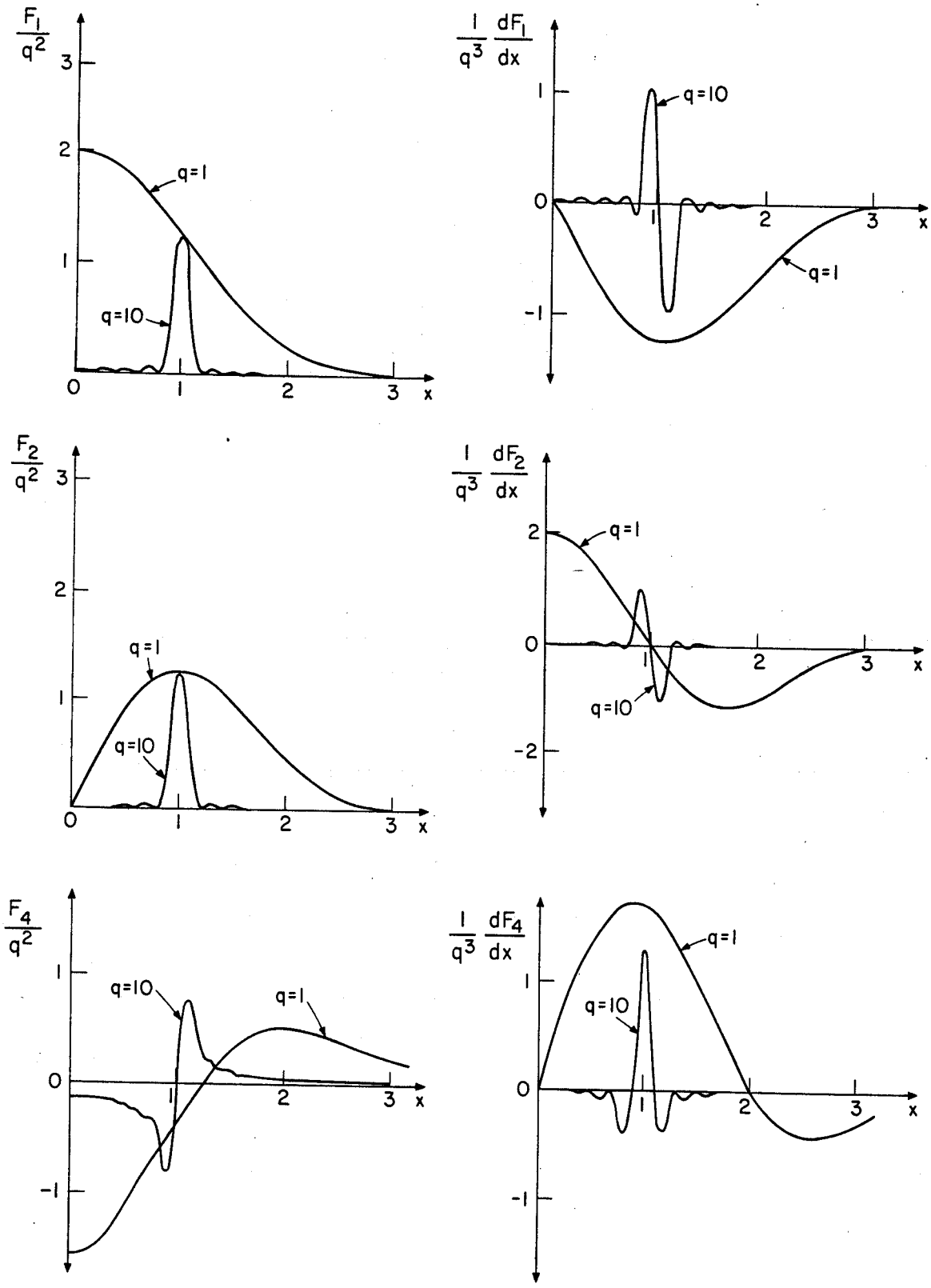

Figure 4.2 Gain Functions and Their Derivatives

These have been plotted for two values of q, and for positive x only. They can be extended to negative x by noting that F_1 and F_4 are even functions, while F_2 is odd. These graphs show that F_j/q^2 and $(dF_j/dx)/q^3$ are bounded by 2 and -2, and that they become negligible as $|x|$ increases. This indicates that, for large q, the derivatives can be much greater in value than the gain functions. Also noteworthy is the fact that as q increases, these functions compress to regions around $x = \pm 1$. However, this does not imply that the gain curves, when plotted versus magnetic field, become narrower as q gets larger. If ΔB is the typical halfwidth of a gain curve, the following scaling holds true:

$$\frac{\Delta B}{B} \sim \frac{\Delta\omega_c}{\omega_c} \sim \frac{k_{||}\, u\Delta x}{\omega} \sim \left(\frac{\lambda}{L}\right)\beta_{||}$$

where the width of the gain curve in terms of x, Δx, was taken as $2/q$ (Fig. 4.2 confirms this approximation). This scaling indicates that $\Delta B/B$ is independent of q.

The results of the two previous sections have been compared with those of earlier studies with good agreement. Sprangle et.al. [59] have calculated P_{RF} for an electron beam intercepting a standing wave at right angles. Expressions were obtained for two polarizations, TE($\bar{B}_\perp \simeq 0$) and TM($\bar{E}_\perp \simeq 0$), and for all harmonics. Limiting our attention to the fundamental interaction, it was found that these equations for P_{RF} agreed with Eq. (4.11) when the correct limits were taken. The $|\bar{E}_\perp|^2$ term corresponded to the TE interaction, while the $E_{||}^2$ term gave the TM results. It is interesting to note that the TE configuration is equivalent to a gyrotron with a Gaussian profile, so that the results of Chapter 3 are applicable to this problem.

Kurin [56] has calculated the electron conductivity for the case where both the beam and wave propagate along the same axis ($\bar{k} \| \hat{z}$; both forward and backward interactions). Emission occurs when this conductivity is negative. A comparison with the results of this chapter is difficult due to the fact that Kurin solves the traveling wave problem in a phenomenological manner that basically gives the correct answer but not the exact solution. However, if his gain function ($[1 + (x \pm 1)^2 q^2\pi^2]^{-1}$) is substituted for F_1 and F_2 in Eq. (4.20), his expression for conductivity can be derived.

The general results that were obtained in the previous sections can be specialized to two device configurations that are presently being analyzed in detail: $\bar{k} \perp \bar{B}_o$ and $\bar{k} \| \bar{B}_o$. Returning to Eq. (4.21), the starting current for the former case can be obtained by setting η equal to either $\pi/2$ or $3\pi/2$. If the following assumptions are also made:

i) the beam has no velocity spread: $f_o = (2\pi p_\perp)^{-1} \delta(p_\perp - p_\perp^0) \delta(p_\| - p_\|^0)$

ii) the RF field has a Gaussian transverse profile:

$$E \propto \exp(-r^2/r_o^2)$$

then I_{ST} for a beam of small radial thickness (pencil beam) can be written as

$$I_{ST} = -\pi\left(\frac{\omega\epsilon_o}{Q}\right)\left(\frac{\gamma m_e}{2e}\right)\left(\frac{p_\|^0}{\gamma m_e}\right)^2 L\left\{\left[\frac{E_\perp^2}{E_o^2} + \left(\beta_\| + \frac{1}{2}\frac{\beta_\perp^2}{\beta_\|^2}\right)\frac{E_\perp B_\perp}{E_o^2}\right] F + \frac{1}{2}\left(\frac{\beta_\perp^2}{\beta_\|}\right)\left[\left(\frac{E_\perp B_\perp}{E_o^2}\right)X - \frac{E_\perp^2}{E_o^2}\left(\frac{\omega r_o}{c}\right)\right]\frac{dF}{dx}\right\}^{-1} \tag{4.26}$$

where $E_\perp = E_o \cos\xi \sin\alpha$

$B_\perp = \pm E_o \sin\xi \cos\alpha$

$F = \frac{\pi}{2}\exp(-x^2/2)$

$$X = \left(\frac{\omega_c - \omega}{u}\right) r_o$$

L is the resonator length, and ξ and α are angles that can be varied. Changing ξ is equivalent to varying the orientations of the $\bar{E}$ and $\bar{B}$ vectors with respect to the beam. Changing α is the same as moving the beam in the $\hat{z}'$ direction so that it interacts with different peaks of the standing wave pattern. The two signs in $B_\perp$ result from the two possible values for η. In this equation the $E_{||}$ interation, which is usually small, has been omitted. If ξ is set equal to zero (the TE case), the magnetic terms do not play a role, and one is left with a "pure" gyrotron interaction involving $E_\perp^2$.On the other hand, for the TM case with $\xi = \pi/2$, $E_\perp$ is zero and none of the terms of Eq. (4.26) survive, leaving only the weak $E_{||}$ mechanism. Eq. (4.26) indicates that for $\bar{k} \perp \bar{B}_o$, the TE configuration will always give the lowest starting currents since $r_o \gtrsim c/\omega$ is always true.

If $\bar{k}$ is parallel to $\bar{B}_o$ (TEM case), and we again assume no velocity spread, the following expression for I_{ST} is obtained for a pencil beam:

$$I_{ST} = -4\left(\frac{\omega}{Q}\right) E_s \left(\frac{\gamma m_e}{e}\right)\left(\frac{P_{\perp}^{o}}{\gamma m_e}\right)^2 \left(\frac{\omega}{c}\right)^2 \left[F_1 - \frac{1}{2}\left(\frac{\beta_\perp^2}{\beta_{\perp}}\right)\frac{dF_1}{dx} + \left(\beta_{\perp} + \frac{1}{2}\frac{\beta_\perp^2}{\beta_{\perp}} + \frac{X}{2}\frac{\beta_\perp^2}{\beta_{\perp}}\frac{d}{dx}\right)F_2\right]^{-1} \tag{4.27}$$

where E_S has been kept in a general form. When compared with Eq. (4.26), one finds that the coefficient of the above equation is larger by a factor of $r_o^2\omega^2/c^2$ for the same RF field distribution. Also contributing to the higher starting currents required for the $\bar{k} \,||\, \bar{B}_o$ configuration is

the fact that the electric and magnetic gain mechanisms tend to offset one another. Both E_S and I_{ST} will be calculated explicitly in a later example involving a confocal resonator operating at 140 GHz.

Before one calculates starting currents and subsequently generates mode spectra, it is necessary to know the regions in x where emission is possible. These regions can be determined by finding those values of x that cause the expression within the brackets of Eq. (4.21) to be negative. If we limit our attention to a standing wave resonator with $\bar{k} \| \bar{B}_o$ and a uniform profile, Eq. (4.25) and (4.27) yield the following condition for emission:

$$\left(\frac{w}{u}\right)^2 > \frac{2F_1 \left(\beta_{\|}^{-1} + x\right)}{(1 - x^2) \frac{dF_1}{dx} - 2xF_1} \tag{4.28}$$

$$\text{where } F_1 = 2(1 - x^2)^{-2} \sin^2\left[\frac{q\pi}{2}(1 + x)\right]$$

The minimum w/u has been plotted versus x in Figures 4.3(a) and 4.4(a) for $\beta_{\|} = 0.2$ and two values of q: 1 and 10. These graphs indicate that, for q = 10, there is no minimum w/u needed for emission, and that as long as the beam has some perpendicular energy RF output is possible. This conflicts with previous claims [56] that a minimum w/u is required. However, as the ratio w/u of the beam decreases, the gain curves will become narrower, and the minimum starting currents needed for emission become larger. One also observes that as q is increased, the emission regions get narrower and bunch up. As a result each high q mode is characterized by a series of gain curves. This is shown in Figures

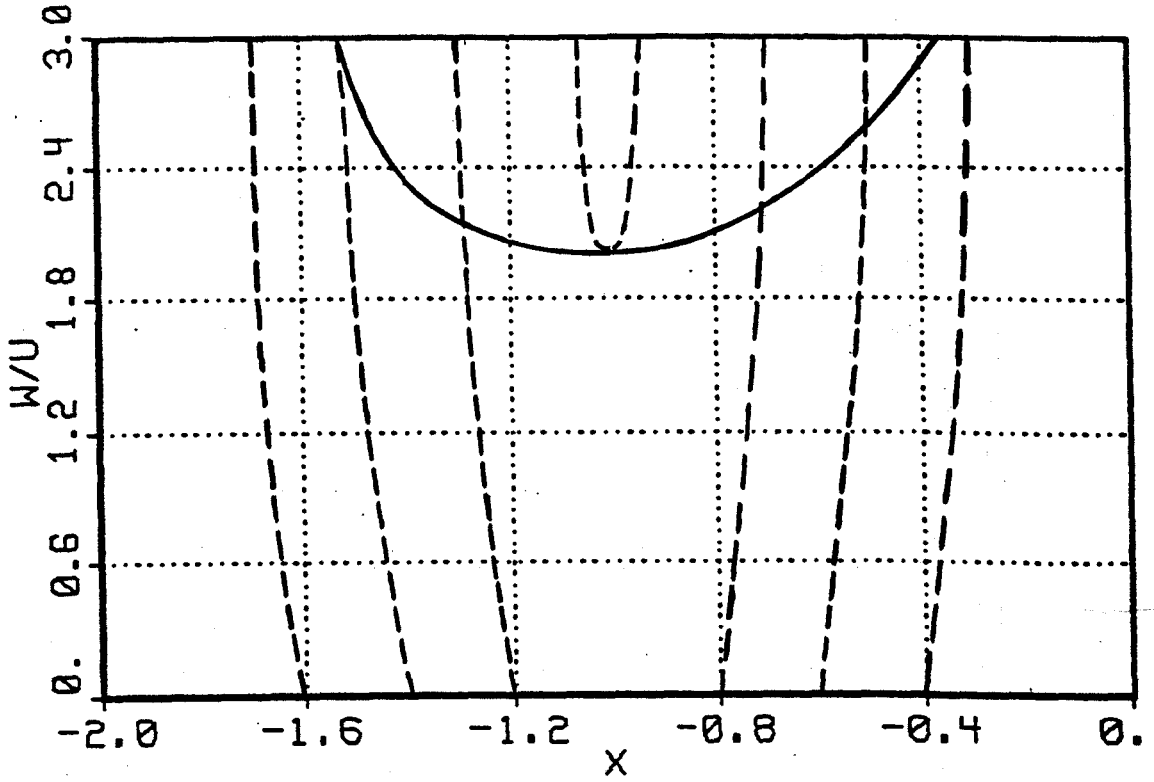

Figure 4.3(a): Minimum w/u for q = 1 (Solid) and q = 10 (Dash). $\beta_{||} = 0.2$.

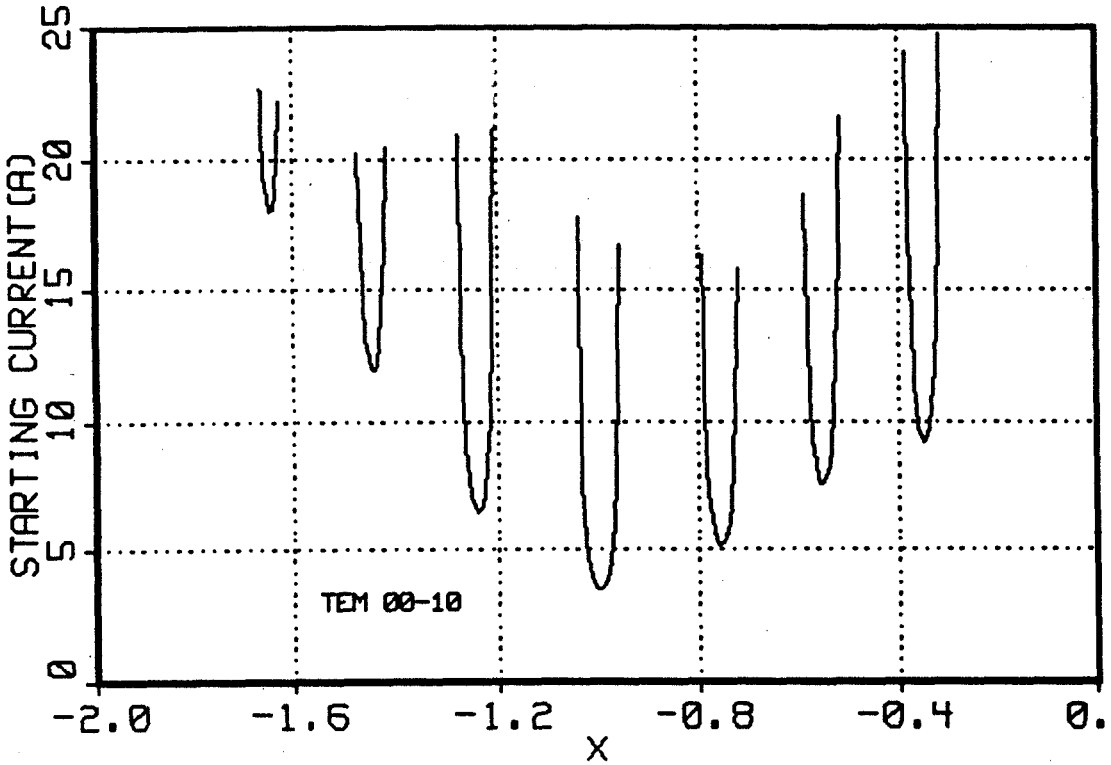

Figure 4.3(b): Characteristic Gain Curves for w/u = 2.5 and q = 10.

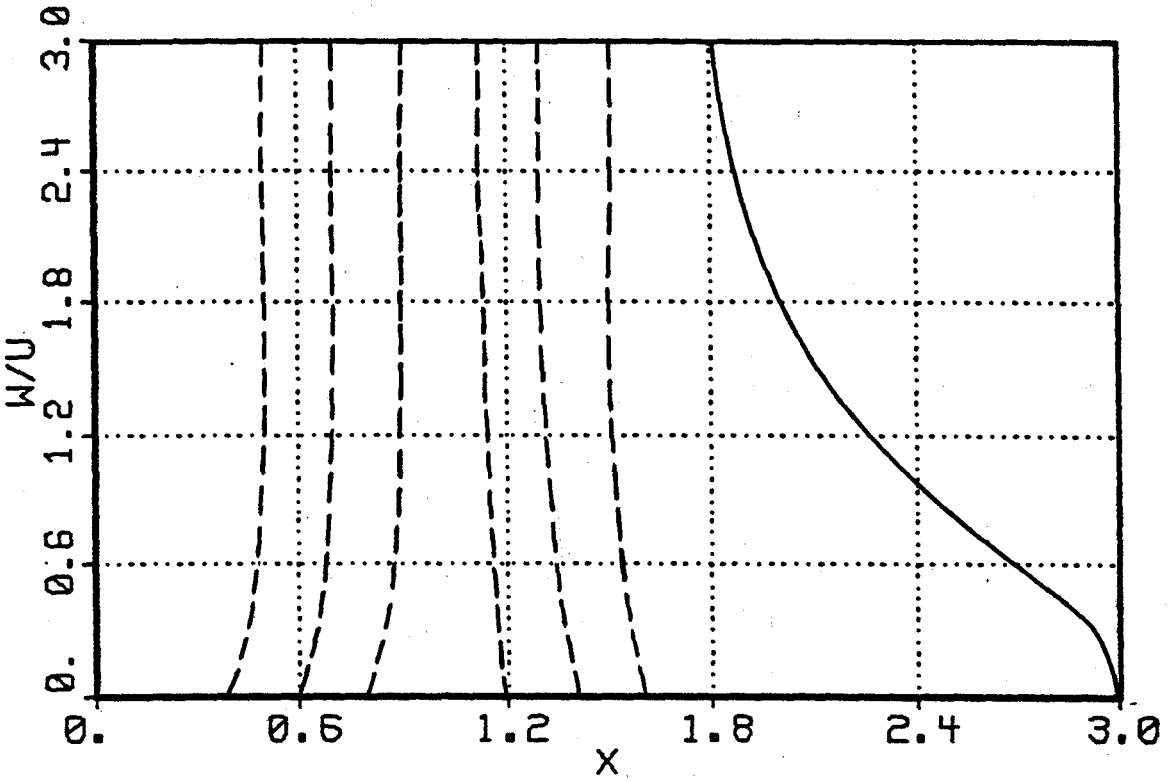

Figure 4.4(a): Minimum w/u for q = 1 (Solid) and q = 10 (Dash). $\beta_{||} = 0.2$.

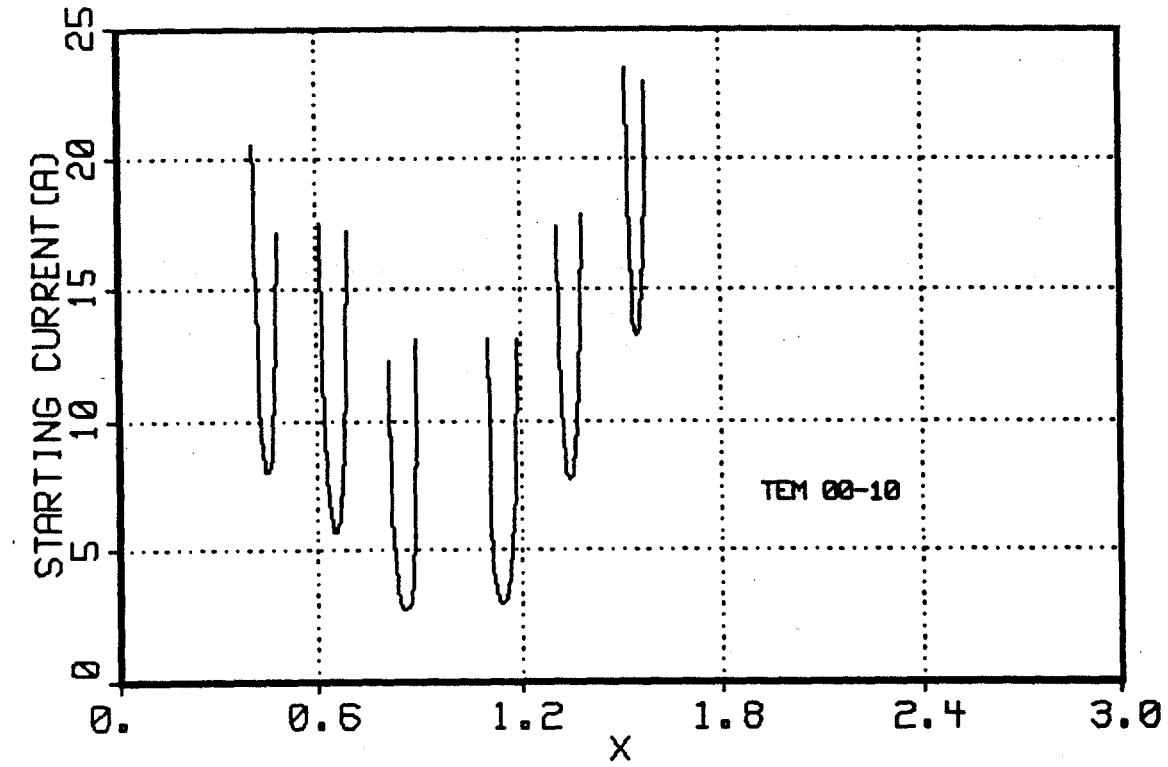

Figure 4.4(b): Characteristic Gain Curves for w/u = 2.5 and q = 10.

4.3(b) and 4.4(b), where I_{ST} has been plotted for a typical q = 10 TEM mode with w/u = 2.5 using Eq. (4.27). It is interesting to note that, although the sidebands of the gain functions shown in Figure 4.2 appear negligible, they do lead to gain curves with starting currents that are comparable to the I_{ST} of the main branch at x = -1.

Some confusion has arisen in the past concerning the proper treatment of the standing wave problem in the case of high q modes. A number of authors have assumed that the standing wave can be decomposed into two traveling waves, and that the starting current can be solved for each traveling wave without considering the other wave. This assumption is supported by the fact that as q increases, the forward and backward resonant interactions become more distinct and separable. This is reflected by the gain function F_1, given by Eq. (4.24), which produces peaks at each of the synchronous points, $x = \pm 1$, depending on which interaction is selected. However, a comparison of the traveling and standing results derived earlier in this chapter indicates that cross terms, albeit small, do exist and that they can play a role under certain circumstances. These cross terms occur because one wave is involved in the electron bunching process, while the other is responsible for energy extraction.

The contributions of these cross terms is most evident when one compares the emission conditions for the traveling and standing wave cases. Eq (4.24) and (4.27) can be used to derive the following emission condition for the traveling wave model for g(z) = 1:

$$\left(\frac{w}{u}\right)^2 > \frac{2F_1^T\,(\beta_{\|}^{-1} \mp 1)}{(1 \pm x)\,\frac{dF_1^T}{dx} \pm F_1^T} \tag{4.29}$$

where $F_1^T = 2(1 \pm x)^{-2} \sin^2\left[\frac{q\pi}{2}(x \pm 1)\right]$

where the top sign corresponds to the forward wave. This differs with the condition for the standing wave model, Eq. (4.28). This difference is most obvious at x = -1 where Eq. (4.29) gives, for a forward wave, a higher w/u limit by a factor of $\sqrt{2}$. One thus concludes that modeling the RF field as a traveling wave is not correct.

4.3 Example of a 140 GHz Optical Gyrotron

In this section, a 140 GHz optical gyrotron will be designed, and the mode spectrum of this device will be generated. This gyrotron will be based on the $\bar{k} \| \bar{B}_o$ configuration, and as a result Eq. (4.27) can be used to calculate the starting currents. Before this can be done, however, the Q, frequency, and stored energy of each mode that can interact with the electron beam must be determined. In addition, Eq. (4.27) must be modified slightly in order to account for the fact that the beam will be annular rather than a pencil.

A confocal resonator [38] has been chosen because of its excellent transverse mode selectivity, and because the trapped radiation is concentrated near the axis, allowing for good mode-beam coupling. The frequency of this cavity can be written as

$$\omega = \left(\frac{\pi c}{L}\right)\left[q + \frac{1}{2}(1 + m + \ell)\right] \tag{4.30}$$

where L is the axial cavity length, q is the axial mode index, and m and ℓ are the transverse indices. The field structure, which in reality is a

complicated function of the spatial coordinates, will be represented by a TEM standing wave with planar wavefronts and a uniform g(z). The electric field amplitude can be written as

$$|\bar{E}_\perp| = E_o H_\ell\left(\sqrt{2}\,\frac{x}{r_o}\right) H_m\left(\sqrt{2}\,\frac{y}{r_o}\right) \exp\left[-\frac{x^2+y^2}{r_o^2}\right] \sin(kz)\, e^{-i\omega t} \tag{4.31}$$

where H is a Hermite polynomial and r_o is the spot size. For a confocal system, $r_o = \sqrt{cL/\omega}$. The stored energy can be calculated by integrating $|\bar{E}_\perp|^2$ over the cavity volume.

In order to completely specify this system, the mirror diameter, cavity length, and beam radius must be chosen. The optimum mirror diameter effectively confines the working mode (TEM_{00q}) but results in large diffraction losses for higher order modes. Eq. (4.27) indicates that, for fixed ω, I_{ST} is independent of L, and therefore in the linear theory the length is somewhat arbitrary. However, L should not be so large that "walkoff" losses [61] due to misalignment become severe. Finally, the beam radius should give good coupling with the working mode, and lower coupling with other modes. Based on these constraints, the following parameters were chosen: L = 19.82 mm (q = 18 for 140 GHz), R_e = 1.82 mm, and a mirror diameter of 10.92 mm.

The final step is the calculation of the coupling factors and Q's of the modes. A coupling factor must be introduced into Eq. (4.27) to account for the fact that the beam is annular. Based on Eq. (4.31), this factor can be expressed as

$$G(R_e) = \frac{1}{2\pi}\int_o^{2\pi} d\theta\, H_\ell^2\left(\sqrt{2}\,\frac{R_e\cos\theta}{r_o}\right) H_m^2\left(\sqrt{2}\,\frac{R_e\sin\theta}{r_o}\right) \exp\left(-\frac{R_e^2}{r_o^2}\right) \tag{4.32}$$

The total Q in this example has been approximated as the diffractive Q, $Q_D = -(2\pi L/\lambda)/\ln(\alpha_1\alpha_2)$, where α_j is the power reflection coefficient [52] at the j^{th} mirror. Ohmic losses have been assumed to be negligible. Based on the cavity dimensions selected above, the working mode TEM_{00q} will have a Q of 1450, while the next transverse mode, TEM_{01q} (or TEM_{10q}), will have a Q that is a factor of 8 smaller.

Figure 4.5 shows the anticipated mode spectrum around the TEM_{00-18} mode. Only the gain curves associated with the backward interaction (x>0) have been plotted. The two main branches of each q mode have been labeled. The velocity ratio w/u is equal to 2.3 at 68 kG and scales according to adiabatic theory as the magnetic field is varied. This explains the lower starting currents for TEM_{00-19}, since this mode only differs from TEM_{00-18} because it oscillates at a higher magnetic field, and as B_o increases the beam velocity ratio increases. A careful comparison of Figure 4.5 with Figure 4.3(b) indicates that a vast majority of the curves of the spectrum represent branches of a TEM_{00q} mode, and that higher order modes do not compete with the working mode, thus confirming the advantage of using confocal mirrors. This spectrum could be further thinned if axial mode selection techniques were employed. Figure 4.5 also suggests the possibility of operating this gyrotron as a tunable maser.

The major difficulty confronting this gyrotron is performance degradation due to velocity spread of the beam. Figure 3.2 indicates that when q = 1 the linear theory is insensitive to rather large velocity dispersions. However as q increases, the frequency spectrum as seen by an electron traveling down the cavity axis (obtained by a Fourier

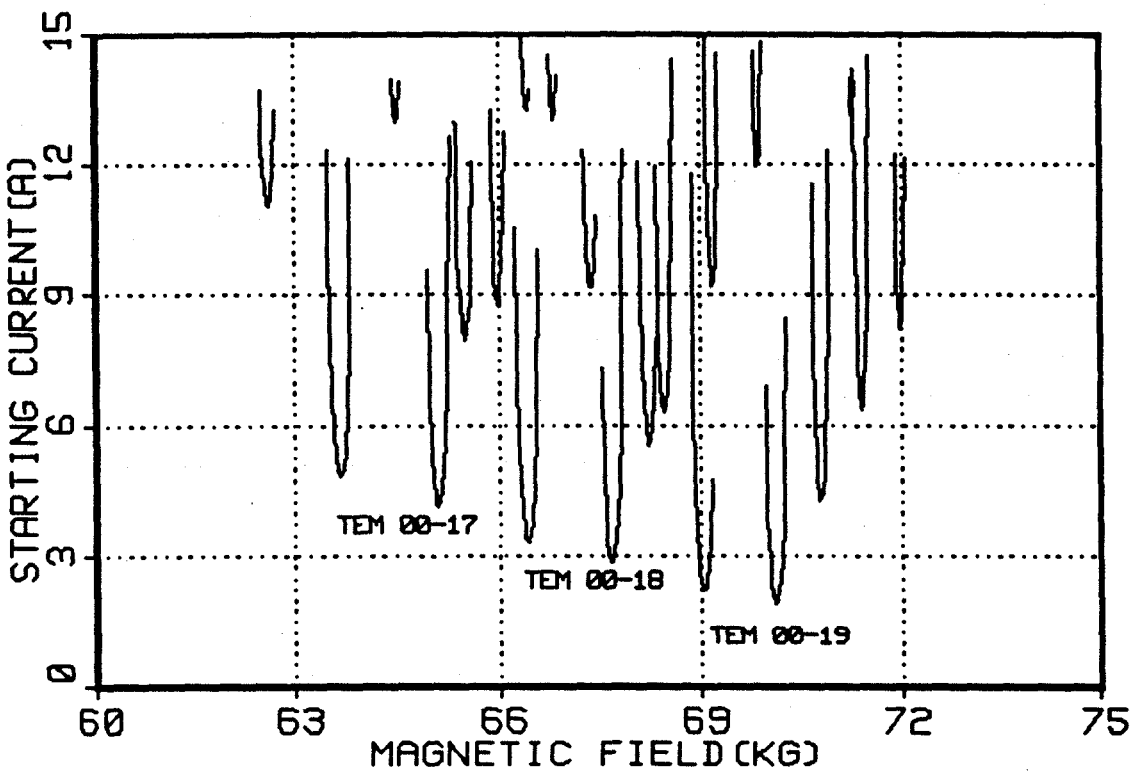

Figure 4.5: Mode Spectrum for 140 GHz Optical Gyrotron

analysis of the axial profile) becomes narrower, and the device becomes less tolerant to velocity variations that cause electrons not to be resonant with the field. The $\bar{k} \| \bar{B}_o$ configuration is much more susceptible to this problem than the $\bar{k} \perp \bar{B}_o$ arrangement since the electrons in the latter case effectively see a q = 1 Gaussian profile. A simple expression for the maximum spread that can be tolerated is obtained by limiting the dispersion of x to the width of the gain functions, which is approximately 2/q. Since for fixed energy $\Delta x/x = \Delta u/u$, the following limits for the velocity halfwidths are quickly acquired:

$$\left(\frac{\Delta u}{u}\right) \lesssim \left|\frac{1}{qx}\right|$$
$$\left(\frac{\Delta w}{w}\right) \lesssim \left(\frac{u}{w}\right)^2 \left|\frac{1}{qx}\right| \qquad (4.33)$$

where the second equation is derived via energy conservation. For our q = 18 device with $x \tilde{=} 1$, the upper limit on the perpendicular spread is 1% according to these equations. This is in good agreement with Figure 4.6, where the starting currents for the two main branches of the TEM_{00-18} mode are shown for various velocity spreads. These curves were calculated by assuming a Maxwellian electron velocity distribution and doing the integration of Eq. (4.21) numerically. Unfortunately, perpendicular velocity spreads of less than 1% are well below what is presently feasible with magnetron injection guns, although future technical improvements may make such low dispersions a reality. Other complications that might also affect the performance of this device include the reflection of diffracted radiation, especially higher order modes, back into the cavity region, and the lowering of the

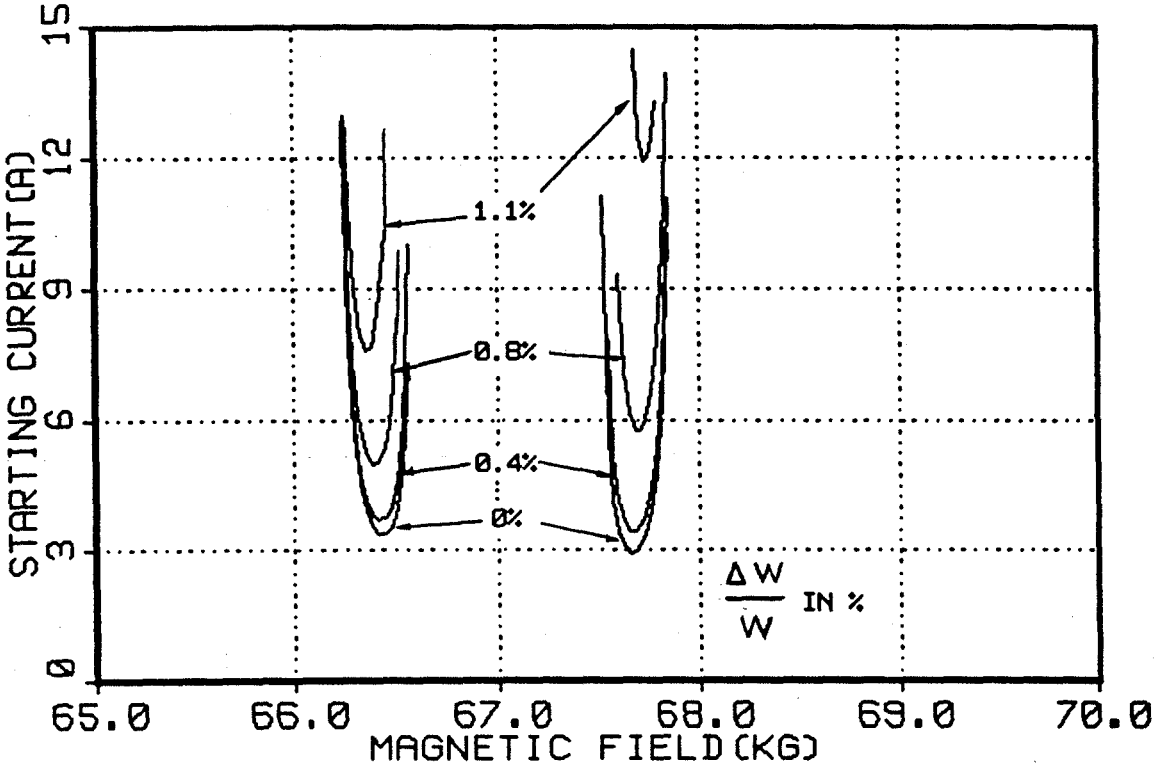

Figure 4.6: Effect of Velocity Spread on Two Main Branches of TEM_{00-18}

working mode Q due to output coupling through one of the mirrors that could aggravate the mode competition problem.

4.4 Conclusions

In this chapter, the linear theory of an optical gyrotron was derived. This derivation was kept general in order that the results would be applicable to any beam-field configuration and field profile. This general approach also allowed all possible interaction mechanisms involving the electric and magnetic field components to be uncovered. These mechanisms were discussed in detail in Section 4.2, and related to four gain functions that mathematically describe the particle-field coherence characteristics.

The linear theory was derived for both a standing and a traveling wave representation of the cavity field. This was done in order to determine if modeling the field as a traveling wave, as a number of previous authors have done, is valid. A comparison of these two theories indicate that even for large q they give different results. Therefore, a standing wave must always be used to describe an oscillator's RF field.

Two beam-field configurations were investigated in detail: $\bar{k}$ perpendicular to the electron beam, and parallel to the beam. The former case is of interest only when $\bar{E}$ is perpendicular to the beam, which gives a pure ECM interaction with no magnetic contribution. In this situation the results of Chapter 3 are applicable. In the latter case, both electric and magnetic mechanisms are present but tend to offset one another. This results in rather high, but feasible, starting currents. A further difficulty is performance

degradation due to beam velocity spread. An optical gyrotron operating at 140 GHz in a TEM_{00-18} mode was designed which exhibited good mode separation properties but required a perpendicular velocity dispersion of less than 1%. Very high quality electron beams are currently under development for use in slow wave gyrotron amplifiers, where similar degradation due to beam velocity spread is found. If electron guns can be constructed for that application, they would also have application to optical gyrotron oscillators in the axial configuration. It may also be possible to use this sensitivity of the TEM mode to velocity spreads as a diagnostic in order to determine the quality of the electron beam.

Chapter 5

Design Study of an Electron Cyclotron Resonance Heating System

In this chapter, an ECR heating system is presented that is designed to heat a commercial tokamak to ignition. This study includes a parametric analysis of a gyrotron that conforms to the physics constraints discussed in Chapter 2 as well as the design of the accompanying transmission system and port. This analysis is based on a conservative extrapolation of presently available technology, and has led to the identification of major technological problems that require a vigorous research and development program as well as their possible solutions. By determining the basic design features of an ECRH system as well as the technological barriers, such a study serves as a useful aid in selecting the most promising path leading to the utilization of ECRH to heat a commercial, power-producing tokamak.

In a parametric analysis, all the performance characteristics and the complex interrelations among the parameters describing the gyrotron system are modelled in a self-consistent computer code. This algorithm should be kept simple enough that an intuitive understanding of the physical processes involved is possible, yet be sufficiently realistic that the important variables of the system are accurately modelled. Studies can then be performed to determine the sensitivity of the operational characteristics of the gyrotron to variations of its design variables. Tradeoff studies can be conducted to eliminate design options technically not feasible, to explore more promising

designs, and to point out the critical technological problems that must be more fully addressed in the future. Such an analysis allows one to determine the most promising design options as well as the regime of operation that is consistent with realistic engineering constraints. Parametric models can also be used to identify attractive new design points that can subsequently be investigated in greater detail, as well as quickly determine the implications of proposed design changes.

In this analysis a number of important questions will be addressed:

(i) What are the major design parameters of an ECM and how are they interrelated?

(ii) How do the technological and physical constraints limit the the parametric space in which an ECM can operate?

(iii) What are the characteristics of an optimized design, and what procedure can be followed to determine the associated device parameters?

(iv) What are the characteristics of the auxiliary systems?

(v) What are the problems associated with operating at high power and high frequency?

Question (i) is covered in Appendix C, where a detailed description of the gyrotron model used in this investigation is presented. Questions (ii) and (iii) are addressed in the first section. The major constraints imposed by physics and technology are discussed, an optimization procedure is outlined, and the operating regime available to a gyrotron is established. Section 2 is concerned with question (iv) and the various methods available for transmitting

the RF power to the plasma. Finally, the concluding section reviews the major problems and outlines possible directions for further design study work.

5.1 Design of the Gyrotron

The model used in this analysis of high power, high frequency gyrotrons is based to a large extent on an earlier design study [62] of a 10 kW, 200 GHz gyrotron and is described in detail in Appendix C. The appropriate alterations have been introduced into the 10 kW study so that it can be applied to gyrotrons with output powers of hundreds of kilowatts. We will begin by discussing the basic assumptions and constants of the model.

It will be assumed that the gyrotron is operating in a steady state, and that all parameters are independent of time. The gyromonotron, a special version of the gyrotron with a single, axisymmetric resonant cavity will serve as a model for the device. Another ECM device, for example the gyroklystron, may eventually emerge as the optimum device for tokamak plasma heating. However, at the present time the gyromonotron, hereafter to be referred to as simply the gyrotron, is the most widely investigated form of ECM, and also the most powerful source of millimeter and sub-millimeter radiation.

The gyrotron will be operated at the fundamental, that is, $\omega \simeq \omega_c$. Operation at the second harmonic, $\omega \simeq 2\omega_c$, would at first seem more attractive as a result of the reduced magnetic field requirements in the cavity. However, analysis shows that $2\omega_c$ operation is less efficient than ω_c for the present design. This conclusion is based on the nonlinear theory of Nusinovich and Erm [63], which

indicates that the overall efficiency, η_T, of a gyrotron operating at $2\omega_c$ is substantially lower than for a fundamental gyrotron because of the low transverse efficiency, $\eta_\perp$ (see discussion of efficiency in Appendix C). Although $\eta_\perp$ can be improved for $\omega = 2\omega_c$ operation by increasing the Q of the resonator, this gain is offset by the increased power loss due to ohmic heating of the cavity walls, so that high total efficiency cannot be achieved. One can also improve $\eta_\perp$ for $2\omega_c$ operation by increasing the beam current. However, the maximum current is limited by physical constraints of the electron gun, and unless the gun technology is improved, and it may prove impossible to operate at the high currents needed to achieve the optimum values of $\eta_\perp$. Another potential problem with $2\omega_c$ operation is parasitic modes, including modes which oscillate at ω_c.

In order to simplify the analysis, the frequency and power of the gyrotron have been fixed. A frequency of 200 GHz has been selected on the basis of the set of constraints imposed by the propagation and absorption of electron cyclotron radiation in the tokamak plasma. The main conclusion reached in Chapter 2 was that the need for high density operation (peak density $\simeq 4 \times 10^{14}$ cm^{-3}) in moderate size tokamak reactors is likely to lead to the requirement of frequencies in the vicinity of 200 GHz.

The power level of the gyrotron was fixed at 100 kW, which represents a compromise value between two conflicting requirements. On the one hand, there is an advantage in achieving high power levels per unit in order to reduce the number of units and therefore to minimize costs. It has been estimated that operating with more than one thousand gyrotron units will significantly increase the cost. Since

about 100 MW of auxiliary power will be needed to reach ignition according to the HFCTR design study [20], this implies each gyrotron must deliver at least 100 kW. On the other hand, 100 kW is a significant extension beyond present gyrotron technology, and projections to even higher power levels may prove unreliable. Fig. 1.2 shows the current state of the art of gyrotrons. Based on this data, one can project that a CW device could currently be built to deliver 10 kW at ν = 200 GHz. Although this indicates that the choice of P = 100 kW is well beyond the currently available technology, it is in line with the developmental progress now being anticipated in gyrotron research. As will be shown later, the choice of P = 100 kW is also consistent with limits imposed by the ohmic heating of the cavity walls and the need to operate in low modes in order to reduce mode competition. It should be noted that P = 100 kW is a representative value, and that the optimum power level may vary about this value.

Another factor which is important in selecting the power level of each gyrotron is the window transmission problem. Although it is not yet certain that a suitable window material can be found for even a 100 kW power level, the window problem is much more severe at high power levels. It appears likely that, if a 1 MW gyrotron at 200 GHz could be constructed, its output would have to be divided up prior to a window in order to obtain transmission. Such a division of power is a difficult problem and could negate the advantage of achieving high power from a single unit. Windowless operation might be possible, but it is very unattractive because of the additional requirements of vacuum pumping and the danger of gas leaks into the gyrotron.

The gyrotron may be divided into two major subsystems, the electron gun and the cavity, which are physically distinct units. However, the analysis of these two subsystems is not independent, and as a result a self-consistent model is required. Fig. 5.1 shows the overall structure of this model, which has been codified as a PDP-11 Fortran program. The major components have been related to the six major variables of the design: the cavity radius R_o and length L, the electron beam's parallel and perpendicular velocities, $\beta_{||}$ and $\beta_{\perp}$ ($\beta \equiv v/c$), the beam current I and beam radius R_e. The wave equation relates R_o and L to the frequency of operation as well as to the transverse mode index ν_{mp}. The cavity radius and length, in conjunction with the wall temperature T_w, also determine the ohmic and diffractive Q's of the system, Q_{OHM} and Q_D. The cavity Q's can in turn be used to calculate the heat flux in the cavity walls due to ohmic currents P_w. The total efficiency of the device η_T can be calculated in two ways. First, it can be related to the beam energy U and current I, $\eta_T = P/UI$. Secondly, it can be derived from its three components, η_Q, η_{el}, and $\eta_{\perp}$. The main function of the code is to vary the appropriate parameters to obtain a solution in which both definitions of η_T are in agreement. Also included in the algorithm depicted in Fig. 5.1 are limits imposed by mode competition as well as constraints on the beam voltage and current due to physical limits of the electron gun.

5.1.1 Parametric Analysis

In this section, a parametric analysis based on the gyrotron model of Appendix C will be outlined. The figure of merit for this study was chosen to be the total efficiency, η_T. High efficiency is

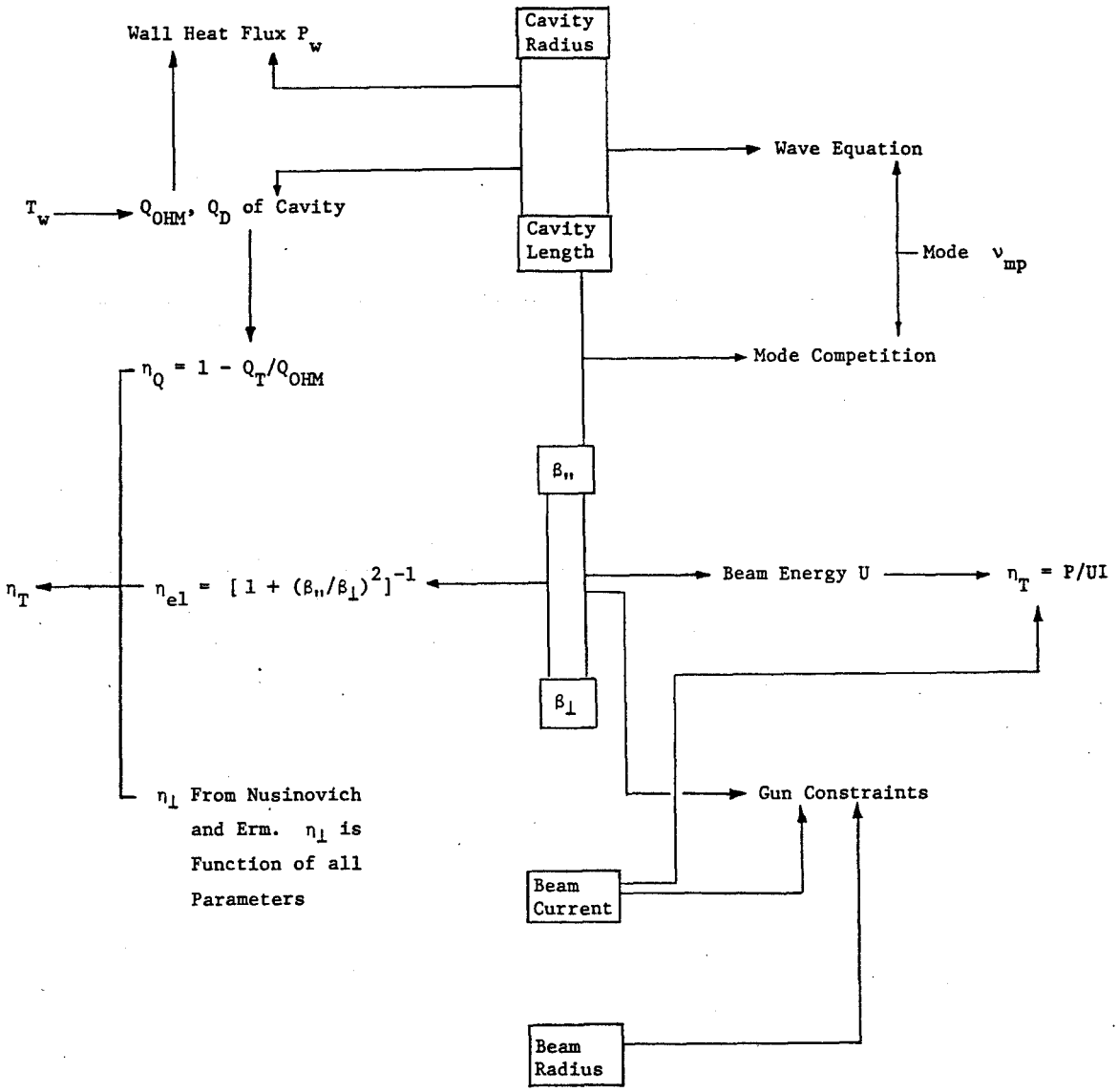

Fig. 5.1 Design Constraints of Gyrotron Frequency and Output Power Fixed

important for gyrotrons for several reasons. First, it reduces the power supply requirements, which can significantly lower the cost of ECRH power. Second, it reduces the required beam power, which prolongs the collector life and lowers the collector cooling needs. Finally, it reduces the ohmic heating losses in the cavity and helps increase the cavity lifetime.

In order to better understand how the total efficiency of the gyrotron is related to the design parameters, η_T has been plotted as a function of a variety of these parameters. These results are shown in Figs. 5.2 through 5.5. In all of these graphs, the length L is allowed to vary in order to find the highest overall efficiency that can be achieved. Except where indicated, the following parameters have been assumed: ν = 200 GHz, U = 70 kV, I = 4.1A, mode TE_{051}, R_e = 2.07 mm (third radial maximum from cavity center), and $\beta_\perp/\beta_\parallel$ = 1.8.

Figure 5.2 shows the effect on η_T of varying the operating frequency of the device. As the frequency is increased, the maximum efficiency will occur at shorter lengths. This is consistent with the calculations of Nusinovich and Erm (Fig. C.1) in which both I_o and μ, and therefore η_T,, can be treated as functions of L/λ, which can be rewritten as $L\omega$. If $Q_D << Q_{OHM}$, then η_T virtually becomes a function of $L\omega$. Fig. 5.2 illustrates that this dependence on $L\omega$ is approximately correct, although slightly higher total efficiencies can be obtained at lower frequencies. This dependence allows one to scale η_T to other frequencies by keeping $L\omega$ constant.

In Fig. 5.3 the beam voltage is varied from 40 kV to 90 kV. One can observe that operating at too high a voltage can cause a

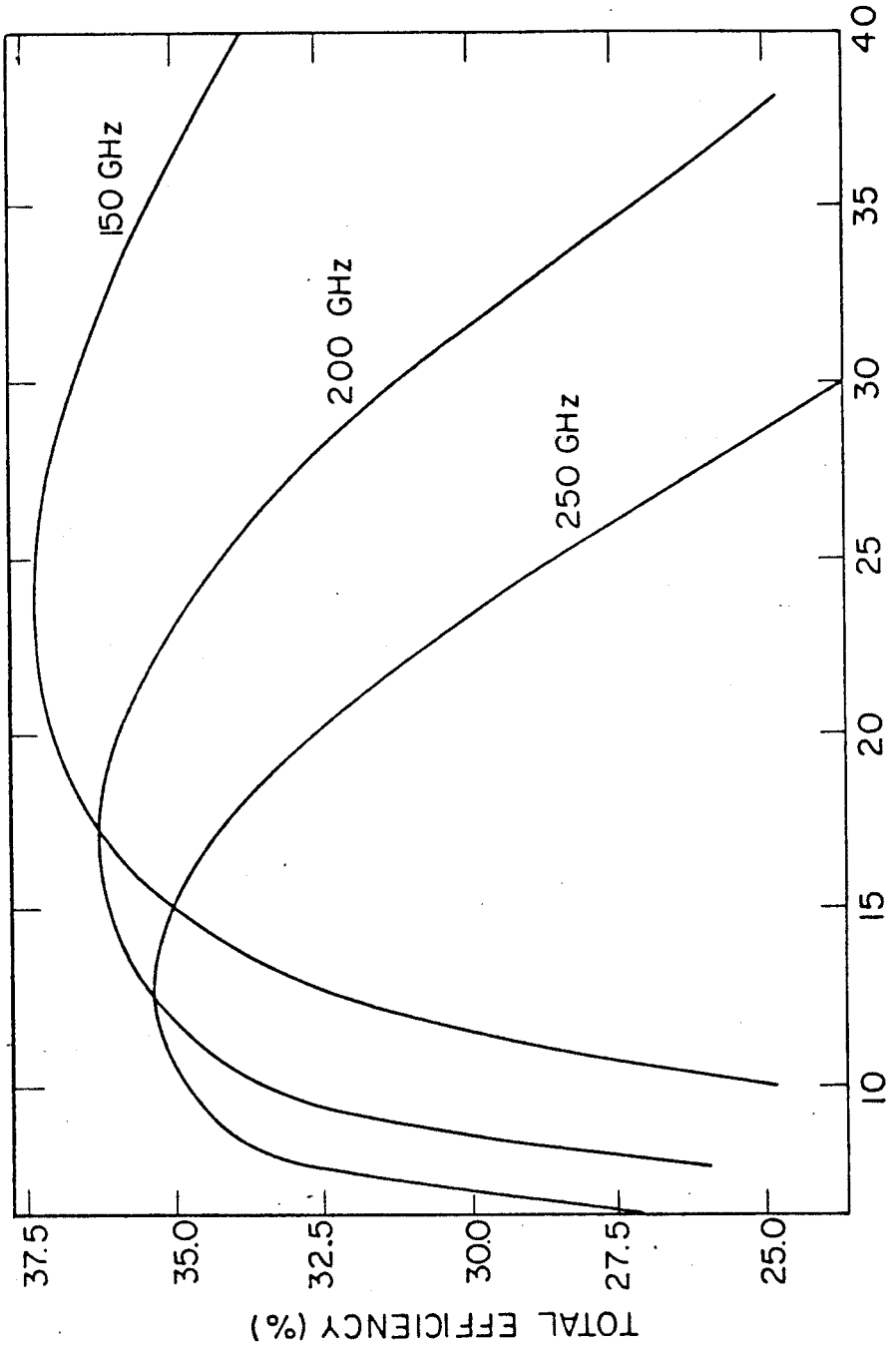

Fig. 5.2 Total Gyrotron Efficiency vs. Frequency and Cavity Length.

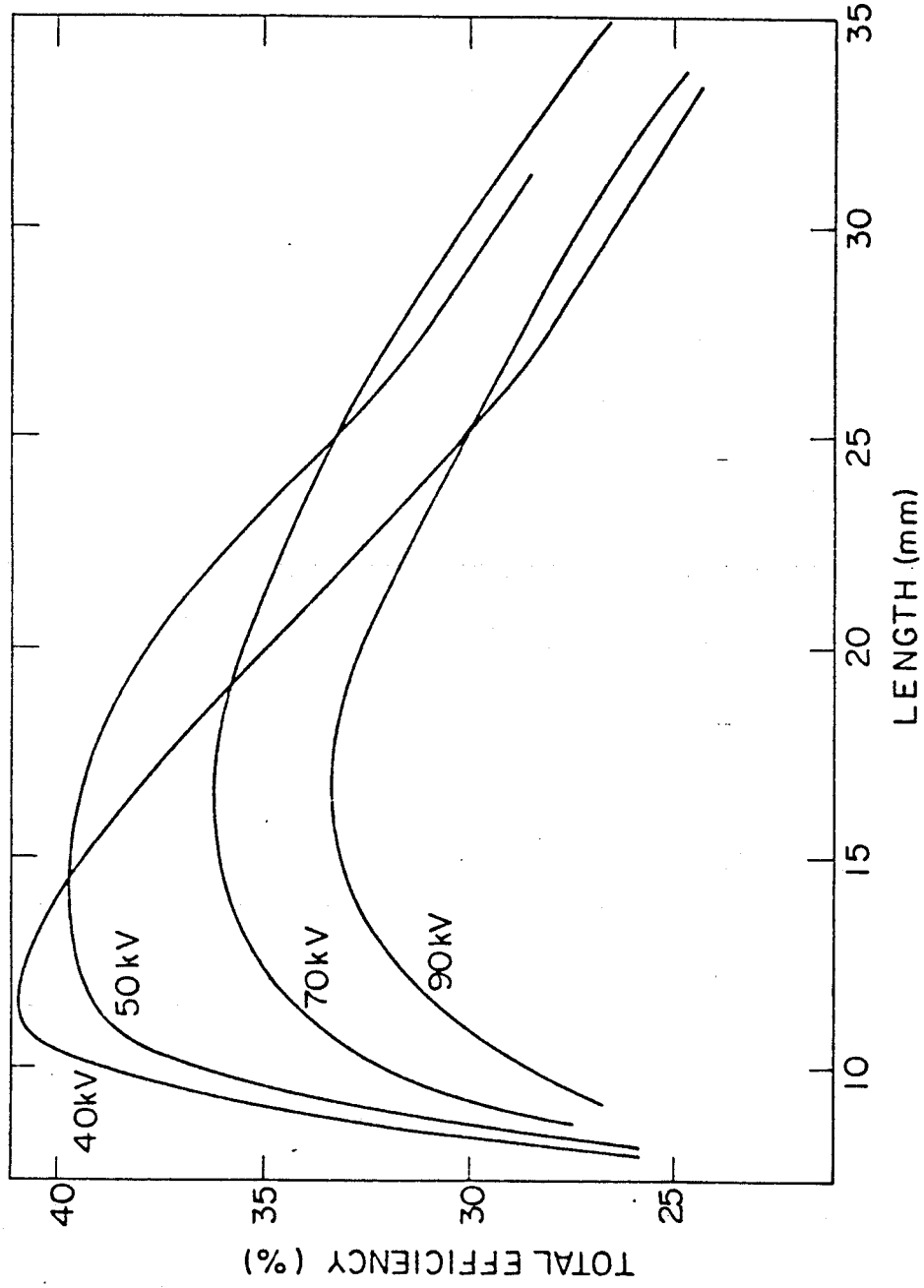

Fig. 5.3 Total Gyrotron Efficiency vs. Beam Voltage and Cavity Length.

reduction in total efficiency. This is due to the fact that as U is increased, the length must be increased to achieve the optimum η_T, but this causes η_Q and subsequently the maximum η_T to be reduced. Calculations indicate that for $\beta_\perp/\beta_\parallel = 1.8$, the beam voltage should be between 40 and 60 kV to achieve the highest total efficiencies.

The effect of varying the beta ratio is shown in Fig. 5.4. As one can see, the total efficiency is very sensitive to this ratio. In order to achieve the highest η_T, the gyrotron should operate at as high a value of $(\beta_\perp/\beta_\parallel)$ as possible. However, as this ratio is increased, the velocity spread of the beam becomes more problematic [64] and can eventually cause a reduction in the efficiency of the device [see Eq. (C.28)]. Results in Fig. 5.4 do not include this decrease of η_T caused by the velocity spread. One should thus select a beta ratio that balances these two opposing influences.

Finally, Fig. 5.5 shows how the K factor in Q_D (see Eq. (C.9)) influences the total efficiency. This factor can be interpreted as a measure of RF field trapping by the resonator. The higher K is, the more effectively the cavity traps the field. The graph indicates that the optimum length, as well as the width of the curve, is strongly dependent on K. This suggests a possible procedure for optimizing a gyrotron design. Once the operating mode is selected, a length can be chosen that corresponds to a tolerable heat flux P_w. Then K can be varied until the peak of the efficiency curve occurs at this length. This value of K can then be obtained by selecting the appropriate cavity shape and output coupling.

The effect of the constraints imposed by the magnetron gun on the operating regime of the gyrotron will now be investigated. In

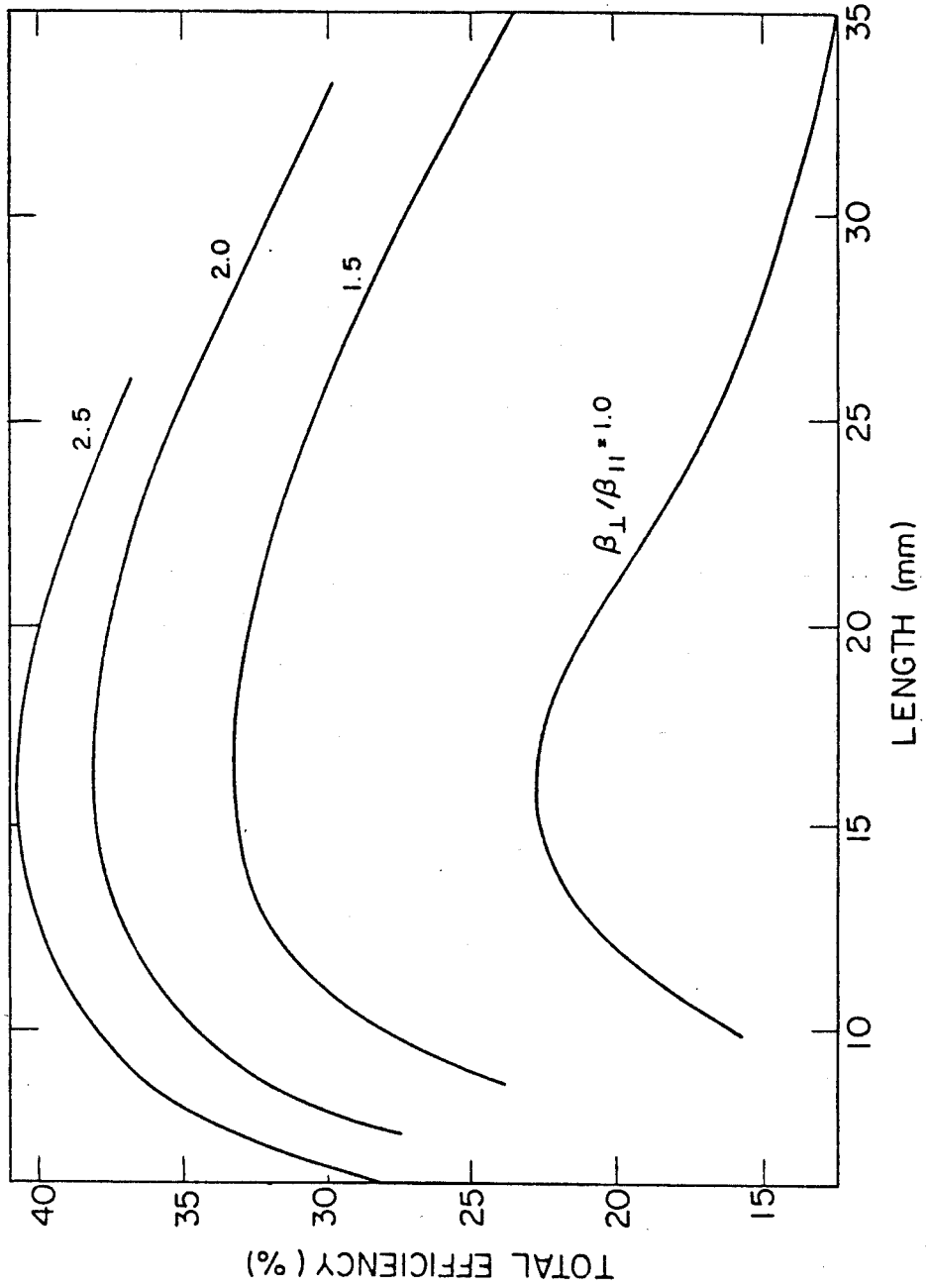

Fig. 5.4 Total Gyrotron Efficiency vs. Velocity Ratio and Cavity Length.

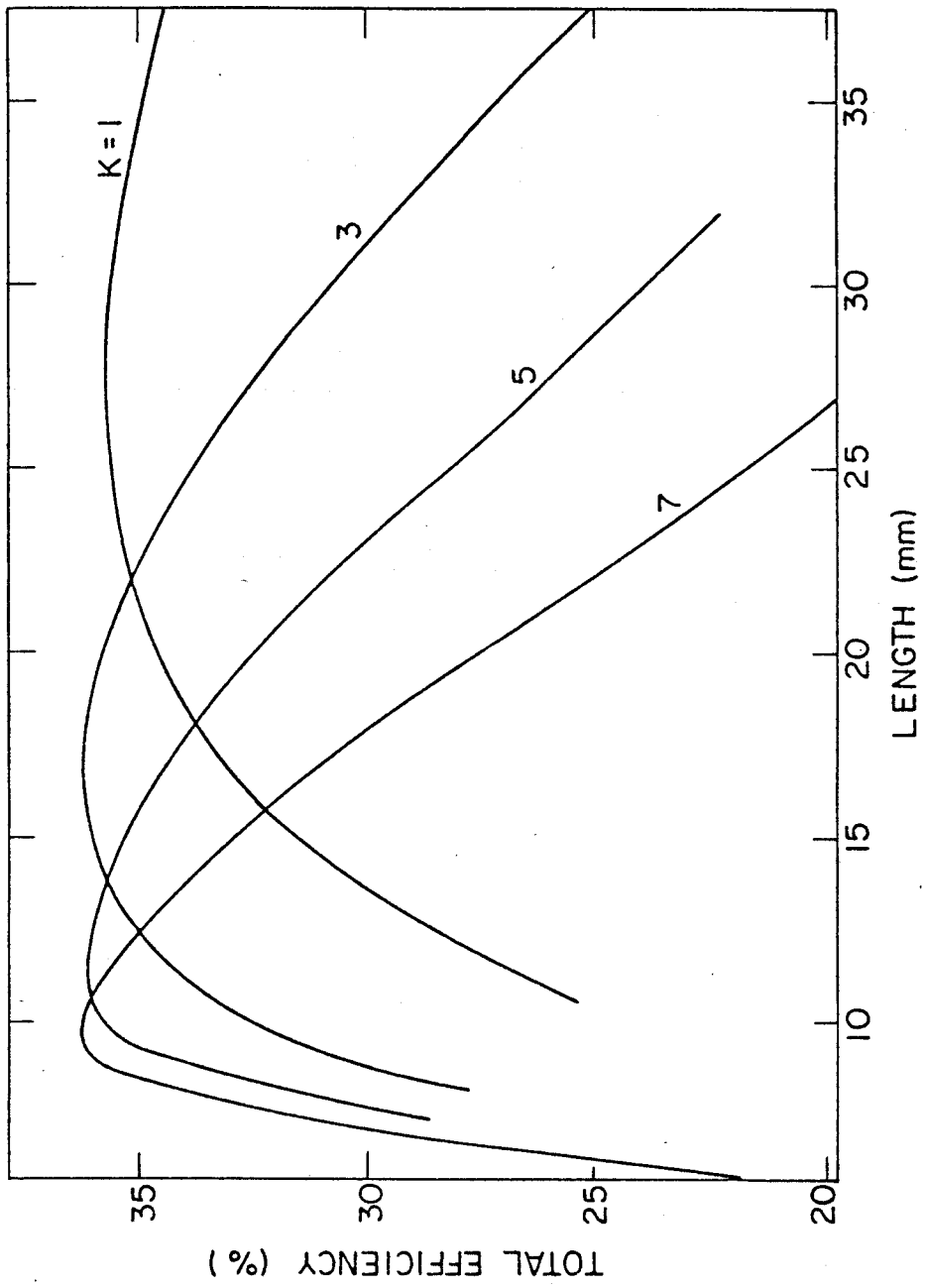

Fig. 5.5 Total Gyrotron Efficiency vs. the Coupling Factor K and Cavity Length.

Appendix C a model for the gun was described in which an upper limit was placed on the current (see Eq.(C.29) through Eq.(C.31)). This limit on the beam current is illustrated in Figs. 5.6 and 5.7. Except where indicated, the following parameters have been assumed: ν = 200 GHz, U = 70 kV, mode TE_{051}, R_e = 2.82 mm (fourth radial maximum from center), and $\beta_\perp/\beta_\parallel$ = 1.8.

Fig. 5.6 shows the effect of changing the maximum velocity spread of the beam. The characteristics of the operating regime are very sensitive to the choice of ε_{max} when this variable becomes sufficiently small. As ε_{max} is decreased, the limit imposed by Eq. (C.29) becomes more restrictive, forcing the gyrotron to operate at higher beam energies and lower currents. The increase in beam energy is beneficial because this causes the velocity spread due to surface roughness and thermal effects to be reduced. As ε_{max} is increased, the maximum current becomes limited by the beam to cavity voltage drop restriction (Eq. (C.31)) rather than by the velocity spread criterion. This can be seen for ε_{max} = 12%.

In Fig. 5.7, the radial maximum of the RF field involved in the interaction with the electron beam is varied. The gyrotron is operating in the TE_{051} mode with ε_{max} = 10%. This graph indicates that it is advantageous for the beam to be as close to the cavity wall as possible in order to increase the current limit. However, one must avoid operating with the beam too close to the wall in order to prevent additional wall heating due to electron bombardment. As in the previous figure, two different limits on the current can be observed. For interactions involving the third and fourth maxima, the current is limited by the cavity-beam voltage, while for the

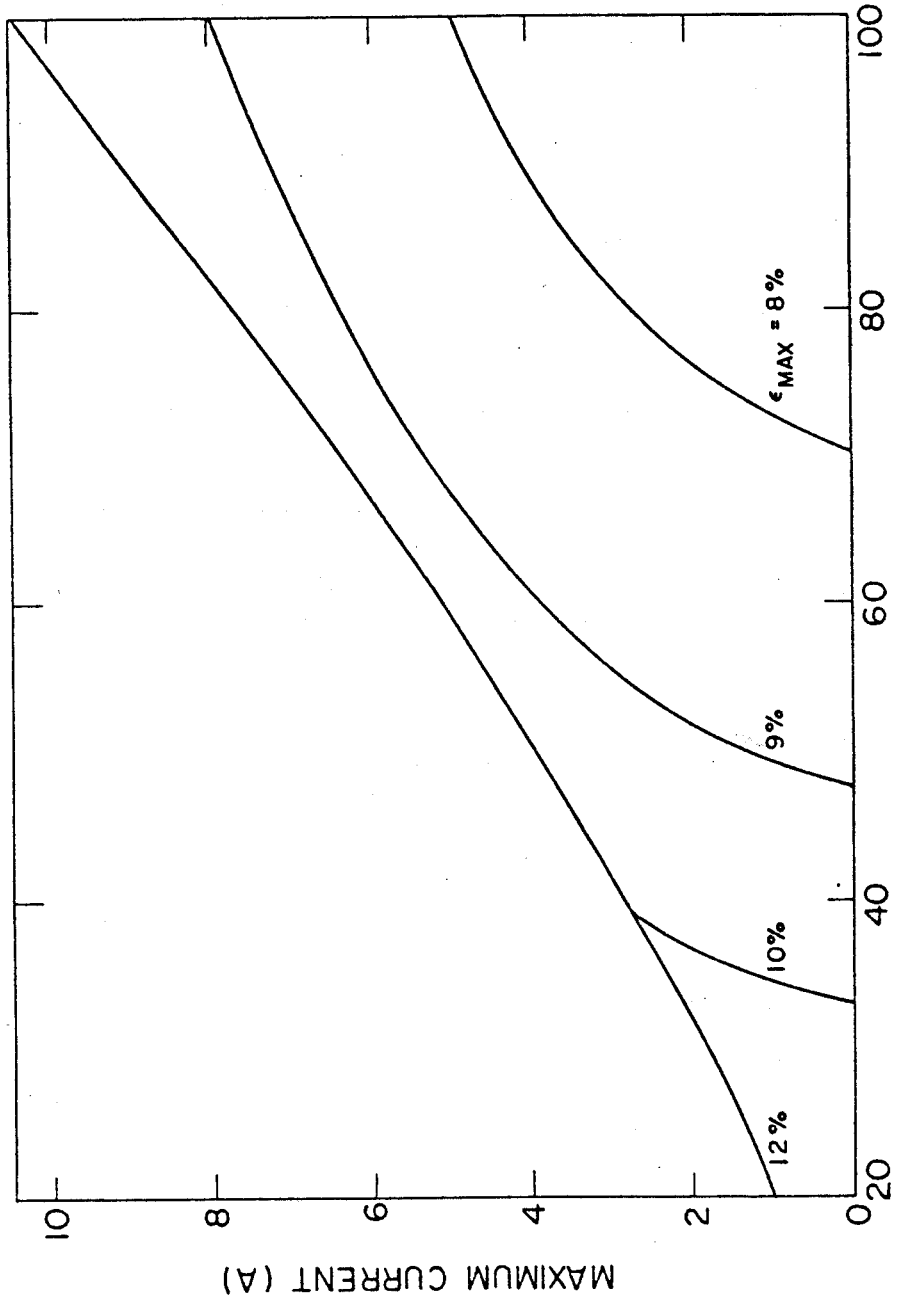

Fig. 5.6 Maximum Current Based on Gun Constraints vs. Beam Energy and Maximum Transverse Velocity Spread.

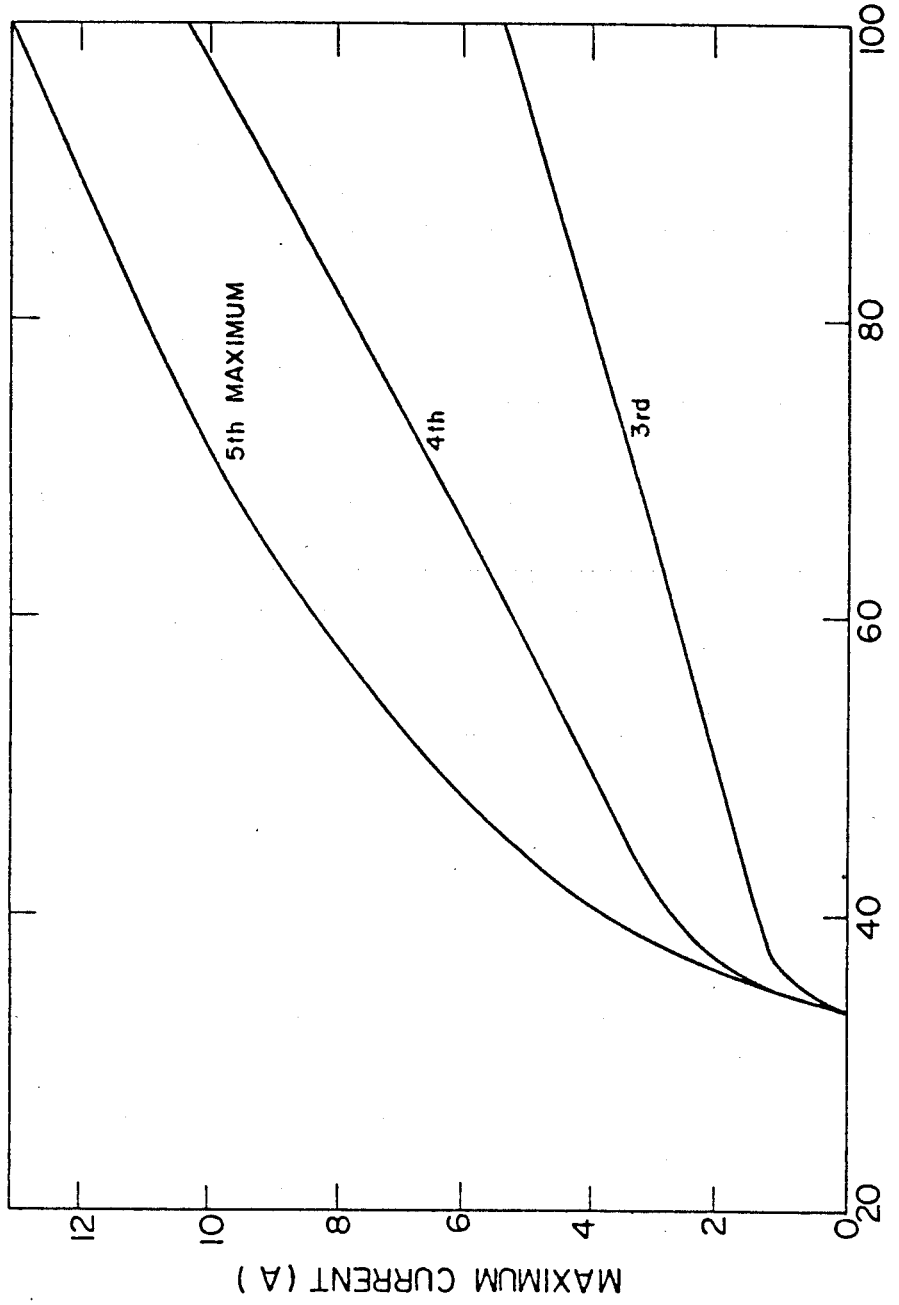

Fig. 5.7 Dependence of Maximum Current on Radial Position of Electron Beam. Curves Correspond to Radial Peaks of RF Field as Measured From Axis.

fifth maximum the beam velocity spread sets this limit.

Using the results of Fig. 5.7 to choose the beam radius, and restricting R_e to less than 0.85 R_o, the effect of varying the operating mode was investigated. It was found that the limit on the current becomes less restricitve as the p index of the TE_{0p1} mode is increased, suggesting higher modes might prove advantageous since they provide a larger operating regime. However, this finding must be tempered by the fact that mode competition becomes more severe as the gyrotron operates in higher modes.

During the course of this parametric analysis, a number of trade-offs involving major design parameters were found. These trade-offs are important because they influence the procedure used for choosing these parameters. In the case of the beta ratio, $\beta_\perp/\beta_\parallel$, this involves the opposing requirements resulting from the desire for high efficiency and the need to limit the beam velocity spread. Increasing $\beta_\perp/\beta_\parallel$ enhances η_T but makes Eq. (C.28) more difficult to satisfy. In choosing ν_{mp}, one must balance the need for a low wall heat flux with the need to minimize mode competition. As one operates in higher modes and ν_{mp} increases, P_w is reduced but the problem of competing modes becomes more severe. The choice of length often involves the conflicting needs of operating at the highest efficiency possible (see Fig. 5.2) and keeping P_w at a reasonable level. Finally, as indicated in the discussion of the gun constraint, a large beam radius causes the limit on the current to be less severe but reduces the strength of the interaction between the RF field and beam. These trade-offs must be balanced in the process of selecting the design parameters.

The procedure followed in selecting the reference design parameters will now be outlined. As mentioned before, the power output P has been fixed at 100 kW and the frequency ν at 200 GHz. The factor K in Q_D is also treated as a constant, and based on the selected cavity shape is given a value of 3 [31]. The electron beam is assumed to pass as close to the cavity wall as possible in order to ease the gun constraints. We begin by selecting the maximum beam velocity spread that can be tolerated. The discussion in conjunction with Eq. (C.29) indicated that a small ε_{max} is desirable because this allows a high beta ratio and thus a high total efficiency. However, Fig. (5.6) shows that if ε_{max} becomes too small, then the available operating regime can become severely limited. In order to avoid a restricted operating regime, a maximum velocity spread of 10% was chosen. This leads, via Eq. (C.29), to a beta ratio $\beta_\perp/\beta_\parallel$ within the range 1.8 - 2.2. A conservative ratio of 1.8 has been chosen.

The beam current can now be determined by varying I until the two methods of calculating η_T given in Fig. 5.1 have a common solution. This was done for beam voltages satisfying the constraints imposed by the gun. As is indicated in Fig. 5.3, the gyrotron should in general be operated at a lower voltage in order to achieve the highest η_T. The results are shown in Figs. 5.8 and 5.9. In Fig. 5.8 the total efficiency has been plotted as a function of cavity radius and length, while Fig. 5.9 shows the corresponding value of I. The beam voltage can be calculated from these two graphs by using the equation $U(kV) = 100/\eta_T\, I(A)$. Note that, since ν is fixed, only certain cavity radii represent actual operating points. These

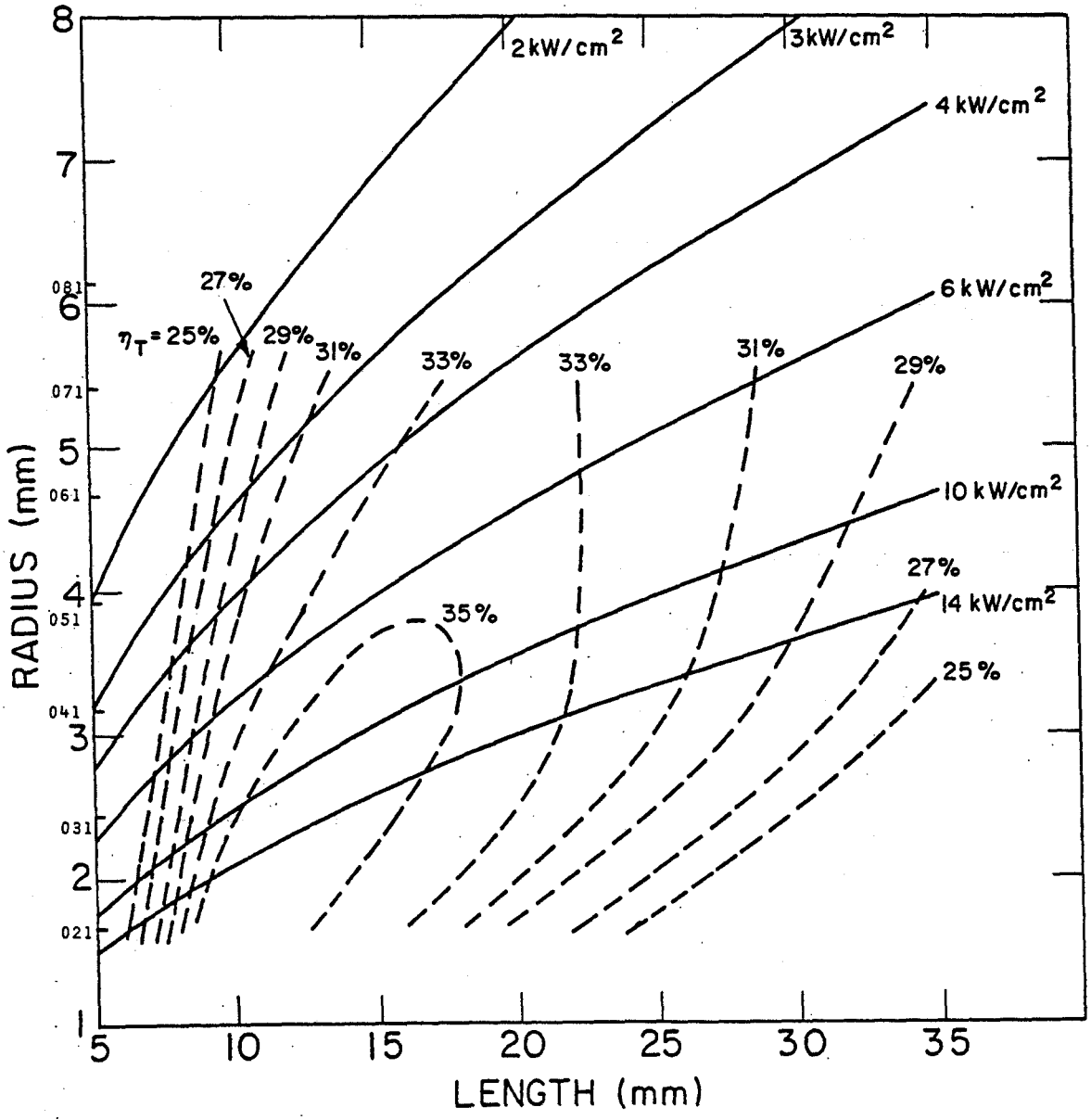

Fig. 5.8 Optimum Total Efficiency of 200 GHz, 100 kW Gyrotron with $\beta_\perp/\beta_\parallel = 1.8$.

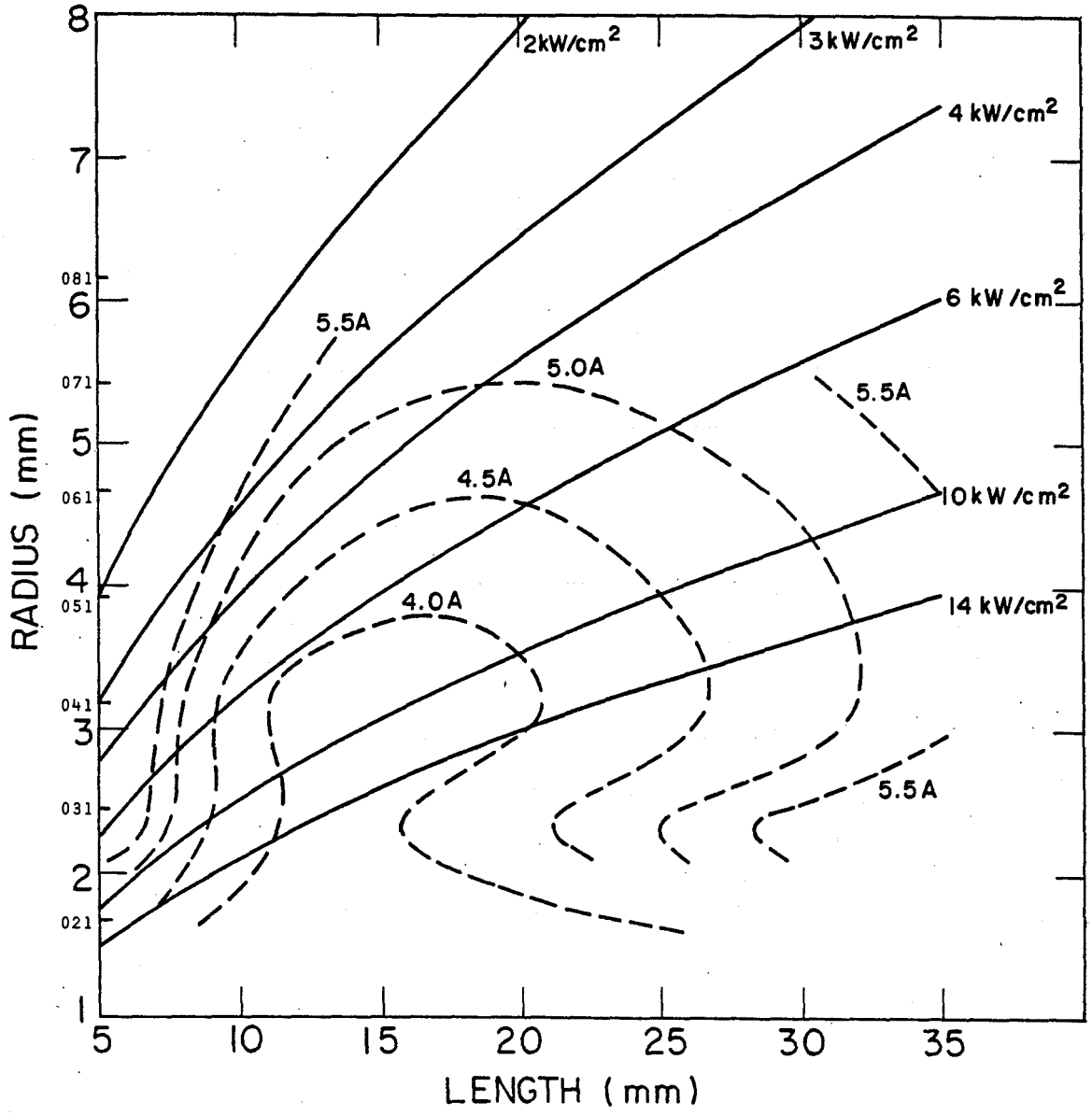

Fig. 5.9 Beam Currents Associated with Operating Conditions Shown in Fig. 5.8

points are indicated by the indices of the TE_{opl} mode along the vertical axis. Also shown in these graphs is the heat flux P_w, which has been calculated using Eq. (C.24).

In order to choose a reference design point, a reasonable value for P_w must be determined. Based on an analysis of cavity cooling that was done for this design study [65], heat fluxes less than 5 kW/cm^2 appear manageable. The heat flux can be reduced by either increasing the cavity radius (i.e., moving to higher modes), or decreasing the length which results in greater output coupling.

Mode competition constraints must also be considered. The mode separation condition, Eq. (3.38), can be rewritten in a simpler form when determining whether the TE_{opl} and TE_{2pl} modes overlap. Note that, for gyrotrons operating near cutoff, the first term of Eq. (3.38) is small compared to the second and can be neglected. Using the fact that $\Delta\nu_{mp}$ scales approximately as $1/R_o$ for the TE_{opl} and TE_{2pl} modes, (this is accurate to within 3% for $3 \leq p \leq 7$) the separation condition becomes:

$$0.116 \gtrsim \beta_{\parallel} \lambda \frac{R_o}{L} \tag{5.1}$$

where all lengths are in millimeters. This inequality scales with respect to R_o and L in the same manner as P_w. Thus, any attempt to reduce the wall heat flux by varying the length or radius will automatically cause the competition between the TE_{opl} and TE_{2pl} modes to becomes more severe. Calculations show that for $\beta_{\parallel} = 0.4$, Eq. (5.1) will not be satisfied until $P_w > 32$ kW/cm^2, which is well above the 5 kW/cm^2 limit mentioned earlier. It is therefore impossible to

simultaneously avoid mode overlap and keep P_w at a reasonable level. In order to alleviate the mode competition problem, it will be necessary to operate at the highest possible P_w and to use mode suppression techniques. It is possible that these techniques, or the appearance of spurious modes, might lead to a reduction of the overall efficiency of the gyrotron as calculated for single modes by Nusinovich and Erm.

For $P_w = 5$ kW/cm^2, modes TE_{051} through TE_{071} provide high total efficiency and can be used as operating points. In order to minimize the number of possible spurious modes by keeping the cavity size as small as possible, TE_{051} has been chosen as the reference design mode. This gives $R_o = 3.94$ mm and, based on the above value of P_w, L = 12.5 mm. The overall efficiency at this operating point is 33%. The beam voltage is 70 kV, and the beam current is 4.3 A. All other design parameters can be calculated using the equations of Appendix C and are given in Table 5.1. Note that, since $\varepsilon_{TOTAL} < \varepsilon_{max} = 10\%$, $J_k < J_k^{max} = 4$ A/cm^2 and the beam-wall voltage drop $\Delta U/U = 0.53\% < 1\%$, the current is well within the limits imposed by the gun. This reference design is characterized by a very low J_k which ensures that the cathode will have a long lifetime.

If the limits imposed by the gun and wall heat flux could be circumvented, then the power output of this device could be increased dramatically by increasing the current. This is shown in Fig. 5.10 where P and η_T have been plotted as functions of I. This figure illustrates that, in general, the output power and total efficiency do not peak at the same operating point. If a wall cooling of $P_w = 10$ kW/cm^2 could be obtained, then the gyrotron could achieve P = 200 kW with

TABLE 5.1

200 GHz Gyrotron Parameters

$\nu = 200$ GHz	$\omega = 1.257 \times 10^{12}\ 5^{-1}$
$\lambda = 1.5$ mm	$B_o = 75$ kG
$I = 4.35$ A	$r_g = 0.1$ mm
$U = 70$ kV	$\alpha = 21.8$
TE_{051} mode	$B_k = 3.44$ kG
$\nu_{05} = 16.47$	$R_k = 13.17$ mm
$R_o = 3.94$ mm	$E_{\perp k} = 1 \times 10^5$ v/cm
$R_e = 2.82$ mm	$J_k = 1.88$ A/cm^2
$\Lambda = 0.8$	$V_a = 21$ kV
$Q_{OHM} = 16{,}744$	$\varepsilon_{sc} = 3.3\%$
$K = 3$	$\varepsilon_T = 1.3\%$
$Q_D = 2618$	$\varepsilon_a = 7.9\%$
$L = 12.5$ mm	$\varepsilon_{TOTAL} = 8.66\%$
$\gamma = 1.137$	$\Delta U/U = 0.53\%$
$\beta = 0.476$	$Q_T = 2264$
$\beta_\perp/\beta_\parallel = 1.8$	$\eta_\perp = 0.50$
$\beta_\perp = 0.416$	$\eta_T = 0.328$
$\beta_\parallel = 0.231$	$P = 100$ kW
$k_\parallel = 2.51$ cm^{-1}	

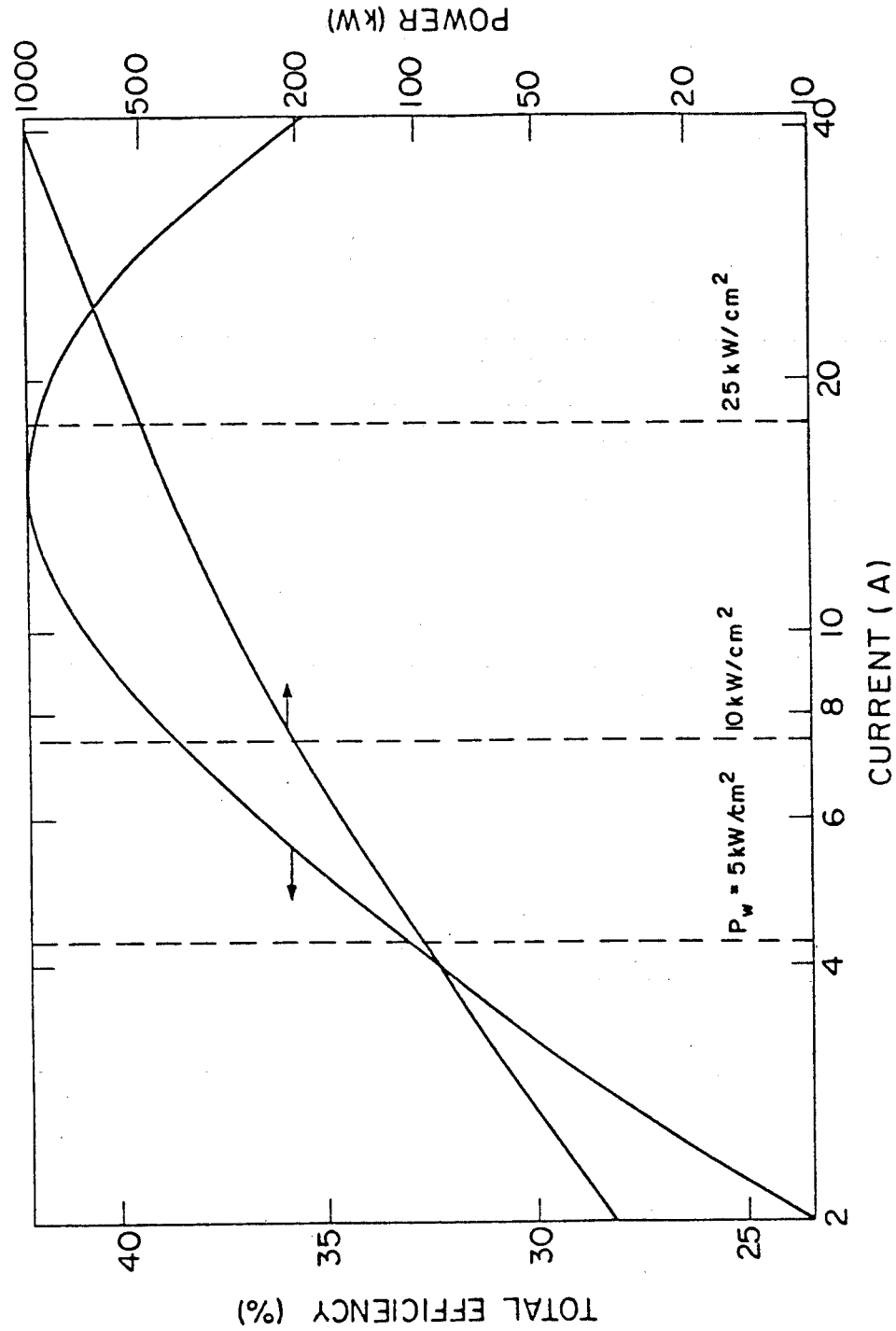

Fig. 5.10 Total Efficiency and Output Power vs. Beam Current. Also shown are Limits Imposed by Wall Heat Flux.

η_T = 39%. The corresponding current would be 7.4 A, giving $\Delta U/U$ = 0.9% and ε_{TOTAL} = 9.8%, both within acceptable levels. Thus, the wall heat flux is the major limit preventing operation at higher powers.

5.2 Microwave Transmission and Port Design

Once the RF power is generated in the gyrotron cavity, a suitable transmission system must be designed that transmits this power to the plasma with relatively small losses. A variety of techniques are available for millimeter wave propagation [66-70].
In this section the advantages and disadvantages of several approaches will be investigated and the one that appears most suitable for high frequency, high power transmission will be selected. A detailed design based on this approach will then be given, including discussion of the loss mechanisms, filters, mode transducers, and windows.

When designing a transmission system, a number of requirements must be satisfied. These include the following:

(1) The system should be compact in order to satisfy space limitations. This suggests the use of a guiding structure that keeps the power concentrated.

(2) Attenuation due to ohmic heating in the guiding structure, diffraction, and conversion to lossy or unusable modes should be small. This simplifies the problem of cooling the structure. This also provides design flexibility since the gyrotron sources can be placed relatively far from the reactor without excessive power losses.

(3) The system should operate well below breakdown voltage, yet be able to support a high power density in order to ensure that the

dimensions of the system do not become excessively large.

(4) Power transmission should not be overly sensitive to system irregularities such as surface roughness, misalignment, joint offsets, etc.

(5) Any mode transformations that are required should be accomplished with minimal conversion to unwanted modes.

(6) If windows are needed, they must withstand vacuum and thermal stresses, and result in minimal insertion losses.

(7) The transmission system should be easy to assemble, disassemble, and align.

Research in the area of high frequency microwave transmission has increased recently as the result of renewed interest in utilizing centimeter and millimeter waves for long distance, trunk communication [68, 71 , 72]. A major reason for this interest has been the need for additional communication channels, and at these wavelengths enormous bandwidths can be made available. The results presented in this section represent to a large extent an extrapolation of this research to the regime of operation of the gyrotron. However, the emphasis in this analysis will differ somewhat from that of microwave communication. Whereas in communication signal distortion represents a major problem, the primary goal here is to minimize power losses, and signal variations do not play a crucial role.

A variety of methods are available for millimeter wave propagation, and a number of these techniques are described in Table 5.2. For each method of propagation, the advantages and disadvantages are given, as well as typical power and attenuation values based on a frequency of 200 GHz. These approaches can be categorized into three

Table 5.2 COMPARISON OF TRANSMISSION TECHNIQUES

TYPE OF PROPAGATION	EXAMPLE	ADVANTAGES	DISADVANTAGES	POWER	ATTENUATION
Free Modes	Free Space	No metal attenuation No connection to reactor Design Flexibility	Safety problems Aperure losses Beam spread	$\lesssim$ 1 MW/cm^2	1.5×10^{-2} dB/m for R_r = 50 cm R_e = 4.5 cm
Beam Modes	Reflecting Mirrors	Minimal attenuation Reduced material requirements No connection to reactor	Alignment Window Safety problems Lack of Experimental results	25 MW/beam	3.3×10^{-4} dB/m
Surface Wave	Cylindrical copper Line	Simple design	Support problems Interference between lines Radiation losses	2500 kW/line	0.1 dB/m (1 cm. diameter line)
Closed waveguide - Multimode	TE_{01} in circular waveguide	Adequate size Self alignment Lower attenuation as ω increases Experimentally tested	Spurious modes More structural material required	800 kW/waveguide	6.8×10^{-3} dB/m (14 mm. diameter pipe)
Closed waveguide - Fundamental mode	TE_{11} in circular waveguide	No spurious modes Known technique Flexibility Self-alignment	High attenuation Low power Rotating polarization	4.2 kW/waveguide	6 dB/m (1.2 mm diameter pipe)

POWER AND ATTENUATION VALUES BASED ON FREQUENCY OF 200 GHz

basic classes of waveguides:

(1) Beam waveguides, where the cross-sectional field distribution of the microwave beam is reconstituted at periodic intervals. Free space transmission, which involves no reconstitution of the beam can also be included here. Beam waveguides are of greatest interest at wavelengths below a few millimeters where conventional waveguides become inefficient for long distance transmission and the required mechanical precision poses severe technological problems.

(2) Surface waveguides, where the field is essentially on the outside of the guiding structure.

(3) Closed waveguides, where the entire field is enclosed by a metal container and shielded from the environment.

High power microwave transmission is hampered primarily by the relatively large transmission losses in the guiding structure. This loss is due to ohmic heating caused by currents flowing in the structure. Efficient power transmission thus requires either a mode which is associated with very low current, or a technique which utilizes very little guiding structure. More favorable are the limitations imposed by electric breakdown on the power-carrying capacity of these waveguides. Most of the waveguides that were investigated could theoretically support the power levels required with a sufficient margin of safety.

Free space transmission [69,70] involves the transmission of power from an emitting to a receiving antenna. The antenna may be a microwave type of receiver, such as a horn, or an optical component, such as a reflecting and/or focusing mirror. This approach offers the

advantage of not using a guiding structure with its inherent losses. Attenuation is due to diffraction and to the intervening air, and as long as the air is kept dry it should cause a negligible attenuation of about 3×10^{-5} dB/m. The lack of waveguide connections to the tokamak reactor results in design flexibility and simplifies the assembly and disassembly procedures. The power carrying capacity of 1 MW/cm^2 [69], based on the breakdown of air at room temperature and one atmosphere pressure, is more than adequate. Potential problems include alignment difficulties, beam spread due to the lack of a mechanism for reconcentrating the beam power, and losses due to mismatches and inefficiencies at the horns/antenna. There is also a safety problem associated with the lack of shielding and the possibility of accidental irradiation of neighboring equipment due to misalignment.

One possible free space transmission system would consist of a focusing reflector as the emitting antenna and a microwave horn as the receiving antenna. One might also utilize a reflector at the receiving end that would focus the incoming power into the horn. For this design it has been assumed each gyrotron will have a separate transmission system in order to avoid problems associated with combining power from different sources. Theory [70] shows that transmission efficiencies greater than 90% can be obtained if $R_e R_r/D\lambda \gtrsim 0.5$, where D is the pathlength, λ is the wavelength, and R_e and R_r are the radii of the emitting and receiving antenna respectively. Using R_r = 50 cm, which is based on space limitations within the reactor building, D = 30 m based on a typical plant layout [65], and λ = 1.5 mm, then $R_r \geq 4.5$ cm is required in order to achieve high transmission efficiency. Such a design appears feasible. However, the safety prob-

lems and difficulties associated with alignment tend to reduce the attractiveness of this system. These problems could be reduced if the gyrotrons were placed closer to the tokamak reactor.

In order to avoid losses due to beam spread, one can utilize quasi-optical techniques to periodically reconcentrate the beam power [67, 69, 70]. The prefix "quasi" is used to indicate that the transmission is governed by a combination of geometric optics and diffraction optical relations. A reflecting mirror, rather than a lens, arrangement, has been investigated because of the low losses of mirrors, and the results are shown on the second row of Table 5.2. As with free space transmission, the reflector system offers the advantages of no waveguide connections to the reactor and lower costs due to the reduced material requirements (as compared to a closed waveguide system). It also suffers from the same alignment and safety problems as free space transmission.

In order to reduce the complexity of a beam waveguide system, it is assumed that all the power of an ECRH station ($\sim$ 25 MW) can be combined into a single beam. Problems involving the adverse interaction of RF radiation from individual gyrotrons can be avoided by allowing each gyrotron to operate at a slightly different frequency. This will not greatly alter the absorption process in the plasma since the frequency bandwidth will remain narrow. The beam is assumed to have a Gaussian cross-sectional profile since this distribution has the highest energy concentration on the beam axis. Studies [69] indicate that Gaussian beams can be obtained with sufficiently high launching efficiencies using conical horns. The mirrors consist of elliptical copper plates shaped to give the appropriate focal length and of suf-

ficient size that the diffraction losses become negligible. Based on the voltage breakdown criterion, these mirrors must be separated by at least 6 meters in order to support a 25 MW beam with λ = 1.5 mm. The choice of reflection angle (the angle between the mirror surface and beam) involves a trade-off between the need for a small angle in order to minimize attenuation due to ohmic losses in the reflectors, and the desire for a large angle to simplify the alignment problem. As indicated by Table 5.2 , beam waveguides appear capable of transmitting high power levels in a low-loss efficient manner. The major problem facing the quasi-optical approach is the difficulties associated with transmitting a 25 MW beam through the vacuum window at the reactor. Assuming that a window will not be able to transmit more than about 5 kW/cm^2, the total window area in this case would be about 5×10^3 cm^2, i.e. 0.5 m^2. It appears unlikely that any single window of that size will be able to withstand the thermal stresses due to internal beam attenuation as well as the stresses resulting from the pressure differential. One possible solution is a division of the main beam into a number of smaller beams just before the vacuum wall, and then transmission of each beam through a separate window. This would allow the use of thinner windows, thus reducing the beam losses, but would add to the complexity of the system. The necessity of locating such a complex structure, which will require precise alignment, at the reactor site is a negative feature of this transmission system.

Surface waveguides [69,70] are defined as transmission systems in which the power is transmitted along the outer surface of a guiding structure. A large variety of surface wave techniques have been developed involving both dielectric and metallic media. These systems

offer the advantages of design simplicity. However, as with beam systems, the lack of shielding causes safety problems. Surface waveguides are also hampered by radiation losses near guide supports, bends, and the launching and receiving horns. There is also the possibility of field interference between neighboring lines if they are too close. For a 1 cm diameter copper transmission line, the power carrying capacity is more than adequate, but the attenuation due to ohmic losses of 0.1 dB/m is too high. Surface waveguides appear to be best suited for high power transmission over very short, straight paths that require minimal structural support for the guide.

The final transmission scheme that was studied was the closed waveguide [69 ,70]. The most common types are the rectangular and circular waveguides. Two versions of the circular guide were investigated; a small diameter tube in which only the fundamental mode, TE_{11}, can propagate, and an oversized tube in which the power is transmitted in the form of a TE_{01} mode but in which a variety of spurious modes can exist. Closed waveguides, because of their inherent shielding, pose a less severe safety problem than open systems, and are less susceptible to misalignment. However, closed guides require more structural material, and this will tend to augment the cost of such a system.

As indicated by Table (5.2), a circular guide supporting only the fundamental mode is not a viable transmission method. High frequency operation requires a very small diameter pipe, and this causes the attenuation to be too high and the power level to be too low. Thus, an oversized tube is the only kind of closed guide that can be used. The choice of TE_{01} as the propagation mode is based on an attractive

feature of TE_{op} modes in circular guides. Their attenuation due to ohmic losses decreases as frequency increases. Thus, at 200 GHz, it is possible to transmit high power levels in a reasonably small diameter pipe and sustain less than a 5% ohmic loss over a 30 m distance. The major difficulty facing oversized guides is losses resulting from coupling between the TE_{01} mode and unwanted modes. Such coupling is caused by a variety of factors, including guide irregularities, surface roughness, and bends.

Another problem with a transmission system utilizing the TE_{01} mode in oversized circular waveguide is the necessity to linearly polarize the radiation at the reactor for ordinary wave plasma heating. This problem could be avoided if linearly polarized radiation were produced near the gyrotron and then transmitted with low loss and low conversion to other modes. This might be possible using TE_{op} modes in a rectangular guide or TE_{11} mode in an elliptical guide. In these cases, the problem of matching the gyrotron output to the guide mode appears to be more severe than in using TE_{01} mode in circular guide. Improved technology of mode conversion, however, could make these other approaches more attractive.

Based on this broad investigation of transmission schemes, the oversized waveguide and reflecting mirror systems appear to be the most attractive methods. Of these two techniques the oversized waveguide has been chosen for a detailed design. Although the quasi-optical approach doesn't require the high mechanical precision of waveguides and can negotiate bends more easily, the problems associated with the need to break up the beam in order to transmit it through a vacuum window

severely penalizes this method, as well as the need to provide some shielding of the beam and the difficulty of aligning the optical structure. The oversized waveguide was also chosen based on past communications research in which total attenuations as low as 1 dB/km were achieved experimentally for a frequency range of 40 to 100 GHz over a distance of several miles [73].

A detailed design based on the oversized waveguide concept will now be given. It is assumed that each of four ECRH stations will deliver 25 MW of RF power to the plasma. Based on a transmission efficiency of approximately 80%, which will be justified later in this section, each station must produce 31.25 MW of power. With each gyrotron producing 100 kW, and assuming an individual oversize circular waveguide transmission run for each gyrotron, this implies a set of 313 pipes running to the reactor. One can envision an 18 × 18 array of transmission waveguides, where the additional tubes over 313 would be used for diagnostics or as spare channels in case working channels were lost. This array of tubes would be encased in a larger container that would provide support. This larger tube might also be used to contain a forced air (or inert gas) flow that would carry away the heat generated in the walls of the waveguides.

Fig. (5.11) shows the major features of the individual transmission waveguides. Since the operating mode of the gyrotron will be TE_{051}, a converter will be necessary to transmorm a TE_{05} mode to a propagating TE_{01} mode. Such a component must be able to accomodate the high power that will be transmitted and at the same time not introduce a large insertion loss in comparison to other loss mechanisms. At the

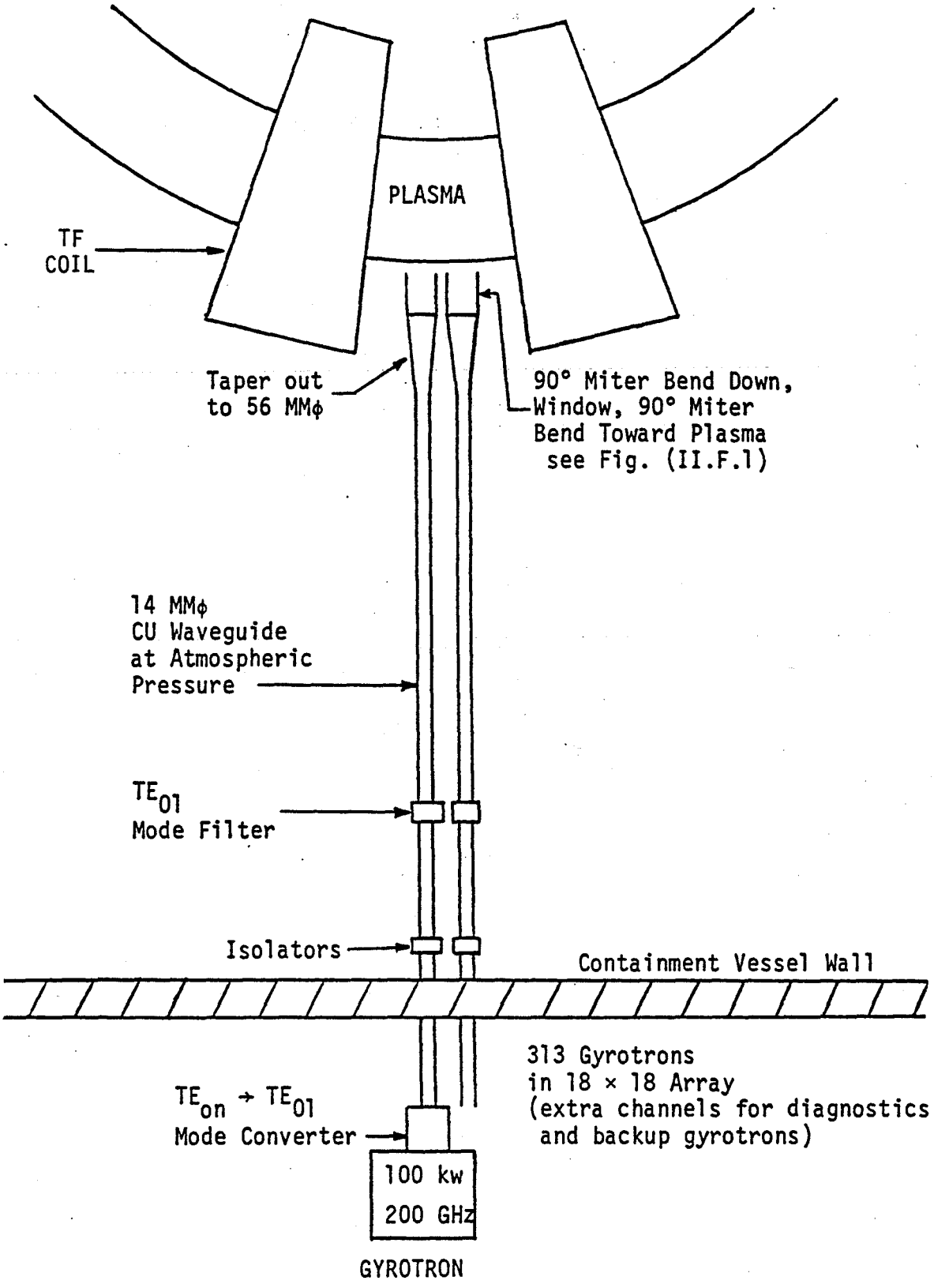

Fig. 5.11 ECRH POWER TRANSMISSION

present time such a device does not exist. One possibility is the use of quasi-optical techniques similar to those used in a design proposed by Vlasov et al. [74 ,75] for transforming circular waveguide modes into polarized, highly directional wave beams or into the principal modes of a rectangular waveguide. In their experimental investigations, they achieved a somewhat low power transformation coefficient of 70 - 75% for λ = 5.1 mm, but expected that this coefficient could be increased if more exact transformer parameters were chosen based on the consideration of diffraction effects.

One potential problem facing the gyrotron is the possibility of RF power being reflected at some point along the transmission path back into the resonant cavity, causing a severe power load and subsequent damage. Such a reflection could occur at the plasma, or might result from an accidental transmission failure caused, for example, by breakdown in the waveguide. Reflected waves might also result from mode conversion at waveguide irregularities. Reflections due to the plasma or mode conversion would not pose major problems, since the power levels associated with these processes should be small, and this power will be in the form of higher order modes which will be severely attenuated by the waveguide. A transmission failure, which conceivably could cause 100% reflection, would be a more serious difficulty, especially if it occurred near the gyrotron. Thus, it may be necessary to protect the gyrotron with an isolator which would allow power transmission only in the forward direction. This component might be in the form of a directional coupling, based either on multiple hole coupling between two waveguides [69] or on quasi-optical techniques [70]. As with the mode transducer discussed earlier, further research is

required in order to design an isolator with high power capabilities and a low insertion loss at the required high frequencies.

A mode filter may be necessary in order to suppress spurious modes that are excited by irregularities in the transmission system. Such modes, if reconverted back into the TE_{01} mode, might adversly interact with the original mode, causing such problems as local heating or breakdown if unwanted resonances occurred. A mode filter should provide low loss for the TE_{01} mode and high losses for unwanted modes. One possibility is the helical waveguide [70], which has the property of high loss for TM modes and TE_{mp} modes with $m \neq 0$. This guide takes advantage of the fact that TE_{op} modes have wall currents only in the aximuthal direction, and provides high resistance to axial currents. Unfortunately, higher order TE_{op} modes with $p > 1$ cannot be suppressed with a helical type mode filter, and at present effective attenuation of these modes requires further research.

The transmission guide as envisioned here will be composed either of high strength copper, or will consist of a steel tube with an inner layer of copper. The inside surface must be polished to a very smooth finish in order to minimize ohmic losses. Two 90° miter bends will be needed at the reactor end in order to gain access to the plasma. This configuration will allow for easy replacement of the reactor modules without removing the overhead transmission guides. Another miter bend will also be needed in the ECRH building in order to provide sufficient room for each gyrotron. A gradual taper will be necessary just before the vacuum window in order to reduce the power density to approximately 5 kW/cm^2, which is consistent with present-day microwave

window experience (at lower frequencies).

The choice of guide radius is based on limitations imposed by voltage breakdown and attenuation due to the walls. The radius should be kept as small as possible in order to minimize coupling between the TE_{01} and spurious modes and keep the transmission system compact, but should be large enough to accomodate 100 kW with a sufficient safety margin and have small ohmic losses. Calculations show that power attenuation is the most limiting criterion for this design. Based on a desire to keep ohmic losses at less than 5% of total power, a waveguide radius of 7 mm was selected. The theoretical power capabilities of such a guide, using 2.9×10^4 V/cm as the breakdown voltage, is 800 kW. In reality, environmental conditions and the presence of waveguide components will lower this maximum level. However, a safety factor of 8 should be adequate if the transmission system is carefully constructed. If it becomes necessary to increase the system power capacity, one might use a gas other than air, such as SF_6, or pressurize the waveguide.

Table 5.3 gives the major design parameters and operating characteristics of the transmission system. The waveguide tolerances and losses are based on pipe qualities that can presently be obtained for communication systems [72]. These tolerances are more precise than those typically associated with commercially produced waveguides. However, it has been shown that they can be achieved utilizing special techniques. The loss mechanisms can be classified into two major groups: losses due to the finite conductivity of the structure, and losses due to the conversion of energy to spurious modes. These individual loss processes will now be discussed in detail.

Table 5.3 Transmission System Parameters

DIMENSIONS:	Wavelength	1.5 mm	
	Inner radius	7.0 mm	
	Wall thickness	1.0 mm	
POWER:	Operating	100 kW	
	Theoretical maximum	800 kW	
	(based on breakdown of air at one atmosphere)		
WAVEGUIDE TOLERANCES:	Ellipticity	10 μm	
	Curvature	800 m	
	Diameter	10 μm	
	Joint Offset	20 μm	
	Joint Tilt	3'	
LOSSES:			
Theoretical ohmic		$(6.8 \times 10^{-3}$ dB/m)	2.0×10^{-1} dB
Estimated realistic ohmic		$(2.7 \times 10^{-3}$ dB/m)	8.1×10^{-2} dB
Mode conversion-curvature		$(2.8 \times 10^{-4}$ dB/m)	8.4×10^{-3} dB
Mode conversion-diameter deviations		$(3.2 \times 10^{-4}$ dB/m)	9.6×10^{-3} dB
Taper (3 m long, 14 mmϕ → 56 mmϕ)			2.3×10^{-2} dB
Miter Bends (3)			1.4×10^{-1} dB
Mode Filter (Helix)			3.0×10^{-3} dB
Mode Transducers (at gyrotron and at reactor)			1.3×10^{-1} dB
Windows (2)			1.9×10^{-1} dB
Joints (3)			1.7×10^{-1} dB
Total			9.6×10^{-1} dB
			(80% transmission)
TEMPERATURE:	Average	31°C	
	ΔT	16°C	

As mentioned earlier, one of the major advantages of using the TE_{01} mode is the reduction of attenuation as frequency increases. For a copper waveguide operating far above cutoff, the theoretical attenuation for TE_{op} modes can be written as:

$$\alpha \cong \frac{8.69}{r} \sqrt{\frac{\omega\varepsilon_o}{2\sigma}} \left(\frac{\omega_{cut}}{\omega} \right)^2 \quad \text{dB/m} \qquad (5.2)$$

where ω_{cut} is the cutoff frequency and r is the guide radius in meters. This equation was used to calculate the guide radius required for a power loss of 5% or less (7.4×10^{-3} dB/m for a 30 m length). In reality, surface roughness and minute surface irrigularities tend to increase the effective resistivity of the walls and cause attenuation to become more severe. Tischer [76] observed that a major contribution to the excess losses of copper guides at millimeter wavelengths was due to an anomaly of the skin effect at room temperature. These effects result in an increase of the attenuation on the order of 40%. This is also in agreement with empirical observations on the WT4 waveguide system [77], where steel pipes were electrolytically plated with copper on a production basis, yielding a waveguide that was found to be stable over a three-year testing period. Based on these findings, an additional attenuation of 2.7×10^{-3} dB/m is anticipated.

Mode conversion results whenever the geometry of the waveguide departs from a perfectly true right circular cylinder. Such departures distort the field configuration of the propagating mode, resulting in the coupling and transfer of energy to spurious modes. These unwanted modes tend to be higher order modes which are quickly dissipated in the waveguide. Since approximately 200 modes can propagate in this

this guide, mode conversion represents a potentially severe problem.

The mode conversion problem can be modeled by m coupled transmission line equations where m denotes the number of possible modes of propagation. Approximate solutions have been obtained for continuous coupling due to random imperfections using first-order perturbation theory [78]. It has been shown [79] that the mode conversion losses can be written in the following general form:

$$\alpha_{MC} = 4.34\ C^2_{a,b}\ S_x\ (\Delta\beta_{a,b}/2\pi) \qquad (5.3)$$

Here α_{MC} is the expected attenuation of mode a in dB/m, $C_{a,b}$ is the coupling coefficient between modes a and b, and S_x is the power spectral density, which describes the magnitude of a particular type of irregularity. S_x is evaluated at the beat frequency of the coupled modes, $\Delta\beta_{a,b}/2\pi$, where $\Delta\beta$ is the difference between the propagation constants of the two modes. Equation (5.3) must be evaluated for each coupling process. The attenuation coefficient α_{MC} has been determined for this system based on deviations of straightness and diameter, utilizing the power spectral densities achieved on the WT4 system. These calculations indicate that mode conversion losses should be small in comparison to ohmic losses for pipe qualities that can presently be obtained.

One potential problem is the degeneracy that exists between the TE_{01} and TM_{11} modes. This raises the possibility of strong coupling between these two modes, especially if any unintentional bends exist along the waveguide run. One technique that might be used to circumvent this problem is the use of a dielectric liner to break the degeneracy.

However, such a liner might not be feasible in a high power environment. If a pure metallic waveguide is utilized, great care will have to be taken to ensure that straightness tolerances are met.

In addition to pipe imperfections, joint discontinuities will also cause coupling between modes. Each waveguide is assumed to be constructed of three, ten-meter sections. Based on typical errors found in communication waveguides, an average offset of 20 μm and a tilt of 3 minutes is anticipated. Of these two factors, the tilt is by far the major difficulty, coupling power primarily into the TE_{12} mode. As Table 5.3 indicates, joint irregularities represent one of the major loss mechanisms.

The losses associated with mode transformation from the gyrotron output mode to the TE_{01} mode and from the TE_{01} mode to a linearly polarized mode are difficult to estimate. The quasi-optical techniques suggested by Vlasov et al., as previously mentioned, have been successfully applied but with a power transmission of only 70 - 75%. These high losses, however, could very likely be reduced by using more complex mirror shapes and/or by reflecting from two or more mirrors. By these techniques, diffraction losses and mode mismatch could, in principle, be greatly reduced. Since the loss per mirror reflection should be of order 1% or less, mode transformation losses in principle can be reduced to a very small value.

If the waveguides are kept at atmospheric pressure, then the RF power will have to propagate through two vacuum windows, one at the gyrotron output and one at the reactor. Candidates for window materials include:

(1) Ceramics - this includes alumina, Al_2O_3, and beryllia, BeO.

(2) Mica - has been used successfully by the Soviets in a high frequency CW gyrotron.

The basic difficulty in evaluating the performance of these windows is a lack of information concerning loss characteristics at frequencies near 200 GHz. For this analysis, a beryllia window with a loss tangent of 1×10^{-3} has been assumed. Calculations indicate that for a 60 mm diameter window, a thickness of 2 mm should be adequate to withstand stresses due to the pressure differential. Based on this thickness, a total loss of 0.19 dB is anticipated. Table 5.3 indicates that this is one of the major transmission loss mechanisms. One possible way of avoiding the use of windows is to evacuate the waveguides. However, this will augment the complexity of the system, and might necessitate the placement of the gyrotrons closer to the reactor. If windows are utilized, there are a number of alternative schemes other than the use of a single, flat window that could reduce thermal stress problems [13].

In order to gain access to the plasma, as well as provide room for the gyrotrons, a minimum of three bends will be required. Two methods have been used in overmoded circular waveguide systems to accomplish a rapid change in direction: a constant-curvature bend, and a miter bend based on quasi-optical principles. The miter bend has been chosen because of its compactness and low loss characteristics. The loss in dB is equal to $2.4\ (\lambda/r)^{1.5}$ for bends with $\lambda/r \ll L$ [69]. For our system, the total loss is expected to be 0.14 dB. This value should be reduced in the future as bend designs become more refined [81].

The final two loss mechanisms that have been considered are those associated with the taper and mode filter. The taper is employed to reduce the RF power density in the window. The losses associated with the taper can be kept small by making the transition sufficiently gradual. Thus, the longer the taper, the less mode conversion one would expect. Assuming a 3 m straight taper, the loss (primarily to the TE_{02} mode) is calculated to be 2.3×10^{-2} dB. This loss, or the taper length, could be reduced by employing a variable taper in which the waveguide shape is chosen to minimize abrupt discontinuities. The mode filter has been theoretically modeled as a one meter section of helical waveguide which will damp out the TE_{mp}, $m \neq 0$, modes. The increased loss in the helical guide as compared to the ohmic losses of a pure copper pipe is approximately 25% [71]. Based on this value, the mode filter will add 3×10^{-3} dB to the total attenuation, and therefore represents a small factor.

Summing all the individual losses, a total attenuation of 0.96 dB is obtained, which translates into an expected power transmission of 80%. Based on the assumption that this heat (except that generated at the window, which will presumably have its own cooling system) will be distributed evenly along the pipe, a temperature fluctuation of 16°C is anticipated for gyrotrons that will be operating for 5 seconds of a 500 second power cycle. The average temperature will be 31°C based on the dissipation of heat by free air convection. Of course, localized heating due to design imperfections could drastically affect the temperature in those areas.

We will now deal specifically with the reactor end of the micro-

wave transmission system. The constraints imposed on the transmission waveguide can be classified into two categories: those resulting from the plasma absorption process, and those associated with the constrained reactor geometry. Requirements due to the plasma include the need to launch the power at a specified angle with respect to the toroidal magnetic field, and to keep diffractive losses at a minimum. Geometric considerations involve the need for sufficient clearance for the waveguide between the magnet coils, as well as adequate access so that microwave components may be replaced when necessary.

Fig. 5.12 shows the ECRH port design. The RF power is transmitted from the gyrotron buildings to the reactor in straight, horizontal waveguides that are supported at an elevation slightly higher than the reactor modules. This allows replacement of the modules without removing the horizontal portion of the guides. After a 90° miter bend, the radiation propagates through the vacuum window to the polarizing and focusing mirrors. The position of the vertical portion of the waveguides is determined by the poloidal coils, and as a result the mirrors are located approximately 3.2 meters from the plasma center. The mirrors transform the circular TE_{01} modes into linearly polarized modes and focus the RF power into the plasma.

In order to allow for the removal of a module, a disconnection joint will be necessary. At this joint, the outer support pipes are held together by a series of bolts fitted through oversized holes in the two mating flanges. When the flanges are preperly matched, the internal array of waveguides are aligned in the correct manner. These internal guides need not be individually bolted because of the unique

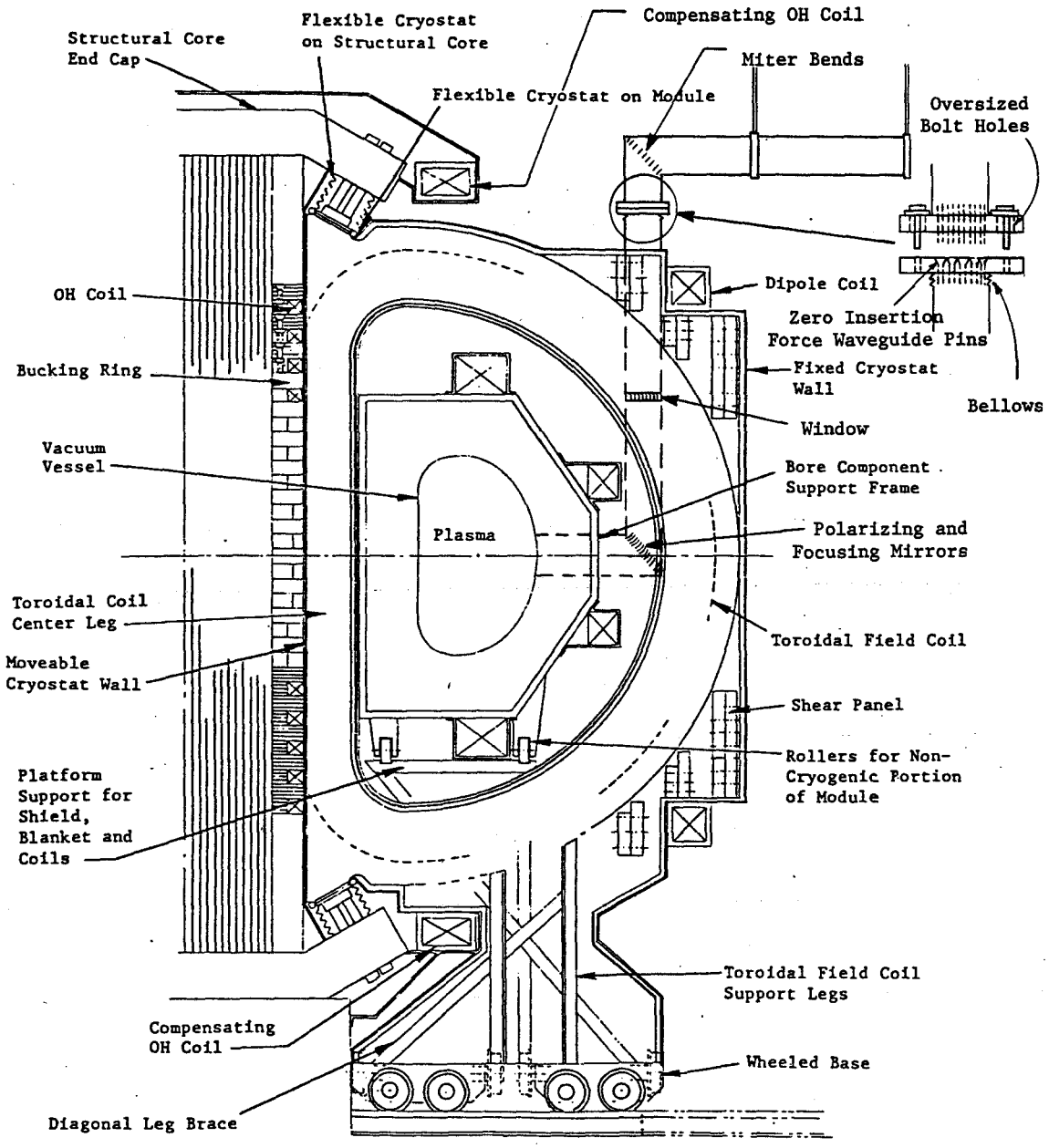

Fig. 5.12 ECRH Port Design

current distribution of TE_{01} modes. Since these modes are supported by wall currents with no longitudinal component, azimuthal breaks will not affect their propagation, and therefore a tight fit at the joint for electrical contact is not necessary. However, care must be taken to ensure that the joint offset and tilt are kept as small as possible in order to minimize mode conversion losses. For this design, the diameter of the outer support tube is determined by the relative positions of the dipole coil and the poloidal coil just outside the blanket. The maximum diameter is 70 cm, which will provide adequate clearance for an 18 × 18 array of 14 mm diameter waveguides.

Past experiments have shown that simple open-ended oversized waveguides are quite effective in launching the power into the plasma. Power densities of 5 kW/cm^2 per port have been used with no major problems [82]. There should be minimal interactive coupling between the four ECRH ports as a result of the efficient power absorption that is anticipated. Based on a power density of 5 kW/cm^2, 100 MW will require 2.0 m^2 of port area, which compares favorably with the 4-5 m^2 required for neutral beam heating of the HFCTR [20]. Thus, the access required for ECRH, which consists of 0.4% of the total first wall area, should have a relatively minor effect on the breeding ratio of the blanket.

The major difficulty associated with the launching of ECR power into the plasma will be the conversion of the waveguide mode to linearly polarized radiation. Direct launching from the end of the oversized waveguide will not be satisfactory because of the circular polarization of the radiation. A mode transducing mirror has been developed by

Wengenroth [80] which utilizes phase and polarization shifting techniques at a reflecting surface. This approach has been demonstrated at 33 GHz. In order to convert the TE_{01} mode, a twist reflector plate is utilized. The angular spread of the beam is approximately λ/D, where D is the diameter of the output waveguide. This gives a spread of 1.5° for this design, which implies an 8.6 cm diameter beam once it reaches the plasma center. Thus, the beam will be sufficiently narrow to be used for localized heating. The RF power will be launched at close to 90° with respect to the toroidal field. The angular spread of 1.5° should have a relatively minor effect on the absorption process.

In addition to the RF power, the polarizers will be subject to a neutron flux that will degrade their performance. This degradation will include an increase in the resistivity of the copper from which they are constructed as well as the possibility of surface erosion. Although the lifetime of these mirrors cannot presently be calculated, provisions must be made for their easy removal in case of failure. This design provides sufficient access through the vertical portion of the waveguide so that, after the internal array of pipes is removed, the mirrors can then be lifted out and replaced. A laser beam can then be used to realign the transmission system.

Also investigated was the possibility of increased ohmic losses due to the higher temperature of the final stretch of waveguide. Calculations indicate this effect should be minimal. First, the losses are relatively insensitive to the wall temperature, with an increase from 30° to 200°C resulting in a 20% rise in ohmic losses. Secondly,

the heating should involve only a small portion of the waveguide, since the blanket protects the entire transmission path prior to the polarizers. If this heating of the waveguide proves problematic, then a cooling system for the final section of guide might be required.

5.3 Conclusions

In this chapter an ECR heating system was designed for a commercial fusion reactor. This study consisted of a parametric analysis of a 100 kW, 200 GHz gyrotron and the design of a microwave transmission and port system. The primary goal of the parametric analysis was to maximize the overall efficiency of the gyrotron in order to reduce power supply requirements and enhance the lifetime of the cavity and collector. The major technological constraints were imposed by the cavity cooling requirements, and by the electron gun on the maximum beam current (see Eq.(C.29) through Eq.(C.31)). A procedure was outlined for selecting a design point that conformed to the technical and physical limitations, and this procedure was used to obtain the reference design given in Table 5.1.

Although the gyrotron model that was developed in Appendix C was found to realistically describe the physical processes of the device, one should understand the limitations of this analysis. The model assumed a simple cavity design (i.e., a gyromonotron) and did not include efficiency enhancement techniques such as magnetic field [42] and RF field [43] profiling. The model was based on the present understanding of the gyrotron, and the conclusions reached might be altered somewhat as the technology of the device improves. The basic purpose

was to determine if a 100 kW, 200 GHz gyrotron appears feasible based on a reasonable extrapolation of present state of the art technology, and to obtain a representative set of design parameters that might characterize such a device. In addition, this study helped to pinpoint major problems that must be investigated in greater detail in the future. On the basis of this analysis, it is recommended that the following areas be examined closely:

(1) Electron gun - find ways of increasing $\beta_\perp/\beta_\parallel$ without introducing a velocity spread in the beam. Increase the breakdown voltage limit so that the mirror ratio α and the velocity spread due to space charge might be reduced.

(2) Cooling - investigate the problems associated with heat removal from the cavity walls and the development of hot spots.

(3) Multimoding - develop mode suppression techniques that will not adversely affect the efficiency of the gyrotron.

(4) Profiling - determine how magnetic and RF field profiling affect the efficiency and operational characteristics of the device.

(5) Higher power devices - increase the power capabilities of the gyrotron in order to reduce the number of gyrotron units required to heat a tokamak. Such a reduction would lessen costs and improve the reliability of an ECR system. One possible avenue is the use of optical cavities as discussed in Chapter 4.

A transmission system utilizing the TE_{01} mode in an oversized waveguide appears feasible based on the analysis of Section 5.2. A total loss of about 20% was calculated, with the potential for lower losses as designs become more refined. Since a fixed frequency is

involved, phase and delay distortions, as well as bandwidth and coherence considerations associated with information transmission systems, are less important. The major goals for a power transmission system are low attenuation, low reflection, reliability, and long life. At present, the primary unknowns include the deleterious effect of spurious modes, as well as a lack of microwave components that can accommodate both high power and high frequency.

Chapter 6

Conclusions

1. For a reactor that utilizes ECR heating, there are important constraints on the reactor operating parameters that in turn result in a lower limit on the gyrotron frequency. These constraints are imposed by the cutoff condition for ECR wave penetration to the plasma center. Of the four heating modes examined (O and X-wave, each at $\omega = \omega_c$ and $2\omega_c$), the ordinary wave at $\omega = \omega_c$ appears to be the most favorable. It has good absorption properties, can be launched from outside the torus (low magnetic field side), and leads to relatively low gyrotron frequencies. For this heating mode, the propagation condition can be written as $\alpha \equiv \omega_{po}^2/\omega^2 < 1$. If the ignition requirements are used to determine the minimum plasma density, then this propagation condition plus beta limits resulting from MHD stability criteria can be used to determine a minimum toroidal field on axis, and subsequently the gyrotron frequency. If the empirical confinement law is expected to degrade somewhat when scaled to reactor conditions (MS = 2), then a compact reactor (plasma radius $\leq$ 1.5 m) with a beta limit of 4% will require a toroidal field greater than 60 kG, which corresponds to gyrotron frequencies above 170 GHz. Further confinement degradation or the presence of impurities will increase this frequency.

2. A general linear theory has been derived for all TE modes of a gyrotron that gives the startup characteristics of the device. A set of analytic

expressions was derived for calculating the starting current and detuning properties for any RF field distribution. The resulting equations are fairly easy to solve, yet remain flexible enough that they can be used to study a variety of topics relevant to gyrotron research, including the effect of beam velocity spread, field profiling, and mode competition. The starting current was found to be simply related to the Fourier transform of the longitudinal field shape. In addition, it was concluded that low q TE_{mpq} modes are relatively insensitive to velocity dispersions of the beam. In Section 3.4 this theory was extended to include all harmonics in the weakly relativistic limit.

3. The theory derived in Chapter 2 was used to examine the effect of RF field profiling on the linear characteristics of the gyrotron. Three distributions were analyzed in detail: sinusoidal, Gaussian, and flat. It was found that slight alterations of the RF field longitudinal distribution can drastically change the minimum starting current and Doppler shift associated with the resonance curve. In the example given, a decrease of I_{ST} by a factor of three was observed for the Gaussian vis à vis the sinusoidal profile. These changes are due to both variations of the profile width and shape. As the profile width is increased, the effective $k_{||}$ decreases, resulting in both a lower starting current and a smaller Doppler shift. Such an effect is observed if one compares a cavity with closed ends to an open resonator in which the field, rather than ending abruptly, extends beyond the ends of the cavity in order to achieve output coupling. If effects related to profile width are eliminated, it is found that a region of low amplitude RF field at the

input end of the cavity, such as the tail of the Gaussian, helps to reduce I_{ST}. This results from the fact that such a region prebunches the electrons, thus reducing their phase dispersion before energy is transferred to the RF field.

4. The potential competition between modes was investigated by plotting the gain curves versus axial magnetic field for a set of neighboring modes. Each curve was calculated using the assumption that the simultaneous presence of other modes had no effect on the starting current. This approach was shown to be valid for an azimuthally symmetric system except for the TE_{mpq} and $TE_{mpq'}$ modes, where $q \neq q'$. For this situation, cross terms resulting from linear mode coupling are not negligible for those magnetic fields that result in comparable starting currents for these two modes. It was also shown that the simple approximation that gyrotron modes are excited at Doppler-shifted frequencies ($\omega = \omega_c \pm k_{||} u$) is inadequate for low q modes, and a more realistic description based on the exact linear theory was developed. Fig. 3.5 shows the typical hierarchy of modes that exists in a gyrotron resonator.

5. In Chapter 4, the linear theory of a gyrotron utilizing an optical cavity was derived. Such a resonator has good mode selectivity characteristics, and may be capable of supporting much higher power levels than a closed cavity. This derivation was kept general in order that results would be applicable to any beam-field configuration and field profile, and also to uncover all possible interaction mechanisms involving the electric and magnetic field. It was found that only the electric field

produces the relativistic phase bunching mechanism that characterizes the gyrotron. Gain is possible with the magnetic field as a result of axial bunching and differences in the electron-RF field interaction time. It was also shown that, contrary to approaches used by previous authors, the field of a high q mode in an oscillator must be modelled as a standing wave rather than a traveling wave.

6. Two beam-field configurations for an optical gyrotron were investigated in detail: wave vector $\bar{k}$ perpendicular to and parallel to the beam. The former case is of interest only when $\bar{E}$ is also perpendicular to the beam, and gives a pure ECM interaction with no magnetic contribution analogous to the mechanism analyzed in detail in Chapter 2. In the latter case, both electric and magnetic mechanisms are present but tend to offset one another, yielding rather high, but feasible, starting currents. Unfortunately, this configuration is very sensitive to a dispersion in the beam parallel velocity.

7. A design study has been carried out for a high power, 200 GHz gyrotron. A projected power level of 100 kW for a single gyrotron oscillator appears feasible. The gyrotron would operate with a 70 kV, 4.4 A beam, with an overall efficiency of 33%. The cavity mode would be TE_{051} with a total Q (ohmic plus diffractive) of 2.3×10^3. The cavity, must dissipate 5 kW/cm^2. The overall design represents, in some respects, a significant extension of present day technology, but the design appears to be practical. There are, however, a number of technological problems

which have to be solved. These include electron gun design for high $v_\perp/v_\parallel$ and low space charge; cavity design to prevent multimoding and enhance efficiency; window, collector and output waveguide design; and cooling systems that avoid hot spots.

8. A potentially low loss system has been designed for transmission of the microwave radiation from the gyrotrons to the plasma. Transmission of the TE_{01} mode in oversize, circular, copper waveguide has been selected. This technique has been field tested in high frequency microwave communications systems, but only low power transmission was studied. A projected overall transmission from the gyrotron output to the plasma of 80% should be feasible. However, some new components will have to be developed in order to achieve this high level of transmission efficiency. Mode transformers, with low insertion loss and high power capability, will have to be developed for mode transformation both from the gyrotron to the oversize TE_{01} mode and from the TE_{01} mode to a linearly polarized mode at the reactor. Mode filters and isolators may also need to be developed.

Appendix A

List of Symbols

The following is a list of symbols used in this thesis. Unless otherwise stated, all quantities are in MKS units. In Chapter 5, the subscript k is used to indicate parameters associated with the gun cathode.

a = plasma radius

$\bar{B}_o$ = static axial magnetic field

E_s = cavity stored energy

$\bar{E}_\ell$ = orthonormal electric mode

$E_{\perp k}$ = electric field between cathode and first anode

$F_c, F_s, F_1, \ldots, F_4$ = gain functions

f_o = unperturbed electron distribution

f_1 = perturbed electron distribution

$G(R_e)$ = Beam-RF field coupling coefficient

$g(z)$ = axial RF field profile

H_ℓ, H_m = Hermite polynomials

$\bar{H}_\ell$ = orthonormal magnetic mode

I = beam current

I_{ST} = gyrotron starting current

$\bar{J}$ = perturbed electron current

P = gyrotron power

$P_\perp$, $P_{||}$ = electron momentum components

P_{RF} = work done by the RF field on electrons

P_w = wall power density

Q_D = diffractive Q

Q_{OHM} or Q_o = ohmic Q

Q_T = total quality factor of resonator

R_e = annular electron beam radius

R_o = resonator radius

r_L = Larmor radius

$s \equiv \omega_c / k_{||} u$

$\bar{T}$ = density averaged plasma temperature

T_w = wall temperature

TE_{mpq} = transverse electric mode

TM_{mpq} = transverse magnetic mode

$k_\perp$ = wavenumber perpendicular to $\bar{B}_o$

$k_{||}$ = wavenumber parallel to $\bar{B}_o$

L = cavity length

m_e = rest mass of electron

$N(r,\theta)$ = electron spatial density

n = harmonic number

n_o = peak plasma density

$\alpha \equiv \omega_p^2/\omega_c^2$ (Chapter 2)

α = magnetic field compression ratio (Chapter 5)

β = v/c

β_c = beta limit

γ = relativistic gamma factor

ε = velocity spread

$\eta_\perp$ = transverse efficiency

η_T = total efficiency

λ = mode wavelength

$\nu \equiv \omega/2\pi$

$\bar{T}(r,\theta)$ = transverse field structure

U = beam (cathode) voltage

u = electron velocity parallel to $\bar{B}_o$

V_a = anode voltage

w = electron velocity perpendicular to $\bar{B}_o$

$x \equiv (n\omega_c - \omega)(k_{||}\, u)^{-1}$ detuning parameter

ν_{mp} = transverse mode index

σ = conductivity

τ_E = energy confinement time

ϕ = velocity phase angle of electron

ϕ_k = cathode-magnetic field angle

ω = mode frequency

ω_c = cyclotron frequency

ω_p = plasma frequency

ℓ_k = emitting strip width

Appendix B

Derivation of the Interaction Integral

The derivation of Eq. (3.11), which describes the linear interaction of the electron beam and RF field, will be outlined in this appendix. The technique utilized, known as the method of characteristics, involves the integration of the forces acting on each electron along its unperterbed orbit in order to determine the altered electron velocity distribution, and subsequently the perturbed current J_1. In addition, the expression of the functions F_c and F_s in terms of Fourier transforms of the longitudenal profile g(z) will be shown. In this section the subscript ℓ has been deleted.

The time evolution of the electron distribution is governed by the Vlasov equation

$$\frac{\partial f}{\partial t} + \bar{v} \cdot \frac{\partial}{\partial x} f - \frac{e}{m} (\bar{E} + \bar{v} \times \bar{B}) \cdot \frac{\partial}{\partial \bar{v}} f = 0 \qquad (B.1)$$

where collisional effects are negligible and therefore not considered. This equation can be linearized by letting the distribution function f and fields $\bar{E}$ and $\bar{B}$ be expressed in terms of an equilibrium value plus a perturbation: $f = f_o + f_1$, $\bar{B} = \bar{B}_o + \bar{B}_1$, and $\bar{E} = \bar{E}_1$. In these expansions $\bar{B}_o$ is the uniform axial magnetic field, $\bar{B}_1$ and $\bar{E}_1$ are the RF field components, and there is no equilibrium electric field. These are substituted into the Vlasov equation, and nonlinear terms are dropped. If f_o is assumed to satisfy the zero-order Vlasov equation

$$\frac{\partial f_o}{\partial t} + \bar{v} \cdot \frac{\partial}{\partial \bar{x}} f_o - \frac{e}{m} (\bar{v} \times \bar{B}_o) \cdot \frac{\partial}{\partial \bar{v}} f_o = 0 \qquad (B.2)$$

then this equilibrium condition can be subtracted from the linearized perturbed equation to yield the following result

$$\frac{\partial f_1}{\partial t} + \bar{v} \cdot \frac{\partial}{\partial \bar{x}} f_1 - \frac{e}{m}(\bar{v} \times \bar{B}_0) \cdot \frac{\partial}{\partial \bar{v}_1} f_1 = \frac{e}{m}(\bar{E}_1 + \bar{v} \times \bar{B}_1) \cdot \frac{\partial}{\partial \bar{v}} f_0 \tag{B.3}$$

The goal now is to express f_1 in terms of the other quantities. This is achieved by defining the following equations, known as characteristics:

$$\begin{aligned} \frac{d\bar{x}'}{d\tau} &= \bar{v}' \\ \frac{d\bar{v}'}{d\tau} &= -\frac{e}{m}(\bar{v}' \times B_0) \\ \frac{dt'}{d\tau} &= 1 \end{aligned} \tag{B.4}$$

where τ is a parameter characterizing the unperturbed orbit (i.e., changing τ implies motion along the orbit). These equations are a direct result of the zero-order Vlasov equation (B.2). The primes indicate that the parameters are functions of τ. The boundary conditions are $\bar{x}'(\tau=t)=\bar{x}$ and $\bar{v}'(\tau=t)=\bar{v}$. If Eq.(B.3) is written in terms of primed quantities, and Eqs.(B.4) are substituted in, the left-hand side of Eq.(B.3) reduces to the exact differential $df_1'/d\tau$, where $f_1' \equiv f(\bar{x}', \bar{v}', \bar{t}')$. The perturbed distribution f_1 is obtained by integrating $df_1'/d\tau$ from $\tau=-\infty$ to t, which yields

$$f_1(\bar{x}, \bar{v}, t) = \frac{e}{m}\int_{-\infty}^{t} [E(\bar{x}',\tau) + \bar{v}' \times \bar{B}_1(\bar{x}', \tau)] \cdot \frac{\partial}{\partial \bar{v}'} f(\bar{v}', \bar{x}')\, d\tau \tag{B.5}$$

where $f_1'(\tau = -\infty)$ is equal to zero.

The next step is to express the integrand explicitly in terms of

τ. If the RF field is in the form of a TE mode, the components can be written in cylindrical coordinates as $\bar{B}_1 = B_\theta\hat{\theta} + B_r\hat{r} + B_z\hat{z}$ and $\bar{E}_1 = E_r\hat{r} + E_\theta\hat{\theta}$. If the velocity is written in terms of its components, $\bar{v} = u\hat{u} + w\hat{w}$, and ϕ is the phase of $\hat{w}$ with respect to the $\hat{x}$ axis, then the integrand can be written as

$$(\bar{E}' + \bar{v}' \times \bar{B}') \cdot \frac{\partial f_0}{\partial \bar{v}'} = [E'_\theta \sin(\phi' - \theta') + E'_r \cos(\phi' - \theta')]\frac{\partial f_0}{\partial w'}$$

$$+ [B'_r \sin(\phi' - \theta') - B'_\theta \cos(\phi' - \theta')](u'\frac{\partial f_0}{\partial w'} - w'\frac{\partial f_0}{\partial u}) \qquad (B.6)$$

Since no electron prebunching is assumed, $\partial f_o/\partial\phi = 0$ and associated terms have been dropped. Expressions for the spatial and velocity components are obtained by integrating the characteristic equations (B.4). The middle equation is just the equation of motion of a circulating particle with a cyclotron frequency $\omega_c = eB_o/\gamma m_e$. There is no force in the parallel direction, and as a result u' is a constant. If the assumption is made that variations of the field across the Larmor orbit are small, and the electrons effectively see the field at the gyro-center, then r' and θ' can also be treated as constants along each orbit. This assumption can be expressed mathematically for a gyrotron as $k_\perp r_L \simeq \beta_\perp << 1$, and in effect restricts this theory to the fundamental (i.e., first harmonic) interaction since higher harmonics result from field variations across the orbit. The following equations can now be derived:

$$r'(\tau) = r \qquad u'(\tau) = u$$

$$\theta'(\tau) = \theta \qquad w'(\tau) = w$$

$$z'(\tau) = u(\tau - t) + z \qquad \theta'(\tau) = \omega_c(\tau - t) + \theta$$

(B.7)

In order to use the above equations in Eq.(B.6), the RF field components must be written explicitly in terms of the spatial coordinates. Restricting our attention to TE modes, the magnetic terms can be dropped since the electric field interaction dominates (see Chapter 5 for the treatment of magnetic terms). Writing the $\bar{E}$ field as in Eq. (3.8) with $\bar{T}(r,\theta) = E_r\hat{r} + E_\theta\hat{\theta}$, Eq. (B.6) becomes

$$\bar{E}_1' \cdot \frac{\partial f_0}{\partial \bar{v}'} = \{E_\theta \sin[\omega_c(\tau-t)+\phi-\theta] + E_r \cos[\omega_c(\tau-t)+\phi-\theta]\}\, g[z+u(\tau-t)]e^{i\omega\tau} \frac{\partial f_0}{\partial w}$$

(B.8)

Expanding the trigonometric functions, defining $\delta \equiv t-\tau$, and noting that $\bar{T}\cdot\hat{w} = E_r \cos(\phi-\theta) + E_\theta \sin(\phi-\theta)$ and $\bar{T} \times \hat{w} \cdot \hat{z} = E_r \sin(\phi-\theta) - E_\theta \cos(\phi-\theta)$ gives

$$\bar{E}_1' \cdot \frac{\partial f_0}{\partial \bar{v}'} = \left[(\bar{T}\cdot\hat{w})\cos\omega_c\delta + (\bar{T}\times\hat{w}\cdot\hat{z})\sin\omega_c\delta\right] g(z - u\delta)e^{i\omega(t-\delta)} \frac{\partial f_0}{\partial w}$$

(B.9)

The perturbed distribution, given by Eq.(B.5), now becomes

$$f_1(\bar{x},\bar{v},t) = \frac{e}{m}\int_0^\infty d\delta \left[(\bar{T}\cdot\hat{w})\cos\omega_c\delta + (\bar{T}\times\hat{w}\cdot\hat{z})\sin\omega_c\delta\right] g(z-u\delta)e^{i\omega(t-\delta)} \frac{\partial f_0}{\partial w}$$

(B10)

The perturbed current $\bar{J}$ can be expressed as $\bar{J} = -e\int d\bar{v}\ \bar{v}N(r,\theta)\ f_1(\bar{x},\bar{v},t)$ where N is the spatial beam density and the integration is performed over velocity space. The interaction integral is obtained by multiplying $\bar{J}$ by $p_o^*\cdot\bar{E} = T^*(r,\theta)\ g(z)e^{-i\omega t}$ and integrating over the interaction

volume:

$$p_o^* \int_V d^3r\ \bar{J}\cdot\bar{E} = -\frac{e^2}{m}\int_{-\infty}^{\infty}dz\int_0^{2\pi}d\theta\int_0^{R_o}rdr\int_0^{2\pi}d\phi\int_0^{\infty}w^2dw\int_{-\infty}^{\infty}du\int_0^{\infty}d\delta\ \frac{\partial f_o}{\partial w}\ N(r,\theta)$$
$$\cdot[\cos(\omega_c\delta)g(z)g(z-u\delta)e^{-i\omega\delta}(\bar{T}\cdot\hat{w})(\bar{T}^*\cdot\hat{w})+\sin(\omega_c\delta)g(z)g(z-u\delta)e^{-i\omega\delta}(\bar{T}\times\hat{w}\cdot\hat{z})(T^*\cdot\hat{w})] \quad (B.11)$$

This expression can be simplified by performing the ϕ integrals first:

$$\int_0^{2\pi}d\phi\ (\bar{T}\cdot\hat{w})(\bar{T}^*\cdot\hat{w}) = \pi\cdot(\bar{T}\cdot\bar{T}^*)$$

$$\int_0^{2\pi}d\phi\ (\bar{T}\times\hat{w}\cdot\hat{z})(\bar{T}^*\cdot\hat{w}) = \pi\cdot(\bar{T}\times\bar{T}^*\cdot\hat{z})$$

and then separating the spatial integrals to obtain the geometric factors G_D and G_C of Eq.(3.11). The z and δ integrals are combined to get the following functions:

$$F_a = 2\ k_{\parallel}^2\int_{-\infty}^{\infty}dz\int_0^{\infty}d\delta\ \cos\ \omega_c\delta\ g(z)\ g(z-u\delta)\ e^{-i\omega\delta}\ u$$

$$F_b = 2\ k_{\parallel}^2\int_{-\infty}^{\infty}dz\int_0^{\infty}d\delta\ \sin\ \omega_c\delta\ g(z)\ g(z-u\delta)\ e^{-i\omega\delta}\ u \quad (B.12)$$

If the trigonometric functions are written in terms of exponents, and only the resonant terms are retained (i.e. those terms that are slowly varying functions of δ), then F_a and F_b can be expressed as $F_a = iF_b = F_c + iF_s$, where F_c and F_s are the gain functions used in Chapter 3. The nonresonant terms, which are expressed in terms of quickly varying functions of δ, are negligible upon integration over δ. Eq.(B.11) now becomes

$$p_o^* \int_V d^3r\ \bar{J}\cdot\bar{E} = -\frac{e^2}{m}\frac{\pi}{k_{\parallel}^2}\int_{-\infty}^{\infty}du\int_0^{\infty}dw\ \frac{\partial f_o}{\partial w}\ \frac{1}{2}\frac{w^2}{u}\ (F_c + iF_s)[(G_D - iG_c)] \quad (B.13)$$

The final step required to obtain Eq.(3.11) is an integration by parts to eliminate the derivative of f_o. Here one must remember that F_c and

F_s are functions of x, and that $x = (\omega_c - \omega)/k_{||}\, u$ is a function of w since ω_c contains the relativistic factor γ. Noting that $f_o(w=\infty) = f_o(w=0) = 0$ and that $\partial x/\partial w = -\gamma^2 (w/c^2)(\omega_c/k_{||}\, u)$, an integration of parts is equivalent to the following transformation:

$$\frac{\partial f_o}{\partial w}\, w^2\, (F_c + iF_s) \rightarrow -f_o\, w\, [2 - \gamma^2 (\frac{\omega_c}{k_{||} u})(\frac{w}{c})^2 \frac{d}{dx}](F_c + iF_s) \tag{B.14}$$

Eq.(3.11) can now be quickly obtained.

Returning to F_c and F_s, the substitutions $\lambda \equiv k_{||} \delta u$ and $\tilde{z} = k_{||}\, z$ are used to derive Eqs.(3.12a) and (3.12b). Note that the information about the interaction length along z is contained in g(z). Concentrating on F_c, the convolution integral within it can be rewritten as:

$$\int_{-\infty}^{\infty} d\hat{z}\; g(\hat{z})\; g(\hat{z}-\lambda) = \int_{-\infty}^{\infty} \mathcal{L}(\alpha)\, \bar{\mathcal{L}}(\alpha)\; e^{-i\lambda\alpha}\, d\alpha \tag{B.15}$$

where $\mathcal{L}$ is the Fourier transform as defined in Chapter 3, and $\bar{\mathcal{L}}$ is the transform of g(-z). One can quickly show that $\bar{\mathcal{L}}$ is equivalent to $\mathcal{L}^*$. F_c can now be expressed as

$$F_c = \mathrm{Re} \int_{-\infty}^{\infty} d\alpha\, \mathcal{L}(\alpha)\, \mathcal{L}^*(\alpha) \int_0^{\infty} e^{i\lambda(x-\alpha)}\, d\lambda \tag{B.16}$$

Since we are interested in the real part of this expression, the lower limit of the λ integral can be changed to $-\infty$ if the right-hand side is multiplied by one-half. The λ integral can then be written in terms of a delta function that is nonzero only at $\alpha = x$. Eq.(3.17) quickly follows.

The expression of F_s in terms of F_c via the Kramers-Kronig relation (Eq.(3.18)) can be justified if one can prove that

$$\pi \cdot \sin(\lambda x) = P \int_{-\infty}^{\infty} \frac{\cos(\lambda \alpha)}{x-\alpha} \, d\alpha$$

This identity can be shown to be true if a contour integral is done around the simple pole at $\alpha = x$.

Appendix C

Gyrotron Model

A complete design of a high frequency gyrotron can be carried out using a combination of analytic expressions and numerical results derived primarily from the Soviet literature. The model utilizes an adiabatic electron gun theory [83], numerical resonator model [31], and computer calculations of cavity efficiency [32, 63]. These principles may be summarized in a relatively simple analytic model which is very useful for preliminary gyrotron design and for evaluation of technological feasibility, and which serves as the basis of the parametric analysis. It should be recognized that eventually many of the final design parameters must be obtained from computer calculations that more accurately model the physical processes of the device. However, the analytic theories used here do serve to define the approximate value of many parameters and so are of great use in preliminary designs as a result of their simplicity.

C.1 Gyrotron Cavity

The cavity is assumed to be a nontapered right circular cylinder that supports cylindrical TE_{mpq} modes. Each mode is characterized by a transverse index ν_{mp} that is the p^{th} zero of $J_m'(y) = 0$. Since a gyrotron operates near cutoff, it can be shown that the cavity length $L>>\lambda$, and that the wave equation becomes

$$\omega = \frac{2\pi c}{\lambda} \simeq \frac{\nu_{mp} c}{R_o} \qquad (C.1)$$

In order to further simplify the present discussion, the indices m and q are fixed at 0 and 1 respectively. The choice of m = 0 appears to be optimum for low mode operation at $\omega = \omega_c$, while q = 1 is important for maintaining single mode operation and achieving high efficiency.

The beam radius, R_e, must be matched to a maximum in the transverse RF field distribution. This requires

$$R_e = \frac{\nu_{1r}}{\nu_{op}} R_o \quad , \quad 1 \leq r \leq p \tag{C.2}$$

when the beam coincides with the r^{th} radial maximum of the TE_{op1} mode. The electron gyroradius, r_g, is given by

$$r_g = \frac{v_\perp}{\omega_c} = \frac{c\beta_\perp}{\omega_c} \quad \frac{c\beta_\perp}{\omega} = \frac{\beta_\perp \lambda}{2\pi} \tag{C.3}$$

The ratio of r_g to the beam radius R_e is:

$$\frac{r_g}{R_e} \simeq \frac{\beta_\perp \lambda}{2\pi} \frac{1}{R_o(\nu_1/\nu_{op})} = \frac{\beta_\perp}{\nu_{1r}} \quad , 1 \leq r \leq p$$

Hence $r_g << R_e$ and the electron beam is in the form of a hollow cylinder.

The theoretical ohmic Q, Q_{OHM} is given, for a TE_{op1} mode, by

$$Q_{OHM} = \frac{R_o}{\delta} \frac{\nu_{op}^2 + \left(\frac{\pi}{2}\right)^2 r^2}{\nu_{op}^2 + \left(\frac{\pi}{2}\right)^2 r^3} \tag{C.4}$$

where $r = 2 R_o/L$ and δ is the skin depth. For $L/\lambda >> 1$, Q_{OHM} is given to high accuracy by:

$$Q_{OHM} = R_o/\delta \tag{C.5}$$

For a copper cavity at $\lambda = 1.5$ mm, $\delta \simeq 1.85 \times 10^{-5}$ cm at $T_w = 200^0$ C. It is important to allow for a somewhat degraded Q_{OHM} due to surface imperfections, particularly at short wavelengths. For example, it may be better to assume

$$Q_{OHM} = \Lambda R_o/\delta$$
$$\Lambda \simeq 0.5 - 0.8 \qquad (C.6)$$

The diffractive Q of the resonator is given by

$$Q_D = 4\pi \frac{L^2}{\lambda^2} \frac{1}{1 - |R_1 R_2|} \qquad (C.7)$$

where R_1, R_2 are the electric field reflection amplitude coefficients at the two ends of the cavity. The minimum cavity Q is given by:

$$Q_{MIN} = 4\pi L^2/\lambda^2 \qquad (C.8)$$

We may redefine Q_D as:

$$Q_D = K\, Q_{MIN} \qquad (C.9)$$

In general, the parameter K varies with cavity shape, mode, length and diameter. For the cavity assumed in this model, K is not a strong function of cavity mode and a rough value of $K \simeq 3$ is obtained [31]. Hence $Q_D \simeq 3\, Q_{MIN}$. The total cavity Q, Q_T, is given by:

$$\frac{1}{Q_T} = \frac{1}{Q_D} + \frac{1}{Q_{OM}} \qquad (C.10)$$

As will be shown later, it is important to have $Q_D \ll Q_{OM}$ in order to achieve high efficiency.

The overall efficiency for conversion of beam power to output RF power is denoted by η_T. Only the transverse energy of the electrons may be converted to output power. The transverse efficiency, $\eta_\perp$, can

be calculated numerically from the motion and RF field equations. This has been done by Nusinovich and Erm [63], and their results, modified by Gaponov et al. [32], are shown in Fig. C.1 for first and second harmonic operation. Their calculations are applicable to weakly relativistic, monoenergetic beams with no velocity spread and to an RF field with a Gaussian longitudinal profile. Their results can be utilized in this model as long as the beam voltage U does not become too large ($U < 100$ kV) and the velocity spread is not excessive [32]. The use of a Gaussian to describe the RF field structure has been verified experimentally to be valid in the case of simple open resonators such as the one assumed here. The graphs of Fig. C.1 express η as a function of two parameters, the normalized beam current I_o and normalized cavity length μ.

In addition to $\eta_\perp$, one must also calculate the efficiency for conversion of electron beam power to transverse power, η_{el}. This can be written as:

$$\eta_{el} = \left[1 + (\beta_\parallel/\beta_\perp)^2\right]^{-1} \tag{C.11}$$

Finally, the efficiency factor that accounts for ohmic losses in the cavity walls, η_Q, can be expressed as:

$$\eta_Q = 1 - Q_T/Q_{OHM} = Q_{OHM}/(Q_D + Q_{OHM}) \tag{C.12}$$

The total efficiency can now be written as:

$$\eta_T = \eta_\perp \eta_{el} \eta_Q \tag{C.13}$$

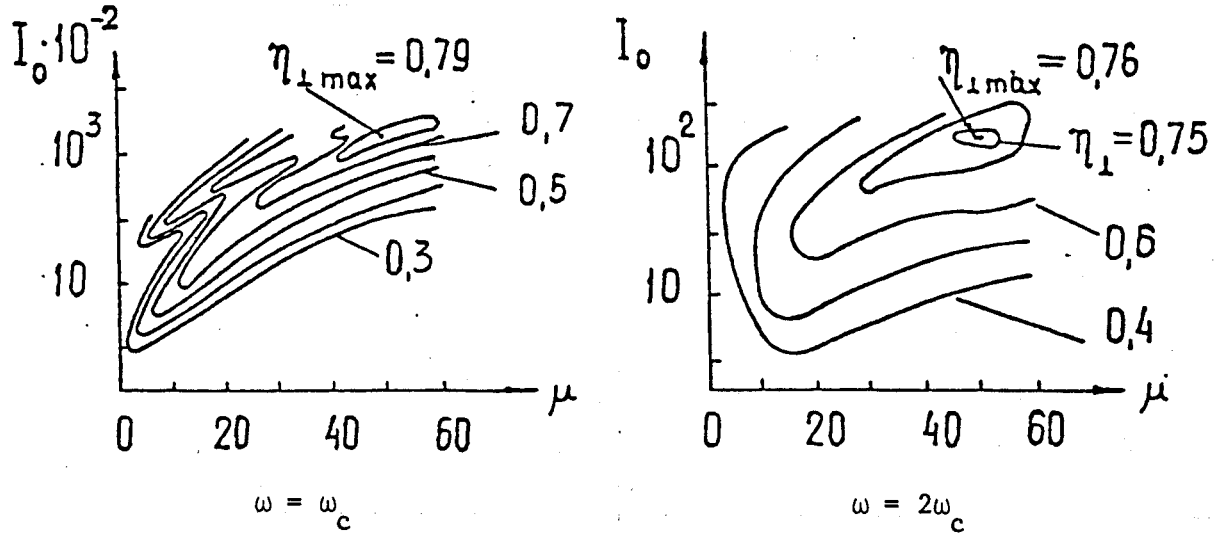

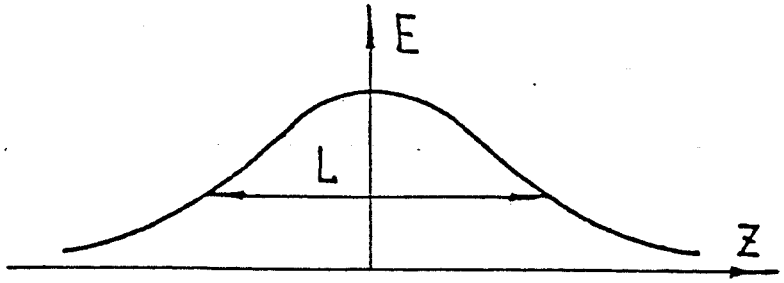

$$I_0 = 0{,}24 I(a)(Q \cdot 10^{-3}) \left(\pi \frac{\beta_\perp}{\beta_{\parallel}}\right)^{2(3-n)} \left(\frac{L}{\lambda}\right)^{5-2n} \left[\frac{(n/2)^n}{n!}\right]^2 G$$

$$G = \frac{J^2_{m-n}(\nu_{mp} R_0 / R_p)}{(\nu^2_{mp} - m^2) J^2_m(\nu_{mp})}$$

$$\ell = \pi \frac{\beta^2_\perp L}{\beta_{\parallel} \lambda}$$

Fig C.1 Gyrotron Transverse Efficiency Based on Nonlinear Theory of Nusinovich and Erm [63]

C.2 Gyrotron Gun

A typical gyrotron gun, known as a magnetron injection gun, is illustrated schematically in Fig. C.2 along with its fundamental parameters. In order to differentiate between cathode and cavity parameters, those associated with the cathode have a k subscript. A number of additional parameters can also be defined or calculated based on the cathode's operating characteristics. The relativistic factor γ is given by:

$$\gamma = \frac{1}{\sqrt{1 - \beta^2}} = 1 + \frac{U}{511 \text{ keV}} \tag{C.14}$$

The perpendicular electric field near the cathode is given by

$$E_{\perp k} = \frac{V_1}{R_k} \frac{1}{\ell n \frac{R_k + d}{R_k}} \simeq \frac{V_1}{d} \text{ for } d << R_k \tag{C.15}$$

The perpendicular velocity of the electrons just above the cathode is:

$$\beta_{\perp k} = 3.33 \times 10^{-6} \frac{E_{\perp k}}{B_k} \tag{C.16}$$

where $E_{\perp k}$ is in V/cm and B_k is in kG. The initial height to which an electron rises above the emitter strip is $2r_k$ where

$$r_k = \frac{\beta_{\perp k}}{\omega_{ck}} \tag{C.17}$$

The emitter strip area A is given by,

$$A = 2\pi R_k \ell_k \tag{C.18}$$

and the emitter current density, J_k, is

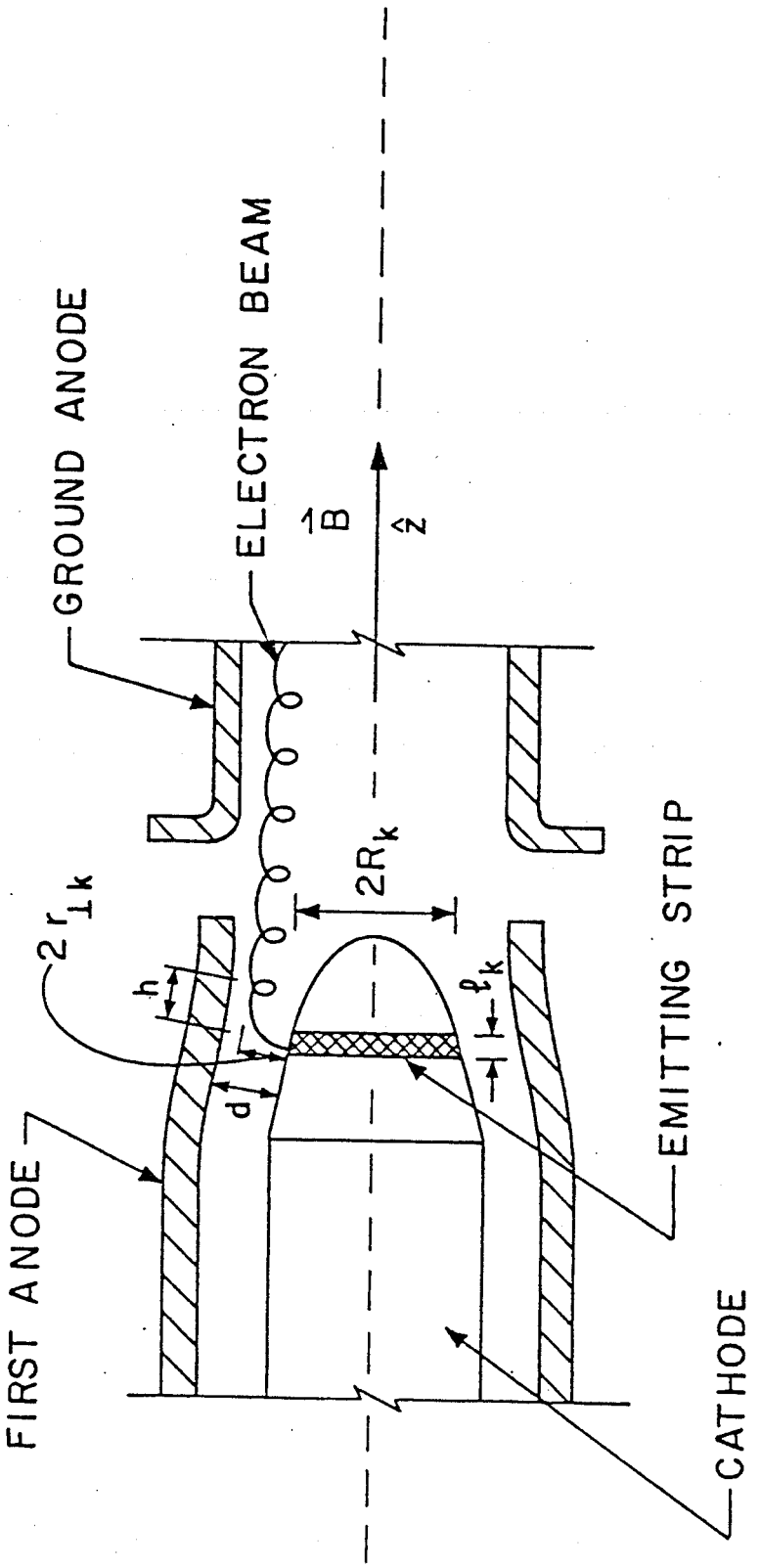

Fig. C.2 GYROTRON GUN

$$J_k = I/2\pi R_k \ell_k \tag{C.19}$$

Some parameters in the gun and cavity regions are correlated via the mirror ratio, $\alpha = B_o/B_k$. It is assumed that the electron trajectories between the gun and cavity are adiabatic. Then

$$R_k = \alpha^{1/2} R_e \tag{C.20}$$

$$\beta_\perp = \alpha^{1/2} \beta_{\perp k} \tag{C.21}$$

$$\beta_{||} = (1 - \gamma^{-2} - \beta_\perp^2)^{1/2} \tag{C.22}$$

C.3 Operating Constraints

The major limits that constrain the operating regime of the gyrotron will now be discussed. Our model includes limitations imposed by the cooling requirements and constraints imposed on the beam parameters by the electron gun. In the case of cooling, the main problem is the removal of heat resulting from ohmic currents in the cavity walls. This heat flux P_W can be calculated from the Q's of the cavity. Since Q_{OHM} is defined as the ratio of the cavity stored energy to ohmic power losses in the walls, and Q_D is the ratio of the stored energy to P, one can express P_W as:

$$P_W = \left(\frac{Q_D}{Q_{OHM}}\right)\left(\frac{P}{2\pi R_o L}\right) \tag{C.23}$$

P_W can be written interms of R_o and L (for fixed P and ω) by substituting Eqs. (C.6) and (C.9) for Q_D and Q_{OHM}:

$$P_W = \frac{2KPL\delta}{\Lambda\lambda^2 R_o^2} \tag{C.24}$$

In order to calculate the skin depth δ for Q_{OHM} and P_W, the temperature of the inner cavity wall, T_W, must be known. This requires a detailed analysis of the cavity cooling system. Such an analysis has been done for this design [65], and based on its results a wall temperature of 200°C has been chosen. T_W will be treated as a constant, which is satisfactory since both δ and Q_T are relatively weak functions of T_W.

The procedure followed for selecting the gun parameters, and the subsequent limits on beam current will now be outlined. The magnetic compression factor α is determined either by the maximum electric field allowable in the cathode, or by the need for sufficient clearance for the electrons between the emitter and the first anode. If the breakdown electric field is set at 1 x 10 V/cm, Eqs. (C.16) and (C.21) can be combined and written as:

$$\alpha \geq 1.05\ (\alpha\beta_\perp\omega)^{2/3} \tag{C.25}$$

where ω is in GHz. The clearance requirement can be written as $d > (2\ r_k + \ell_k\phi_k)$, where $2r_k$ is the electron orbit diameter in the cathode region and $\ell_k\phi_k$ represents a spread in the beam due to the finite width of the emitter strip. This expression yields:

$$\alpha > 1.71 \times 10^3 \left(\frac{\gamma\beta_\perp}{U}\right) (2\beta_\perp + .33) \tag{C.26}$$

where U is in kilovolts. As a result of the need to keep the magnetic compression as small as possible [64], the minimum value of α satisfying both Eqs. (C.25) and (C.26) is selected.

The width of the emitter strip should be made as large as possible in order to minimize the current density at the strip.

However, the need to keep the beam width reasonably small sets an upper limit on ℓ_k. If the beam width is restricted to one-tenth the width of an RF field radial peak, this gives:

$$\ell_k \simeq 120 \left(\frac{\sqrt{\alpha}}{\omega}\right) \text{ mm} \tag{C.27}$$

where ω is in GHz. Here the angle ϕ_k has been fixed at 7.5^0. The first anode voltage has also been fixed at $V_a = 0.3$ U, which is consistent with past design studies of the electron gun [64]. In practice, the actual value of V_a is determined by the electron-optics of the gun, and requires a computer simulation of the electron orbits. Based on this value of V_a, the gap d can be calculated using d = 0.03 U, where d is in millimeters and U is in kilovolts.

The major limits on the beam current can now be calculated. The first results from the need to keep the velocity spread of the beam, $\Delta\beta_\perp/\beta_\perp$, at a reasonably small value in order to ensure that the gyrotron operates at high efficiency. An upper limit on the velocity spread is imposed by the condition that all electrons must have sufficient energy to pass through the high magnetic field region of the cavity. This implies

$$\frac{\Delta\beta_\perp}{\beta_\perp} < \left(\frac{\beta_\parallel}{\beta_\perp}\right)^2 \tag{C.28}$$

This condition is generally less restrictive than that required for high efficiency. An experimental investigation by Taranenko et al. [35] showed that a substantial reduction of efficiency occurred for $\beta_\perp/\beta_\parallel \simeq 3.25$ for a velocity spread $\Delta\beta_\perp/\beta_\perp = 4\%$, well within the limit

given by Eq. (C.28). In order to determine the maximum velocity spread based on efficiency, a numerical analysis of the beam-RF field interaction would have to be conducted. Such a study is beyond the scope of this model. Instead, the velocity spread has been limited to a fraction $\left(\frac{1}{3} \text{ to } \frac{1}{2}\right)$ of the value suggested by Eq. (C.28). Thus, for $\beta_\perp/\beta_\parallel = 1.8$, the velocity spread cannot exceed 10 - 15%.

The velocity spread of the electron beam arises from several causes, including space charge effects at the cathode, thermal effects, and surface roughness of the emitter. These components are labelled ε_{sc}, ε_T, and ε_a respectively, where $\varepsilon \equiv \Delta\beta_\perp/\beta_\perp$. The spreads resulting from these effects were calculated by Gol'denberg and Petelin [83] and Tsimring [84]. Based on their results, the limit on I can be written as:

$$I < 104 \frac{R_e \alpha}{\gamma \omega}^{3/2} \left[\varepsilon_{max}^2 - 6.3 \times 10^{-5} \left(\frac{\omega}{\sqrt{\alpha}\beta_\perp}\right)\right]^{1/2} \qquad \text{(C.29)}$$

where R_e is in millimeters, ω is in GHz, and ε_{max} is the maximum velocity spread that can be tolerated. It should be noted that this equation is applicable to both narrow and wide emitters, even though ε_{sc} differs for these two cases. This is because the wide emitter case also includes the restriction placed on beam width, which was discussed in conjunction with Eq. (C.27). When this requirement is included, both the narrow and wide emitter cases give virtually the same limit on the current for $\phi_k \simeq 7.5$ and $\beta_\perp$ within the range 0.25 - 0.45.

The second limit on current results from the need to keep the current density at the emitter low in order to ensure that the cathode have a long lifetime. If 4 A/cm^2 is chosen as the maximum density,

this leads to the condition:

$$I \leq .2513\, \ell_k \sqrt{\alpha}\, R_e \quad \text{Amps} \tag{C.30}$$

where ℓ_k and R_e are in millimeters.

Finally, a limit can be placed on the current based on the self-potential of the beam. The potential drop in the beam, as well as the voltage between the beam and cavity wall, must be kept small in order to minimize the velocity spread of the beam and achieve high efficiency. Because of the tenuous nature of the beam, its self-potential drop is negligible and the beam can be treated as monoenergetic. However, the voltage drop between the beam and the wall can be quite large. If this voltage is limited to 1.0% of the beam energy, then the following expression can be derived:

$$I \leq \frac{0.13\beta_{\|}\, U}{\ell n(R_o/R_e)} \quad A \tag{C.31}$$

where U is in kV's. The selected beam current must satisfy the limits imposed by Eqs. (C.29), (C.30), and (C.31).

References

1. R.M. Gilgenbach, M.E. Read, K.E. Hackett, F. Lucey, B. Hui, V.L. Granatstein, K.R. Chu, A.C. England, C.M. Loring, O.C. Eldridge, H.C. Howe, A.G. Kulchar, E. Lazarus, M. Murakami and J.B. Wilsen, Phys. Rev. Lett. 44 (1980) 647-650.

2. R.A. Dandle, F.W. Baity, Jr., K.H. Carpenter, J.A. Cobble, H.O. Eason, J.C. Glowienka, G.R. Haste, M.E. Hesse, S. Hirde, N.H. Lazar, B.H. Quon, T. Uckan, T.L. White, C.L. Hedrick, D.B. Batcher, L. Deleano, R.C. Goldfinger, E.F. Jaeger, L.W. Owen, D.A. Spone, J.S. Tolliver, J.B. McBridge, N.A. Krall, A.L. Sulton, Jr., Plasma Physics and Controlled Nuclear Fusion Research 1978, Innsbruck (Int. Atomic Energy Agency, Vienna,) Vol. II (1979) 365-372

3. A.M.M. Todd, M.S. Change, J.M. Greene, R.C. Grimm, J.L. Johnson, J. Manicham, Phys. Rev. Lett 38 (1977) 826.

4. L. Friedland, M. Porkolab, and I. Bernstein, Bull. Am. Phys. Soc. 24 (1979) 1059.

5. D.V. Kisel', G.S. Kovablev, V.G. Navel'yev, M.I. Petelin and Sh. Ye. Tsimring, Radio Eng. Electron. Phys. 19, No. 4,(1974) 95-100.

6. R.A. Dandl, A.C. England et. at., Nucl. Fusion 4, (1964) 344.

7. V.V. Alikaev, V.M. Glagolev and S.A. Morozov, Plasma Phys. 10, (1968) 753.

8. V.V. Alikaev, G.A. Bobrovskii, M.M. Ofitserov, V.I. Poznyak and K.A. Razumova, J.E.T.P. Lett. 15, (1972) 27.

9. V.E. Golant, M.G. Kaganskii, L.P. Pakliomov, K.A. Podushnikova and K.G. Shakhovets, Sov. Phys.-Tech. Phys. 17, (1972) 488.

10. V.V. Alikaev, Yu. I. Arsenyev, G.A. Bobrovskii, V.I. Poznyak, K.A. Razumova and Yu.A. Sokolov, Sov. Phys. Tech. Phys. 20, (1975) 327.

11. V.V. Alikaev, G.A. Bobrovskii, V.I. Poznyak, K.A. Razumova, V.V. Sannikov, Yu.A. Sokolov and A.A. Shmarin, Sov. J. Plasma Phys. 2, (1976) 212.

12. V.V. Alikaev, IAEA Conf. on Plasma Phys. and Contr. Nuclear Fusion, Innsbruck (1978).

13. J.F. Shively, P. Ferguson, H.R. Jory, J. Moran, and R.S. Symons, Conf. Digest, IEEE-S Intnl. Microwaves Symp. (1980) 99.

14. V. Granatstein, Bull. Am. Phys. Soc., Vol. 24, No. 8, October 1979.

15. T.H. Stix, The Theory of Plasma Waves, McGraw-Hill, N.Y. (1962) 27-43.

16. E. Ott, B. Hui, and K.R. Chu, Naval Research Laboratory Memorandum Report 4028 (1979). To be published in Phys. Fluids.

17. V.E. Golant, A.D. Philiya, Sov. Phys. Uspekhi 14 (1972) 413.

18. S.M. Wolfe, D.R. Cohn, R.J. Temkin and K. Kreischer, Nuclear Fusion 19, (1979) 389.

19. D.L. Jassby, D.R. Cohn, R.R. Parker, Nucl. Fusion 16 (1976) 1045.

20. D.R. Cohn, J.H. Schultz, L. Bromberg, F. Chang, D.L. Cook, M. Culbert, J. Fisher, D. Hackworth, R.D. Hay, D.L. Jassby, D.L. Kaplan, K.E. Kreischer, L.M. Lidsky, F. Malick, T. McManamy, K. Molvig, J. Murphy, M. Okabayashi, D.O. Overskei, M. Sniderman, W. Stephany, H.H. Towner, J.E.C. Williams, High Field Compact Tokamak Reactor (HFCTR) Conceptual Design, Final Report, M.I.T. Plasma Fusion Center Research Report RR-79-2, January 1979.

21. V.A. Flyagin, A.V. Gaponov, M.I. Petelin and V.K. Yulpatov, IEEE Trans. Microwave Theory and Tech. MTT-25 (1977) 514.

22. J.L. Hirshfield and V.L. Granatstein, IEEE Trans. Microwave Theory and Tech. MTT-25 (1977) 522.

23. A.A. Andronov, V.A. Flyagin, A.V. Gaponov, A.L. Gol'denberg, M.I. Petelin, V.G. Usov and V.K. Yulpatov, Infrared Physics 18 (1978) 385. Also A.V. Gaponov, V.A. Flyagin, A.Sh. Fix, A.L. Gol'denberg, V.I. Khizhnyak, A.G. Luchinin, G.S. Nusinovich, M.I. Petelin, Sh. Ye. Tsimring, V.G. Usov, S.N. Vlasov, V.K. Yulpatov, Int. Journal of Infrared and Millimeter Waves 1, No. 3 (1980) 351-372.

24. J.L. Hirshfield, I.B. Bernstein and J.M. Wachtel, IEEE Journal Quantum Electronics 1, No. 6 (1965) 237.

25. V.A. Zhurakhovskii and S.V. Koshevaya, Radio Eng. and Communication Systems, 10, No. 11 (1967) 71

26. I.I. Antakov, V.S. Ergakov, E.V. Zasypkin and E.V. Sokolov, Radiophysics and Quantum Electron. 20, No. 4 (1977) 413.

27. R.S. Symons and H.R. Jory in Proceedings of the Seventh Symposium on Engineering Problems of Fusion Research (Knoxville, Tenn. 1977).

28. K.R. Chu, Phys. of Fluids 21 (1978) 2354.

29. R.J. Temkin, K. Kreischer, S.M. Wolfe, D.R. Cohn and B. Lax, Journal of Magnetism and Magnetic Materials 11 (1979) 368.

30. J.C. Slater, Microwave Electronics. D. Van Nostrand Co., New Jersey, 1950.

31. S.N. Vlasov, G.M. Zhislin, I.M. Orlova, M.I. Petelin and G.G. Rogacheva, Radiophysics and Quantum Electron. 12, No. 8 (1969) 972.

32. A.V. Gaponov, A.L. Gol'denberg, D.P. Grigor'ev, T.B. Pankratova, M.I. Petelin and V.A. Flyagin, Radiophysics and Quantum Electron. 18, No. 2 (1975) 204.

33. N.A. Krall and A.W. Trivelpiece, Principles of Plasma Physics, McGraw-Hill, Inc. 1973.

34. M.I. Petelin and V.K. Yulpatov, Radiophysics and Quantum Electron. 18 (1975) 212.

35. V.P. Taranenko, V.N. Glushenko, S.V. Koshevaya, K. Ya. Lizhdvoy, V.A. Prus and V.A. Trapezon, Elektronaya Tekhnika, Ser. 1, Elektron. SVCh, No. 12 (1974) 47.

36. M. Abramowitz and I.A. Stegun, Handbook of Mathematical Functions. Dover, New York, 1965.

37. H. Uhm, R.C. Davidson and K.R. Chu, Phys. Fluids 21, No. 10 (1978) 1877.

38. A. Yariv, Quantum Electronics. Wiley, New York, 1975.

39. G.S. Nusinovich and R.E. Erm, Elektronaya Tekhnika, Ser. 1, Elektron, SVCh, No. 8 (1972) 55.

40. J.D. Jackson, Classical Electrodynamics. Wiley, New York, 1962.

41. L.A. Vainshtein, Open Resonators and Open Waveguides, Translated from Russian by P. Beckmann, Boulder, CO., Golem Press, 1969.

42. K.R. Chu, M.E. Read, and A.K. Ganguly, IEEE Trans. on Microwave Theory and Techniques, MTT-29 (1980) p.4.

43. Yu.V. Bykov and A.L. Gol'denberg, Radiophysics and Quantum Electronics 18, (1975) 791-792.

44. M.E. Read, R.M. Gilgenback, R. Lucey, K.R. Chu, A.T. Drobot, and V.L. Granststein, inpress, IEEE Trans on Microwave Theory and Tech (1980).

45. P.M. Morse and H. Feshback Methods of Theoretical Physics, McGraw-Hill, N.Y. (1953) 636-7.

46. R.J. Temkin and K.E. Kreischer, MIT Plasma Fusion Center Report PFC/RR-80-10 (1980)

47. G.S. Nusinovich, Elektronnaya Teknika, Ser 1, Elektronika SVCh, No. 3 (1974) 44.

48. I.G. Zarnitsyna, G.S. Nusinovich, Radiophysics and Quantum Electronics 17. No. 12 (1974) 1418.

49. G.S. Nusinovich, Radiophysics and Quantum Electronics 19, No. 12 (1976) 1301

50. E.J. Nefedov and I.M. Rossiiskii, Sov. Phys. Dokl. 23, No. 8 (1978) pp. 594-5.

51. I.G. Zarnitsyna and G.S. Nusinovich, Rad. Eng. and Electron. Phys. 23, No. 6 (1978) pp.74-8.

52. P.W. Smith, Proc. IEEE 60, No. 4 (1972) pp.422-440

53. V.S. Averbakh, S.N. Vlasov, and V.I. Talanov, Radiophysics and Quantum Elecronics 10, No. 9-10 (1967) pp. 747-760.

54. A.G. Fox, U.S. Patent 3-504-299

55. P.W. Smith, IEEE J. Quantum Electron. QE-1 (1965) pp.343-8.

56. A.F. Kurin, Rad. Eng. and Electron, Phys. 14, No. 10 (1969) pp. 1652-4.

57. A.F. Kurin, G.A. Kurina, and V.V. Novikov, Radiophys. and Quant. Electron 19, No. 7 (1976) pp. 742-747.

58. F.A. Korolev and A.F. Kurin, Rad. Eng. and Electron Phys 15, No. 10 (1970) pp 1868-1873.

59. P. Sprangle, J.L. Vomvoridis, and W.M. Manheimer, NRL Report 4366 (1981)

60. E.S. Weibel, Phys. Rev. Lett. 2, No. 3 (1959) pp.83-4.

61. J. Kotik and M.C. Newstein, J. Applied Phys. 32, No. 2 (1961) pp.178-86

62. R.J. Temkin and S.M. Wolfe, M.I.T. Plasma Fusion Center Research Report No. RR-78-9, (unpublished), (1978).

63. G.S. Nusinovich and R.E. Erm, Elektronnaya Tekhnika, Ser. 1, Elektronika SVCh, No. 8, (1972) 55.

64. J.L. Seftor, K.R. Chu, A.T. Drobot, IEEE Trans. on Microwave Theory and Techniques, MTT-27 (1979) p.9.

65. R.J. Temkin, K.E. Kreischer, V. Schultz, and D.R. Cohn, MIT Plasma Fusion Center Report PFC/RR-79-20 (1979).

66. Polytechnic Institute of Brooklyn, Proceedings of the Symposium on Millimeter Waves, New York, N.Y., (1959)

67. Leo Young, editor, Advances in Microwaves, Vol. 3, Academic Press, New York, (1968).

68. Leo Young, editor, Advances in Microwaves, Vol. 4, Academic Press, New York, (1969).

69. E.C. Okress, editor, Microwave Power Engineering, Academic Press, New York, (1968).

70. F.A. Benson, editor, Millimeter & Submillimeter Waves, Iliffe Books Ltd., London, (1969)

71. A.E. Karbowiak, Trunk Waveguide Communication, Chapman and Hall Ltd., (1965).

72. Institute of Electrical Engineers, International Conference on Millimetric Waveguide Systems, London, England, (1976).

73. D.A. Alsberg, J.C. Bankert, and P.T. Hutchison, Bell System Technical Journal 56, No. 10, (1977) 1829.

74. S.N. Vlasov and I.M. Orlova, Radiophysics and Quantum Electronics 17, No. 1, 115 (1974).

75. S.N. Vlasov, L.I. Zagrijadskaya and M.I. Petelin, Radio Eng. and Electron. Phys. 20, (1975) 14.

76. Tischer, F.J., IEEE-MTT-27, No. 1 (1979) p.31.

77. Anderson, J.C., Carlin, J.W., Thomson, D.J., and West, T.J., Bell System Technical Journal, 67, No. 10 (1977) p. 2157.

78. Rowe, H.E., and Warters, H.D., Bell System Technical Journal, 41, No. 5 (1962) p. 1031.

79. Carlin, J.W., and Moorthy, S.C., Bell System Technical Journal, 56, No. 10. (1977) p. 1849

80. Wengenroth, R.D., IEEE Trans. Microwave Theory and Tech. MTT-26 (1978) p. 332.

81. Sporleder, F., IEE, International Conference on Millimetric Waveguide Systems (London, England, 1976) p. 68.

82. Dandl, R.A., Report of the Ad Hoc Panel on RF Heating in Tokamaks, ERDA-76-115 (1976), Appendix D-3.

83. A.L..Goldberg and M.I. Petelin, Radiophysics and Quantum Electronics 16, No. 1, (1973) 106-111.

84. Sh. E. Tsimring, Radiophysics and Quantum Electronics 15, 952-961, (1972).

85. R.C. Davidson, C.D. Striffler, J. Plasma Phys. 12, (1974) 353.

86. R.C. Davidson, H.S. Uhm, Phys. Fluids 22 (1979).

EXTERNAL DISTRIBUTION

Institutions

Argonne National Laboratory
Association Euratom-CEA
    Grenoble, France
    Fontenay-aux-Roses, France
Atomics International
Austin Research Associates
Bank of Tokyo
Brookhaven National Laboratory
CNEN-Italy
College of Wiliam and Mary
Columbia University
Cornell University
    Laboratory for Plasma Studies
    Applied & Engineering Physics
Culham Laboratory
Culham Laboratory/Project JET
E G & G Idaho, Inc.
Electric Power Research Institute
Gneral Atomic Company
General Electric Company
Georgia Institute of Technology
Grumman Aerospace Corporation
Hanform Engineering Development Lab.
Hiroshima University
Japan Atomic Energy Research Institute
Kernforshungsanlage/Julich GmbH
Kyoto University
Kyushu University
Lawrence Berkeley Laboratory
Lawrence Livermore Laboratory
Los Alamos Scientific Laboratory
Max Planck Institut für Plasma Physik
McDonnel Douglas Astronautics Co.
Nagoya University
Naval Research Laboratory
New York University/Courant Institute
Nuclear Service Corporation
Oak Ridge National Laboratory
Osaka University
Physics International Group
Princeton University/Plasma Physics
Sandia Research Laboratories
Science Applications, Inc.
    Fusion Energy Development
    Lab for Applied Plasma Studies
    Plasma Research Institute
Stanford University
University of California/Berkeley
    Dept. of Electrical Engineering
    Dept. of Physics
University of California/Irvine
University of California/Los Angeles
    Dept. of Electrical Engineering
    Dept. of Physics
    Tokamak Fusion Laboratory
    School of Eng. & Applied Science
University of Maryland
    Dept. of Electrical Engineering
    Dept. of Physics
    Inst. for Physical Science & Tech.
University of Michigan
University of Rochester
University of Texas
    Dept. of Mechanical Engineering
    Dept. of Physics
University of Tokyo
University of Washington
University of Wisconsin
    Dept. of Nuclear Engineering
    Dept. of Physics
Varian Associates
Westinghouse Electric Corporation
Yale University

EXTERNAL DISTRIBUTION

Individuals

Amheard, N.
Electric Power Research Institute
Balescu, R.C.
University Libre de Bruxelles
Bartosek, V.
Nuclear Res. Inst., Czechoslovakia
Berge, G.
University of Bergen, Norway
Braams, C.M.
FOM/Inst. for Plasma Phys., Netherlands
Brunelli, B.
C.N.E.N.-Centro Frascati, Italy
Brzosko, J.S.
Inst. of Physics, Warsaw University
Cap, F.
Inst. fur Theor. Physik, Innsbruck
Conn, R.W.
Chemical Engineering, UCLA
Consoli, T.
Residence Elysee I, Claud, France
Cuperman, S.
Dept. of Physics, Tel-Aviv University
Engelhardt, W.
Max-Planck Institute für Plasmaphysik
Engelmann, F.
FOM/Inst. for Plasma Phys., Netherlands
Fiedorowicz, H.
Kaliski Inst. of Plasma Physics, Warsaw
Frolov, V.
Div. of Research & Laboratories, Vienna
Fushimi, K.
Science Council of Japan, Tokyo
Gibson, A.
JET/Culham, Abingdon, England
Goedbloed, J.P.
FOM/Inst. for Plasma Phys., Netherlands
Goldenbaum, G.
Lawrence Livermore Laboratories
Hamberger, S.M.
Australian National University
Hellberg, M.A.
University of Natal, South Africa
Hintz, E.A.K.
Kernforschungsanlage/Julich GmbH
Hirose, A.
University of Saskatchewan
Hirsch, R.
EXXON Research & Engineering Co.
Hosking, R.J.
University of Waikato, New Zealand
Ito, H.
Osaka University
Jacquinot, J.G.
CEN/Fontenay-aux-Roses, France
Jensen, V.O.
Riso National Lab, Denmark
Jones, R.
National University of Singapore
Kadomtsev, B.B.
Kurchatov Institute, Moscow
Kostka, P.
Central Res. Inst., Budapest
Kunze, H.-J.
Ruhr-Universitat, F. R. Germany
Lackner, K.
Max-Planck Inst. für Plasmaphysik
Lee, S.
University of Malay
Lenhert, B.P.
Royal Inst. of Technology, Sweden
Malo, J.O.
University of Nairobi, Kenya
Mercier, C.H.B.
C.N.E.N./Fontenay-aux-Roses, France
Nodwell, R.A.
University of British Columbia, Canada
Offenberger, A.A.
University of Alberta, Canada
Ortolani, S.
Centro di Studio/C.N.R., Italy
Palumbo, D.
Rue de la Loi, 200, Bruxelles
Pellat, R.
Centre National, Palaiseau, France
Paquette, G.
Universite de Montreal, Canada
Rabinovich, M.S.
Lebedev Institute, Moscow
Razumova, K.A.
Kurchatov Institute, Moscow
Rogister, A.
Kernforschungsanlage/Julich GmbH
Rosenau, P.
Technion, Haifa, Israel
Rosenblum, M.
Soreq Research Center, Yavne, Israel
Rudakov, L.I.
Kurchatov Institute, Moscow
Ryutov, D.D.
Nuclear Physics Instit., Novosibirsk
Salas, J.S.R.
Inst. Nacional de Investig. Nucleares
Shafranov, V.D.
Kurchatov Institute, Moscow
Smirnov, V.P.
Kurchatov Institute, Moscow
Spalding, J.-J.
Culham Laboratory, Abingdon, England
Tachon, J.
CEN/Fontenay-aux-Roses, France
Tewari, D.D.
Dept. of Physics, IIT, New Dehli
Trocheris, M.
CEN/Fontenay-aux-Roses, France
Vandenplas, P.E.
Ecole Royale Militaire, Bruxelles
Verheest, F.
Rijksuniversiteit, Gent, Belgium
Watson-Munro, C.N.
University of Sydney, Australia
Wesson, J.A.
Culham Laboratory, Abindgon, England
Wilhelm, R.
Inst. für Plasmaphysik, Stuttgart
Wilhelmsson, K.H.B.
Chalmers Univ. of Technology, Sweden
Wobig, H.
Max-Planck Inst. für Plasmaphysik